7. Theoretical Models for $\gamma\gamma \to \pi^+\pi^-$

In principle, the process $\gamma\gamma \to \pi^+\pi^-$ should be described by QED coupling of the photons to quarks, with the interactions of the quarks and gluons within the mesons calculated from quantum chromodynamics (QCD). In practice, however, such calculations may only be carried out in the perturbative regime of QCD. If the pion-pair invariant mass is large enough and the pions are produced at large angles with respect to the incoming photons, then the amplitude factors into two parts.[40] The first consists of a parton distribution amplitude $\phi(x_i, Q)$ for each pion—the probability amplitude for finding valence quarks in the pion, each carrying a fraction x_i of the pion's momentum, integrated over transverse momenta up to $k_{\perp i} \approx Q$, where Q is the momentum transferred in the process. The second is a hard-scattering amplitude T for scattering the clusters of collinear valence partons from each pion. Thus the amplitude is

$$\mathcal{M}_{\lambda\lambda'}(s,\theta) = \int_0^1 dx\, dy\, \phi^*(x, \widetilde{Q}_x)\phi^*(y, \widetilde{Q}_y)\, T_{\lambda\lambda'}(x, y; s, \theta)\,, \tag{7.1}$$

where $\widetilde{Q}_x \approx \min(x, 1-x)\sqrt{s}|\sin\theta|$ and $\lambda\lambda'$ are the photon helicities.

Brodsky and Lepage[1] have carried out this calculation with leading-order QCD. The parton distribution functions are determined by relating them to the known pion form factor $F_\pi(s)$, and the hard scattering amplitudes are calculated from the diagrams shown in Fig. 7.1. There remains some unknown x dependence of $\phi(x, Q)$ for which assumptions must be made. However, the result is almost completely independent of those assumptions and takes the form

$$\frac{d\sigma}{dt} = \frac{4\,|F_\pi(s)|^2}{1-\cos^4\theta} \cdot \frac{d\sigma}{dt}(\gamma\gamma \to \mu^+\mu^-)\,, \tag{7.2}$$

where $F_\pi(s) \approx 0.4\,\mathrm{GeV}^2/s$, and s and t are the usual Mandelstam invariants.†

† For the reaction $a + b \to c + d$, one defines the Mandelstam invariants as $s = (p_a + p_b)^2$, $t = (p_c - p_a)^2$, and $u = (p_d - p_a)^2$. The three are related by the simple expression $s + t + u = m_a^2 + m_b^2 + m_c^2 + m_d^2$.

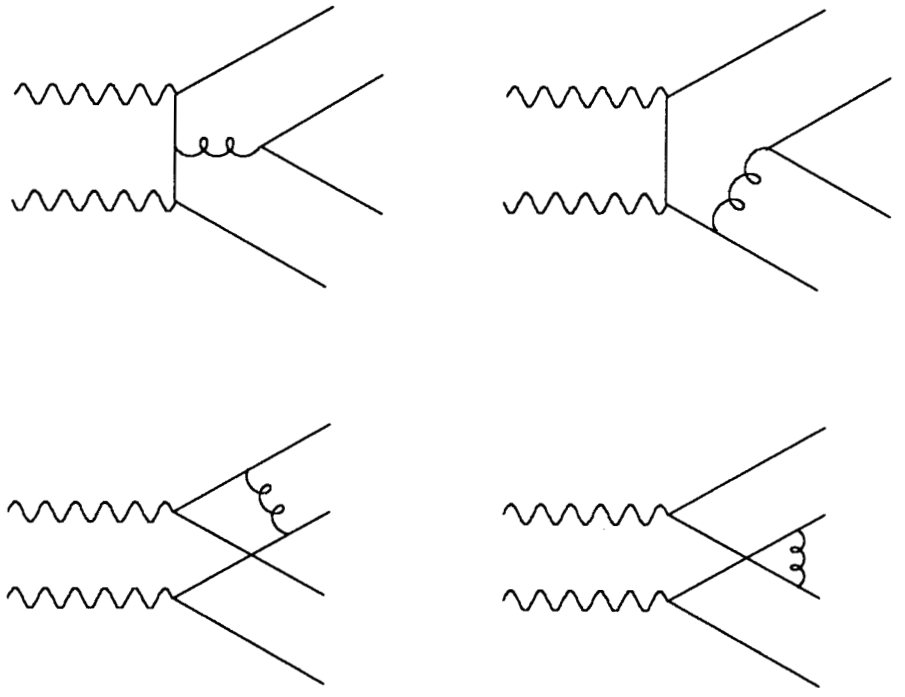

Figure 7.1. Leading-order QCD diagrams contributing to the process $\gamma\gamma \rightarrow \pi^+\pi^-$. The amplitudes are calculated with the quarks collinear with the incoming and outgoing pions

Equation 7.2 is a beautiful and simple parameter-free prediction, but it is valid only when s-channel resonance effects can be neglected. We have seen that the energy range accessible to DELCO is in fact dominated by resonance effects. Furthermore, that energy range probably is too low to give momentum transfers large enough to place the process in a regime where QCD perturbation theory becomes valid. Unfortunately, it is not possible to extend the DELCO measurement to higher energies, because there is no way to separate pions from muons. As seen in Eqn. 7.2, the pion-pair cross section at high energies falls like $1/s^2$ relative to the muon-pair cross section. Therefore, the background quickly dominates the signal to such an extent that there is no possibility of subtracting it.

It is clear that a more phenomenological model must be used to study the low energy pion-pair spectrum. The physical picture of single-hadron exchange

and formation has been useful in some low-energy phenomenology and may be expected to work well for this case. One expects a large contribution from single-pion exchange in the t-channel, $\gamma\pi^{\pm} \rightarrow \gamma\pi^{\pm}$, which may be used to describe the low-energy continuum production, and the s-channel resonance effects can be modeled according to a relativistic Breit-Wigner shape. Such a model has been used by a number of experiments,[41] and it has been found to give a good description of the data when interference between the single-pion exchange and the resonance production is included. We will see that such a model also gives a good description of the DELCO data. But first it is important to consider the motivations for the model, its theoretical problems and limitations, and also some possible extensions.

7.1 Description of the Incoming Two-Photon State

It is necessary first to describe the initial two-photon state in such a way that the conservation laws for angular momentum and parity are easily incorporated into the matrix elements. The formulas used for partial wave expansions can be found in the textbook of J. Werle,[42] and the phase and normalization conventions used here are the same as his. Let $R(\alpha, \beta, \gamma)$ represent the operator to produce a rotation through the three Euler angles about, respectively, the z axis, the y axis, and the new z axis, and let $L_z(v)$ represent a Lorentz boost in the $\hat{z}$ direction to a relative velocity v, with no rotation of the coordinate axes. Then the basis states for a single particle are written as

$$|ms; \vec{p}\lambda\rangle = |ms; \phi\theta p\lambda\rangle = R(\phi, \theta, 0) L_z(v) |ms; 000\lambda\rangle \,. \tag{7.3}$$

This notation represents a particle of mass m, spin s, and helicity λ, moving as a plane wave with momentum p in the direction given by the polar angles ϕ and θ (from here on, the notation ms will be suppressed). The state $|000\lambda\rangle$ is just the

particle at rest, with its spin component in the $\hat{z}$ direction given by $s_z = \lambda$. The important phase convention assumed is[43]

$$|0\pi p\lambda\rangle = |00\,-p\lambda\rangle = e^{-i\pi s} R(\pi,\pi,0) L_z(v)|000\lambda\rangle\,, \tag{7.4}$$

and the normalization is $\langle\vec{p}\,'\lambda'|\vec{p}\lambda\rangle = E\delta^3(\vec{p}\,' - \vec{p})\delta_{\lambda'\lambda}$, where $E = \sqrt{m^2 + \vec{p}^{\,2}}$.

A state with two particles may be formed as a direct product of the two single-particle states. In the center-of-mass system, for particle 1 going in the direction (ϕ, θ), the appropriate definition is

$$|\vec{P} = 0; \phi\theta p\lambda_1\lambda_2\rangle = \sqrt{\frac{p}{W}} \cdot R(\phi,\theta,0)|00p\lambda_1\rangle|00\,-p\lambda_2\rangle\,, \tag{7.5}$$

where $W^2 \equiv P^\mu P_\mu$ and $P = p_1 + p_2$. The normalization follows from that of Eqn. 7.3 and is found to be

$$\langle\vec{P}\,'; \Omega'\lambda_1'\lambda_2' \,|\, \vec{P}; \Omega\lambda_1\lambda_2\rangle = \delta_{\lambda_1'\lambda_1}\delta_{\lambda_2'\lambda_2}\delta^4(P' - P)\,\delta^2(\Omega' - \Omega)\,, \tag{7.6}$$

where we have made use of the identity

$$\frac{\mathrm{d}^3p_1}{E_1}\frac{\mathrm{d}^3p_2}{E_2} = \frac{p}{W}\,\mathrm{d}^4P\,\mathrm{d}\phi\,\mathrm{d}\cos\theta = \frac{p}{W}\,\mathrm{d}^4P\,\mathrm{d}^2\Omega\,, \tag{7.7}$$

One should note that the basis vectors of Eqn. 7.3 are not defined properly for the case of real photons, which have mass zero and, hence, no rest system. They may still be defined the same way, however, if one assumes as a starting point the vector $|00p_0[\lambda]\rangle$ rather than $|000\lambda\rangle$ and keeps in mind that in this case λ is a property of the particle, with a value of $+s$ or $-s$, and does not change from one Lorentz frame to another. Then the two-photon state may be defined exactly as in Eqn. 7.5. Note, however, that whereas Eqn. 7.5 may usually be expanded in another basis represented by l, the relative angular momentum, and σ, the total spin, that cannot be done for the case of two massless particles.

Another technical point is that the two photons, being identical bosons, must be in a state which is symmetric under interchange of the two. Interchanging the two particles in Eqn. 7.5 is equivalent to interchanging the helicities and then rotating about the y axis by π radians. Therefore the four possible incoming states for the two photons are, in their center-of-mass system traveling in the z direction with momenta $\pm q$,

$$\begin{aligned}
\psi^1_{J_z=0} &= \sqrt{\tfrac{1}{2}}\,[1 + R(0,\pi,0)]|\vec{P} = 0; 00q++\rangle \\
\psi^2_{J_z=0} &= \sqrt{\tfrac{1}{2}}\,[1 + R(0,\pi,0)]|\vec{P} = 0; 00q--\rangle \\
\psi^3_{J_z=2} &= \sqrt{\tfrac{1}{2}}\left[|\vec{P} = 0; 00q+-\rangle + R(0,\pi,0)|\vec{P} = 0; 00q-+\rangle\right] \\
\psi^4_{J_z=-2} &= \sqrt{\tfrac{1}{2}}\left[|\vec{P} = 0; 00q-+\rangle + R(0,\pi,0)|\vec{P} = 0; 00q+-\rangle\right] .
\end{aligned} \tag{7.8}$$

Our goal is to project out components of the incoming $\gamma\gamma$ states which have definite spin and parity. A state of definite angular momentum may be formed from the basis defined in Eqn. 7.5 according to[44]

$$|\vec{P} = 0; M[WJ]\lambda_1\lambda_2\rangle = \sqrt{\tfrac{2J+1}{4\pi}} \int d\Omega\, \overline{D}^J_{M\lambda}(\phi,\theta,0)|\vec{P} = 0; \phi\theta W\lambda_1\lambda_2\rangle\,, \tag{7.9}$$

where $\lambda \equiv \lambda_1 - \lambda_2$ and

$$D^j_{m'm}(\alpha,\beta,\gamma) = e^{im'\alpha} d^j_{m'm}(\beta) e^{im\gamma} \equiv \langle jm' \,|\, R(\alpha,\beta,\gamma) \,|\, jm\rangle\,. \tag{7.10}$$

If $\mathbf{P}$ is the operator for space inversion and $A_{1,2}$ is the exchange operator, then[45]

$$\begin{aligned}
\mathbf{P}|\vec{P} = 0; M[WJ]\lambda_1\lambda_2\rangle &= \eta_1\eta_2(-1)^{J-s_1-s_2}|\vec{P} = 0; M[WJ]\,-\lambda_1\,-\lambda_2\rangle \\
A_{1,2}|\vec{P} = 0; M[WJ]\lambda_1\lambda_2\rangle &= (-1)^{J-2s}|\vec{P} = 0; M[WJ]\lambda_2\lambda_1\rangle\,,
\end{aligned} \tag{7.11}$$

where η_1 and η_2 are the intrinsic parities and the second equation, of course, applies only to identical particles. If the two are identical *and* $\lambda_1 = -\lambda_2$, then both operators have the same effect, which means that for a state to be an eigenstate

of both operators, the parity eigenvalue must be positive for bosons and negative for fermions. Hence we immediately get two of the desired components of the $\gamma\gamma$ state:

$$\psi^{J+}_{M=\pm 2} = \sqrt{\tfrac{1}{2}}\left[|\vec{P}=0; M=\pm 2\,[WJ]+-\rangle + (-1)^J|\vec{P}=0; M=\pm 2\,[WJ]-+\rangle\right], \tag{7.12}$$

for which $J \geq 2$. The other two possibilities are easily seen to be

$$\psi^{J\pm}_{M=0} = \sqrt{\tfrac{1}{2}}\left[\tfrac{1+(-1)^J}{2}\right]\left[|\vec{P}=0; M=0\,[WJ]++\rangle \pm |\vec{P}=0; M=0\,[WJ]--\rangle\right]. \tag{7.13}$$

Note that equations 7.12 and 7.13 immediately yield Yang's theorem,[46] which says that a state of two real photons with definite parity cannot have $J = 1$. Also, for $J = 0$ and for all odd parity states, $M = J_z = 0$ is the only possibility.

Using Eqn. 7.9, the four incoming states can be expanded in terms of the partial waves of equations 7.12 and 7.13:

$$\begin{aligned}\psi^{1,2}_{J_z=0} &= \sum_J \sqrt{\tfrac{2J+1}{4\pi}} D^J_{00}(0,0,0)\left[\psi^{J+}_{M=0} \pm \psi^{J-}_{M=0}\right]\\ \psi^{3,4}_{J_z=\pm 2} &= \sum_J \sqrt{\tfrac{2J+1}{4\pi}} D^J_{\pm 2\pm 2}(0,0,0)\psi^{J+}_{M=\pm 2}\,,\end{aligned} \tag{7.14}$$

where the D functions with the given arguments all actually are unity. Overall the result is simple and obvious, except for the important limitation on J for the helicity-zero states.

7.2 The Scattering Cross Section

Consider the process $a + b \to c + d$ in the center-of-mass system. The initial and final states may be described as in Eqn. 7.5, and with the normalization given in Eqn. 7.6, the density of final states within the phase space $\mathrm{d}^3p_c\,\mathrm{d}^3p_d$ is

$$W(p_c p_d) = \frac{1}{E_c E_d}\frac{W}{p}\,. \tag{7.15}$$

Let S_{fi} be the matrix of scattering amplitudes, and define the transition matrix by $S_{fi} = \delta_{fi} + i\delta^4(P_f - P_i)T_{fi}$. Then the probability per unit time and volume for the transition is

$$\begin{aligned} P &= \frac{1}{VT}\sum_{f\neq i} S^\dagger_{if} S_{fi} \\ &= \frac{1}{(2\pi)^4}\sum_{\lambda_c\lambda_d}\int \mathrm{d}^3p_c\,\mathrm{d}^3p_d\,W(p_cp_d)\,|\langle cd;\vec{p}_c\vec{p}_d\lambda_c\lambda_d|T|ab;\vec{p}_a\vec{p}_b\lambda_a\lambda_b\rangle|^2\,\delta^4(P_f - P_i) \\ &= \frac{1}{(2\pi)^4}\sum_{\lambda_c\lambda_d}\int |\langle cd;\vec{P}=0;\phi\theta p\lambda_c\lambda_d|T|ab;\vec{P}=0;00p\lambda_a\lambda_b\rangle|^2\mathrm{d}\Omega\,. \end{aligned} \tag{7.16}$$

The integration over the total momentum has been facilitated by the use of Eqn. 7.7. For the initial state, the relative flux density is the number of states per unit volume $\mathrm{d}^3p_a\,\mathrm{d}^3p_b$ times the relative velocity $v_a + v_b$:

$$\mathcal{F} = \frac{1}{(2\pi)^6}E_aE_b\frac{p}{W}(v_a + v_b) = \frac{p^2}{(2\pi)^6}\,. \tag{7.17}$$

Hence the differential cross section is given by

$$\frac{\mathrm{d}\sigma}{\mathrm{d}\Omega} = \sum_{\lambda_c\lambda_d}|f_{\lambda_c\lambda_d}|^2 = \frac{(2\pi)^2}{p^2}\sum_{\lambda_c\lambda_d}|\langle cd;\phi\theta p\lambda_c\lambda_d|T|ab;00p\lambda_a\lambda_b\rangle|^2\,. \tag{7.18}$$

Now consider the process $\gamma\gamma \to \pi\pi$, where the initial state is as described in the previous section. The final state may be described by Eqn. 7.5, with $\lambda_1 = \lambda_2 = 0$, and expanded into states of definite isospin I:

$$\begin{aligned} |\pi\pi;0\,0\rangle &= \sqrt{\tfrac{2}{3}}\,|\pi^+\pi^-\rangle - \sqrt{\tfrac{1}{3}}\,|\pi^0\pi^0\rangle \\ |\pi\pi;2\,0\rangle &= \sqrt{\tfrac{1}{3}}\,|\pi^+\pi^-\rangle + \sqrt{\tfrac{2}{3}}\,|\pi^0\pi^0\rangle\,, \end{aligned} \tag{7.19}$$

where the notation on the left is $|\pi\pi;I\,I_3\rangle$ and the charged pion state is

$$|\pi^+\pi^-\rangle \equiv \sqrt{\tfrac{1}{2}}\,|\pi;1\,{+1}\rangle|\pi;1\,{-1}\rangle + \sqrt{\tfrac{1}{2}}\,|\pi;1\,{-1}\rangle|\pi;1\,{+1}\rangle\,. \tag{7.20}$$

Define $f^I_\lambda(s,t)$, where $\lambda = |\lambda_a + \lambda_b|$, to be the amplitudes for $\gamma\gamma \to \pi\pi$, with the normalization as specified in Eqn. 7.18. Assuming no polarization of the incoming photon beams, the cross section for $\gamma\gamma \to \pi^+\pi^-$ is expressed as an average over the two possible relative polarizations:

$$\frac{d\sigma}{d\Omega}(\gamma\gamma \to \pi^+\pi^-) = \tfrac{1}{2}|f^c_0(s,t)|^2 + \tfrac{1}{2}|f^c_2(s,t)|^2\,, \tag{7.21}$$

where $f^c_\lambda \equiv \sqrt{\tfrac{2}{3}} f^0_\lambda + \sqrt{\tfrac{1}{3}} f^2_\lambda$.

Using Eqn. 7.9, these amplitudes are easily expanded into partial waves of definite angular momentum:

$$\begin{aligned} f^I_0(s,t) &= \sum_{J=0}^{\infty}(2J+1)d^J_{0\,0}(\theta) f^I_{J0}(s) \\ f^I_2(s,t) &= e^{-2i\phi}\sum_{J=2}^{\infty}(2J+1)d^J_{2\,0}(\theta) f^I_{J2}(s)\,, \end{aligned} \tag{7.22}$$

where $f^I_{J\lambda}(s) \equiv \frac{2}{\sqrt{s}} T^I_{J\lambda}(s)$ and $T^I_{J\lambda}(s) \equiv \frac{1}{2}\langle \pi\pi; s\,J\,I|T|\gamma\gamma; \lambda[s\,J]\lambda_a\lambda_b\rangle$. In both of these sums, only even J contribute. That is because, from equations 7.12 and 7.13, the $\gamma\gamma$ states of odd J all have even parity, but the parity of a $\pi\pi$ partial wave is, from Eqn. 7.11, $(-1)^J$. Also, the relative phase $e^{-2i\phi}$ of the two helicity amplitudes is of no consequence for unpolarized beams and is dropped henceforth.

7.3 Description of $\pi\pi$ Elastic Scattering

Let us apply the same formalism as in the previous section to the process $\pi\pi \to \pi\pi$. With $g^I(s,t)$ defined to be the isospin amplitudes, the partial wave expansion is

$$g^I(s,t) = \frac{1}{p}\sum_{J=0}^{\infty}(2J+1)\mathcal{A}^I_J(s)P_J(\cos\theta)\,, \tag{7.23}$$

where $P_J(x)$ are the Legendre polynomials. The partial wave amplitudes $\mathcal{A}_J^I$ may be written in terms of phase shifts as

$$\mathcal{A}_J^I(s) = -\tfrac{1}{2}i\left[\eta_J^I(s)\cdot e^{2i\delta_J^I(s)} - 1\right]. \tag{7.24}$$

For elastic scattering the $\eta_J^I(s)$ are unity.

Now let us briefly consider some of the general knowledge of $\pi\pi$ partial waves. For $s < 1\,\mathrm{GeV}^2$ and $J \geq 2$, a very good approximation is $\delta_J^I(s) \approx 0$. For $J = 0$ the situation is somewhat confused. The phase shift $\delta_0^0(s)$ appears to pass through resonance in the region $\sqrt{s} = 0.5 \to 0.7\,\mathrm{GeV}$, but there is lack of good direct evidence for the so-called σ resonance at that energy. In any case, the $\delta_0^I(s)$ are substantial from the $\pi\pi$ threshold on up.[47,48] We will not be concerned with the $\delta_1^I(s)$, which are dominated by the ρ resonance, but $\delta_2^0(s)$ above $s = 1\,\mathrm{GeV}^2$ is of particular interest, due to the relatively narrow f resonance at $\sqrt{s} = 1.274\,\mathrm{GeV}$. These strong-interaction effects have important implications for the process $\gamma\gamma \to \pi^+\pi^-$, as may be understood in detail by studying the general unitary and analytic properties of the matrix elements.

7.4 Unitarity, Analyticity and the Model for $\gamma\gamma \to \pi^+\pi^-$

The scattering matrix $S(s,t,u)$ is believed to be an analytic function of the Mandelstam variables s, t, and u. Also, it is required by conservation of probability to be unitary: $S^\dagger S = \mathbf{1}$. In terms of the transition matrix, $T = -i(S-1)$, the unitarity requirement is

$$i(T^\dagger - T) = T^\dagger T. \tag{7.25}$$

These properties can be used to provide a number of useful constraints on any model of hadronic interactions. A brief review of how that is done is provided here, but for a much more complete discussion, one may refer to Ref. 49.

Consider T, for the process $a + b \to c + d$, as a function of s at a fixed value of $t = t'$. All of the singularities in T of the first Riemann sheet are believed to lie on

the real s axis, which is compatible with the unitarity requirement. Considering Eqn. 7.25, the right hand side requires a sum over all kinematically accessible channels, so it changes drastically with s as additional channels open. Therefore, there must be a singularity in T at each point $s > (m_a + m_b)^2$ where a reaction threshold is. Perturbation theory shows that the singularities take the form of cuts with branch points at the thresholds and extending to $s = \infty$, so possible values of s can extend over many Riemann sheets. The sheet containing the real axis below the first branch point is called the physical sheet, and the physical amplitude is defined for real $s = s'$ in the s-channel physical region ($s > (m_a + m_b)^2$ and $t < 0$) by

$$T_{ab\to cd}(s', t) = \lim_{\epsilon\to 0} T_{ab\to cd}(s' + i\epsilon, t)\,. \tag{7.26}$$

Furthermore, if there is a particle with the quantum numbers of $a + b$ but with a mass $m_0 < m_a + m_b$, then there is a pole on the real axis at $s = s_0 = m_0^2$. The contribution to T of such a pole is called the *Born term*.

But that is not all. The same analysis may be applied to the crossed reaction $a + \bar{d} \to c + \bar{b}$, called the u-channel. Since with t fixed at $t = t'$, s and u are directly related by the expression $s = \sum m_i^2 - t' - u$, then all of the poles and cuts in the u-channel must appear on the unphysical portion of the real s axis, with the cuts extending to $s = -\infty$. Thus the complex s plane looks something like what is shown in Fig. 7.2.

7.4.1 *The Born Term and Fixed-t Dispersion Relations*

Let us consider how these generalities apply to $\gamma\gamma \to \pi^+\pi^-$. There can be no pole in the s-channel, but certainly there is one in each of the t and u channels, $\gamma\pi^\pm \to \gamma\pi^\pm$, from single-pion exchange. The residue of the pole is calculated from the first term in a perturbation expansion for a field theory with point coupling of photons to charged spin-zero mesons. Figure 7.3 shows the three relevant Feynman diagrams. A vertex of two pions and one photon contributes to the S-matrix a

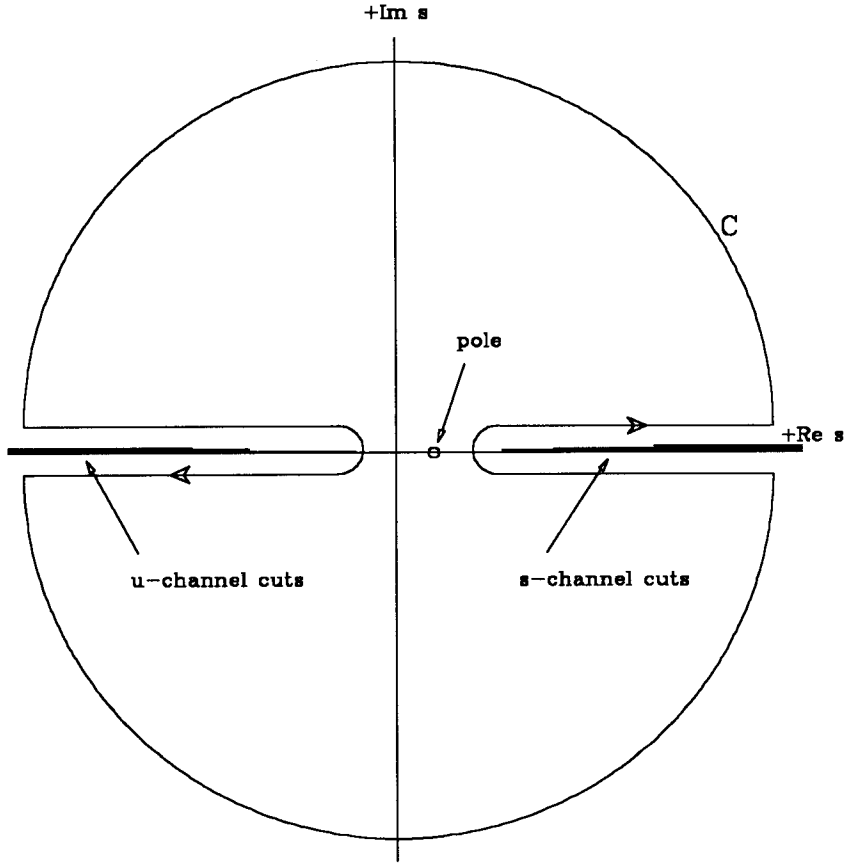

Figure 7.2. The complex s plane for the transition matrix $T(s,t)$ at constant $t = t'$. The contour C is that used to derive the fixed-t dispersion relations.

factor $-ie(p+p')_\mu$, where p and p' are the pion momenta and μ is the Lorentz component of the photon.[14] The vertex of two pions and two photons contributes $2ie^2 g_{\mu\nu}$, and the meson propagator is $i/(p^2 - m_\pi^2)$. Otherwise the calculation proceeds as in QED, and the result is[50]

$$\begin{aligned} \frac{d\sigma}{d\Omega} &= \tfrac{1}{2}|B_0|^2 + \tfrac{1}{2}|B_2|^2 \\ \text{helicity}-0: \quad B_0 &= \frac{\alpha}{W}\sqrt{\beta}\frac{1-\beta^2}{1-\beta^2\cos^2\theta} \equiv \frac{1}{2\pi}\sqrt{\beta s}F_0^B(s,t) \\ \text{helicity}-2: \quad B_2 &= \frac{\alpha}{W}\sqrt{\beta}\frac{\beta^2\sin^2\theta}{1-\beta^2\cos^2\theta} \equiv \frac{\sqrt{\beta}}{2\pi}\frac{tu - m_\pi^4}{\sqrt{s}}F_2^B(s,t)\,, \end{aligned} \tag{7.27}$$

where $\beta = \sqrt{(s-4m_\pi^2)/s}$ is the pion velocity. The reduced amplitudes F_0 and F_2 are defined such that they are free of all kinematic singularities[51] and may be

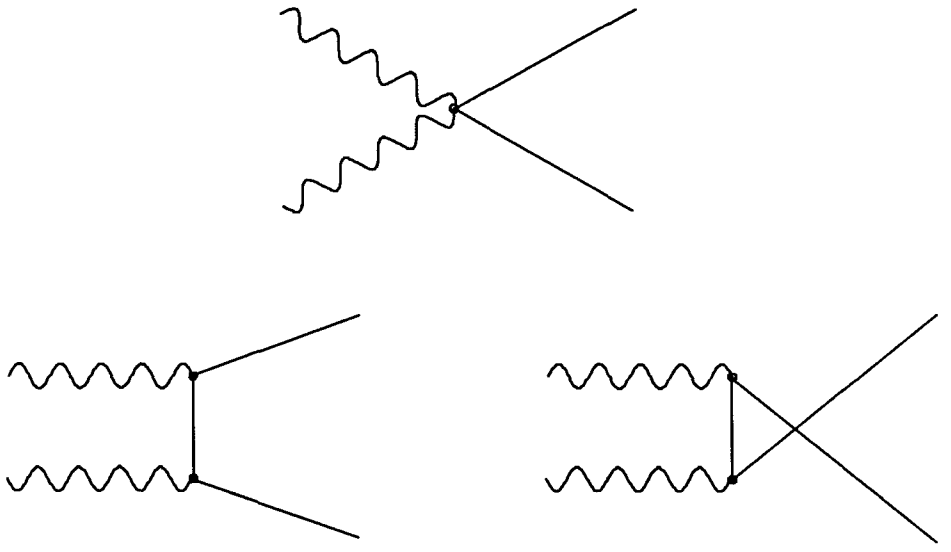

Figure 7.3. The Feynman diagrams for the Born term in the process $\gamma\gamma \to \pi^+\pi^-$.

written in terms of the Mandelstam variables as

$$\begin{aligned} F_0^B &= 2\pi\alpha \frac{m_\pi^2}{(m_\pi^2 - t)(m_\pi^2 - u)} \\ F_2^B &= 2\pi\alpha \frac{1}{(m_\pi^2 - t)(m_\pi^2 - u)} \,. \end{aligned} \tag{7.28}$$

To include formally the contributions of the cuts, fixed-t dispersion relations may be used. Figure 7.2 shows an integration contour C in the complex s plane. Consider the integral

$$\int_C \frac{F(s',t')\,ds'}{s'-s} = 2\pi i \left[F(s,t') - F^B(s,t')\right] , \tag{7.29}$$

which has been evaluated by using Cauchy's theorem and including the residue of the single pole of F within the contour. By letting the arcs of the contours go to infinity, the integral may be evaluated from only the contributions along the real axis. Using the property of *hermitian analyticity*, $T(s+i\epsilon,t) = T^*(s-i\epsilon,t)$, results in the dispersion relations

$$F_{0,2}(s,t') = F_{0,2}^B(s,t') + \frac{1}{\pi}\int_{m_\pi^2}^{\infty} \frac{\Im F_{0,2}(u',t')\,du'}{u'-u} + \frac{1}{\pi}\int_{4m_\pi^2}^{\infty} \frac{\Im F_{0,2}(s',t')\,ds'}{s'-s} , \tag{7.30}$$

where the first of the two integrals has been rewritten as an integration over $u' = 2m_\pi^2 - t' - s'$ and $\Im$ denotes the imaginary part. The two integrals, which are the contributions respectively of the left hand and right hand cuts of Fig. 7.2, are defined for real s by approaching the real axis from above. They are exceedingly complicated, so the equations cannot be solved without making some explicit assumptions about the form of $\Im F(s,t)$ in the region of integration.

7.4.2 *Resonant Partial Waves*

The approach to be taken is to consider only contributions from exchanges, in the s or u channels, of single resonances. Since a resonance has definite spin and parity, then only a single partial wave must be considered. The analytic properties of a partial wave amplitude follow directly from those of the full amplitude and the $D^J_{\lambda_1,\lambda_2}$ functions.[52] In particular, there are cuts along the positive real s axis extending from the first threshold to $s = \infty$. Since there is no fundamental difference between a resonance and a stable hadron besides the mass (assuming all other quantum numbers to be the same), then one expects the exchange of a resonance to result in a pole in the complex s plane near the real axis, but above the first branch point. The pole can neither be on the real axis nor on the physical sheet, so hermitian analyticity demands that there be in fact two poles, placed symmetrically on opposite sides of the real axis and on an unphysical sheet. Only the one which is below the real axis is close to the physical sheet, since the unphysical sheet is reached from the physical sheet by crossing the real axis from above. Assuming that this pole, located at $s_r = m_r - im_r\Gamma$, dominates the behavior of $T_J(s)$ for s near s_r, so only the first term of a series expansion of $T_J(s)$ about $s = s_r$ need be kept, gives the relativistic Breit-Wigner shape for the resonance:

$$T_J(s) = \frac{m_r\Gamma}{m_r^2 - s - im_r\Gamma}\,. \tag{7.31}$$

Such a formula may be improved by including contributions from other singularities. In particular, consider the branch point at the two-particle threshold

$s_t = (m_a + m_b)^2$.† If the branch point is not too close, then the amplitude can be approximated by the first terms in an *effective range* expansion about s_t.[52] This results in an energy dependence for the width Γ. In particular, Γ contains a *threshold factor* p^{2J+1}. In Ref. 53, Lyth suggests the parameterization, for $f \to \pi\pi$,

$$\begin{aligned} \Gamma(s) &= \Gamma_0 \left(\frac{p}{p_0}\right)^5 \left(\frac{s_0}{s}\right)^{\frac{1}{2}} \left(\frac{s_0 + a}{s + a}\right)^2 ; \\ p &\equiv \tfrac{1}{2}\sqrt{s - 4m_\pi^2}\,, \quad p_0 \equiv \tfrac{1}{2}\sqrt{s_0 - 4m_\pi^2}\,, \end{aligned} \tag{7.32}$$

where $s_0 = m_f^2$ and $a \sim m_f^2$. This is the form assumed in the remainder of this analysis. For the f resonance,[6]

$$m_r = m_f = 1.274 \pm 0.005\,\text{GeV}, \qquad \Gamma_0 = \Gamma_f = 0.178 \pm 0.020\,\text{GeV}, \tag{7.33}$$

and we use $a = 0.5\,\text{GeV}^2$. The resulting $\pi\pi$ phase shift for the $I = 0$, $J = 2$ amplitude is given by $\tan\delta_2^0(s) = m_f\Gamma(s)/(m_f^2 - s)$, and this gives a favorable comparison with measurements from pion-nucleon scattering, as shown in Fig. 7.4.[54]

Another modification of Eqn. 7.31 is necessary to include inelastic effects. Note that it is only the *position* of the pole which is characteristic of the resonance itself, and that is all which remains constant for the resonance when observed in several different reactions. What needs modified is the residue. That depends on the coupling of the resonance to the initial and final states. It can be factored into a product of two *partial* widths, of which one depends on only the initial state and the other on only the final state. For example, for $\gamma\gamma \to f \to \pi^+\pi^-$, the

† In general there could be several such thresholds. For example, the f resonance is affected by the $\pi\pi$, 4π, and KK thresholds. We neglect the latter two, because the branching ratios of the f to those channels are relatively small.

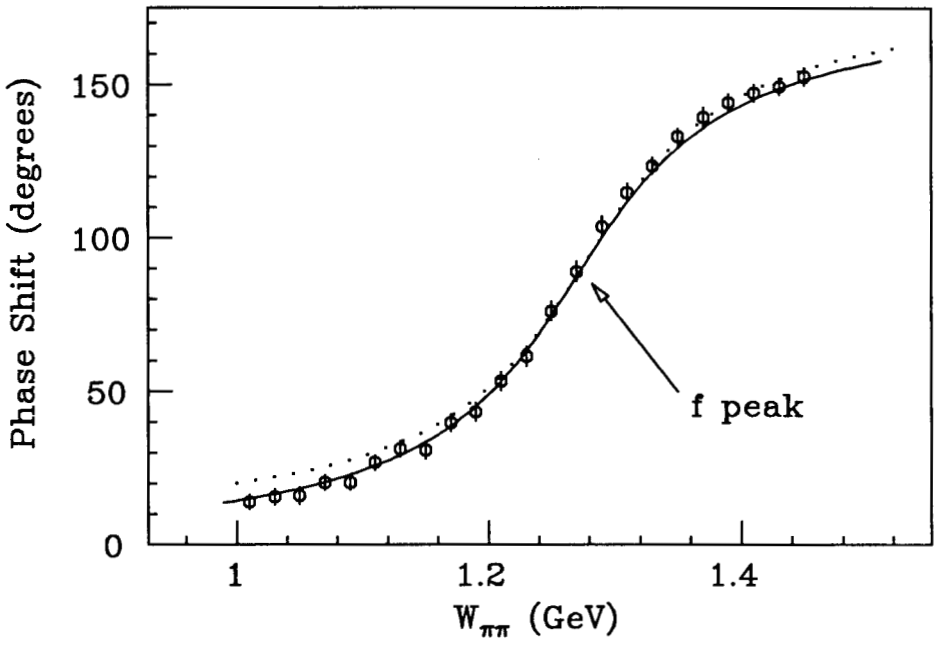

Figure 7.4. The $I = 0$, $J = 2$ $\pi\pi$ phase shift as measured from pion-nucleon scattering. The solid curve is the best fit, by varying the parameter a, of Eqn. 7.32, for which $a = 0.5\,\mathrm{GeV}^2$. The dotted curve shows the Breit-Wigner shape with no energy dependence for the width.

appropriate expression for the amplitude is

$$T^c_{2\lambda}(s) = \sqrt{\tfrac{2}{3}}\,T^0_{2\lambda}(s) = \frac{m_f\left[\frac{2}{3}\Gamma^\lambda_{\gamma\gamma}(s)\Gamma_{\pi\pi}(s)\right]^{\frac{1}{2}}}{m_f^2 - s - im_f\Gamma(s)}\,,$$
$$\text{where}\quad \Gamma_{\gamma\gamma} = \mathrm{BR}(f\to\gamma\gamma)\cdot\Gamma$$
$$\text{and}\quad \Gamma_{\pi\pi} = \mathrm{BR}(f\to\pi\pi)\cdot\Gamma\,. \tag{7.34}$$

The factor of $\sqrt{\frac{2}{3}}$ is from Eqn. 7.19, and λ denotes the fact that there are separate amplitudes for each of the two possible $\gamma\gamma$ helicities. The s dependence of $\Gamma_{\pi\pi}(s)$ should be the same as that of $\Gamma(s)$, since $\pi\pi$ is by far the dominant decay mode. For the s dependence of $\Gamma_{\gamma\gamma}(s)$ we assume the same form as in Eqn. 7.32, except that m_π is replaced by $m_\gamma = 0$.

A little reflection on the meaning of the constants m_f and Γ_f is in order. Ideally they should give the position of the resonance pole as $s_r = m_f^2 - im_f\Gamma_f =$

$1.62 - 0.227i$, since that is the quantity, given in Ref. 6, which characterizes the resonance. However, when the form in Eqn. 7.32 is used for the width, then the pole moves to the position $s_r = 1.59 - 0.225i$, which is a change of the order of one percent. Changing m_f from 1.274 GeV to 1.284 GeV is enough to return the pole to the position given in Ref. 6, but one must keep in mind that all experiments from which those measurements were taken had to do a similar sort of extrapolation to determine the pole position. Hence there is a lot of potential for 1% errors caused by the parameterization of the resonance shape.†

7.4.3 *Estimate of Contributions from the Left Hand Cut*

Now let us use the parameterizations for resonance exchange to estimate possible contributions from the left hand cut in Eqn. 7.30. To do so, we consider the reaction $\gamma\pi \to \gamma\pi$ (these calculations are by Lyth in Ref. 51). Using the inverse of Eqn. 7.9 with $\lambda_\gamma = \pm 1$ and $\lambda_\pi = 0$ gives the description of the $\gamma\pi$ state, which leads to the partial wave expansions for the amplitudes, aside from overall phases of $e^{\pm\phi}$, of

$$T_\pm(s,t) = 2\sum_{J=0}^{\infty}\left(\tfrac{2J+1}{4\pi}\right) d^J_{1\,\pm 1}(\theta) T_{J\,\pm}(s)\,, \tag{7.35}$$

where the $+$ or $-$ refers to the relative helicity of the photons.

Consider the contribution of vector resonances to the $J = 1$ partial wave. From Eqn. 7.11, one can see that a $J = 1$ partial wave with negative parity is formed by the combination $T_{1\,+}(s) - T_{1\,-}(s)$, so the resonance must couple equally to the two helicities if parity is to be conserved. Hence

$$T_{1\,+}(s) = T_{1\,-}(s) = \frac{\frac{1}{2} m_r \Gamma_{\gamma\pi}}{m_r^2 - s - i m_r \Gamma_r}\,. \tag{7.36}$$

† Note that the change in m_f is significant, since it is greater than the error quoted for m_f in Ref. 6. However, even that error estimate is said to be no more than an educated guess.

When the pion mass and the finite resonance width are neglected, then the imaginary parts of the $J = 1$ resonant contributions to Eqn. 7.35 are

$$\begin{aligned} \Im T_-(s,t) &= -\frac{3}{4\pi}\frac{\Gamma_{\gamma\pi}}{m_r}\, t\, \delta(m_r^2 - s) \\ \Im T_+(s,t) &= -\frac{3}{4\pi}\frac{\Gamma_{\gamma\pi}}{m_r}\, u\, \delta(m_r^2 - s)\,. \end{aligned} \tag{7.37}$$

These relations are rewritten in terms of the reduced amplitudes (see Eqn. 7.27), after which crossing symmetry is used to give the corresponding amplitudes for the reaction $\gamma\gamma \to \pi\pi$. T_- becomes the helicity-zero amplitude and T_+ the helicity-two amplitude:

$$\begin{aligned} \Im F_0 &\approx 6\pi^2 \frac{\Gamma_{\gamma\pi}}{m_r}\, \delta(u - m_r^2) \\ \Im F_2 &\approx 6\pi^2 \frac{\Gamma_{\gamma\pi}}{m_r}\frac{1}{m_r^2}\, \delta(u - m_r^2)\,. \end{aligned} \tag{7.38}$$

Inserting these into the first integral of Eqn. 7.30 yields the estimates for the resonance contributions to the left hand cuts:

$$\begin{aligned} F_0^r &= 6\pi \frac{\Gamma_{\gamma\pi}}{m_r}\frac{1}{m_r^2 - u} \\ F_2^r &= 6\pi \frac{\Gamma_{\gamma\pi}}{m_r}\frac{1}{m_r^2}\frac{1}{m_r^2 - u}\,. \end{aligned} \tag{7.39}$$

In Ref. 51, these expressions are used to estimate the u-channel resonance contribution relative to the Born term. The result is that the resonance terms are completely negligible near the $\pi\pi$ threshold but may be significant in the region near one GeV for large-angle scattering. But that estimate is very conservative, using $\Gamma_{\gamma\pi}/m_r \approx 0.1\alpha$, which is about eight times greater than the experimental value now found in Ref. 6 for the ρ. For the helicity-zero amplitude, the contribution from ρ exchange may be as much as half the Born contribution in the f region at large angles. But that is not important since even the helicity-zero Born term is negligible in that region, compared with the helicity-two Born term. Figure 7.5 shows the effect of ρ exchange in the helicity-two amplitude. At

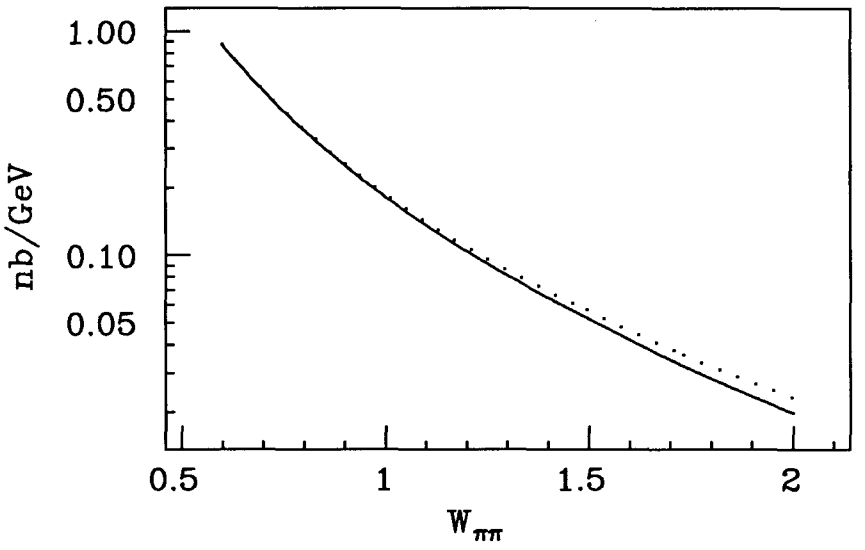

Figure 7.5. The effect of ρ exchange on the $\pi^+\pi^-$ continuum in $e^+e^- \to e^+e^-\pi^+\pi^-$. The solid curve shows the contribution from single pion exchange, while the dotted curve includes the ρ-exchange contribution. The photon flux is calculated from EPA, and the final pion-pair state is integrated over the acceptance defined by $-0.6 \leq \cos\theta \leq 0.6$ and $k_\perp/W \leq 0.2$.

$W = 0.6\,\mathrm{GeV}$ there is an increase of only 0.5% over the Born term; at $W = m_f$ the increase is 5.3%; at $W = 2.0\,\mathrm{GeV}$ the increase is 17%. Thus the ρ-exchange contribution is almost completely negligible compared with pion exchange.

The ω, which has a relatively large $\gamma\pi$ width, does not contribute to the charged channel, and one expects the heavier vector mesons, such as the A_1, to contribute considerably less than the ρ, since their masses place them further from the physical region. Also, higher partial waves give even more negligible contributions, so all indications point to complete dominance of the Born term in the t and u channels.

7.4.4 Corrections Required by Unitarity

It is a useful exercise to write explicitly Eqn. 7.25, the unitarity relation, for the process $\gamma\gamma \to \pi\pi$. To simplify the discussion, it is best actually to work with the pure isospin states of Eqn. 7.19. Let $A^I(\phi\theta;\phi'\theta';s)$ be the amplitude for elastic

$\pi\pi$ scattering in the center-of-mass system from the initial angles (ϕ', θ') to the final angles (ϕ, θ). $T^I_\lambda(\phi\theta; s)$ is the amplitude for photons incoming along the z axis and pions outgoing in the directions given in the center-of-mass system by the angles (ϕ, θ). Amplitudes for purely QED processes like $\gamma\gamma \to \gamma\gamma$ are small compared with hadronic amplitudes, so any term including them may safely be neglected. Then the unitarity relation is (with the isospin index I suppressed)

$$\begin{aligned} i\left[T^\dagger_\lambda(\phi\theta; s) - T_\lambda(\phi\theta; s)\right] = \int \mathrm{d}^3p'_1\, \mathrm{d}^3p'_2\, W(p'_1 p'_2) \\ \times A^\dagger(\phi\theta; \phi'\theta'; s) T_\lambda(\phi'\theta'; s)\delta^4(p'_1 + p'_2) \\ + \text{ inelastic contributions,} \end{aligned} \tag{7.40}$$

where p'_i refers to one pion of the pair corresponding to the angles (ϕ', θ'). The only significant inelastic contributions to Eqn. 7.40 are those coming from strong interaction processes, such as $\gamma\gamma \to K^+K^-$, and of those, only the ones energetically accessible are included, depending on the value of s.

Now we may use Eqn. 7.7 to transform to the center-of-mass variables (p', ϕ', θ') and integrate out the $\delta^4(p'_1 + p'_2)$. Also, let us substitute in the partial wave expansions of Eqn. 7.22 for $T^I_\lambda(\phi\theta; s)$, using the definitions $f^I_\lambda \equiv \frac{2\pi}{p} T^I_\lambda$ (Eqn. 7.18) and $f^I_{J\lambda} \equiv \frac{1}{p} T^I_{J\lambda}$ (Eqn. 7.22). For $A^I(\phi\theta; \phi'\theta'; s)$ we substitute the expansion of Eqn. 7.23, suitably rotated:

$$A^I(\phi\theta; \phi'\theta'; s) = 2\sum_{J=0}^{\infty}\sum_{M=-J}^{J}\left(\frac{2J+1}{4\pi}\right) d^J_{M0}(\theta) d^J_{M0}(\theta') e^{iM(\phi-\phi')} \mathcal{A}^I_J(s)\,. \tag{7.41}$$

After these substitutions, the angular integrations become trivial, and we are left with a separate requirement for each partial wave:

$$\Im T^I_{J\lambda}(s) = \left[\mathcal{A}^I_J(s)\right]^* T^I_{J\lambda}(s) + \text{ inelastic contributions.} \tag{7.42}$$

If the inelastic contributions are negligible or zero, as they must be for small enough s, then Eqn. 7.42 may be solved. Using Eqn. 7.24, one finds

$$T^I_{J\lambda}(s) = |T^I_{J\lambda}(s)|e^{i\delta^I_J(s)} . \tag{7.43}$$

This is equivalent to Watson's theorem for photoproduction,[55] and essentially says that the phase of the $\gamma\gamma \to \pi\pi$ amplitude is given by the $\pi\pi$ phase shift if the energy is low enough that no significant inelastic channels are open. One can consider this phase to be due to final-state interactions of the pions after they are produced from the photons.

7.4.5 Justification of the Born Approximation

From the discussion of Section 7.3, below the f region the only significant phase shifts are δ^I_0. There are no inelastic contributions in that region, so Eqn. 7.43 must be considered to be exact. In Ref. 51, the rough measurements available for δ^I_0, along with the fixed-t dispersion relations of Eqn. 7.30, are used to calculate the necessary corrections to $T^I_{00}(s)$, and one finds that, although large corrections ($\approx$ 30% enhancement) are necessary near threshold, from non-resonant effects, they become negligible above $\sqrt{s} = 0.4\,\text{GeV}$.[56] When nearing the f region, the phase shifts of the δ^0_2 partial wave begin to become significant. We will see that, to a good approximation, Eqn. 7.43 must be satisfied even throughout the f region, up to about 1.4 GeV, leading to corrections to a simple model of the Born term combined with a resonant amplitude.

Such corrections, though, are well defined by Eqn. 7.43. Furthermore, we have shown that contributions from vector meson exchanges are negligible with respect to the pion exchange, so the Born term, with unitarity corrections, is all that is needed to describe the continuum production itself. The remaining question concerns to what extent the Born term actually is described by the diagrams of Fig. 7.3. We have assumed that the pions are point particles. That

seems physically reasonable for low enough photon energy, since the actual size of the pion will be small compared with the photon wavelength. A fairly rigorous justification for the applicability of the point-coupling calculation near threshold may be arrived at through the hypothesis of a partially conserved axial current (PCAC) and current algebra,[57] which are theoretical ideas that have met with much success in describing phenomena of low energy pion physics. The result is that the point-like coupling is valid up to the addition of terms with a relative magnitude of approximately s/m_ρ^2. In fact, we will see that a good description of the data is achieved for the entire region below the f, which agrees with the typical theoretical prejudice that such approximations can be expected to be good up to energies of about 1 GeV.

The Born cross section falls like $1/s$, whereas from Eqn. 7.2 we expect at high energies that the cross section must fall as $1/s^3$, due to the $1/s$ behavior of the form factor. However, since the Born term agrees well with the data below the f, it is reasonable to use it as an extrapolation through the full range of the f, up to about 1.4 GeV. It only is necessary to make an estimate of what errors this extrapolation might cause for the measurement of the resonant part of the cross section.

7.4.6 Constraints on the Coupling of $\gamma\gamma$ to the f Resonance

We have determined that for the region well below the f resonance and above $\sqrt{s} = 0.4\,\text{GeV}$, the cross section should be adequately represented by the Born term alone, unless there happens to be some large direct coupling of $\gamma\gamma$ to low-mass scalar resonances. For the region near the f, the resonant contribution to the $J = 2$, $I = 0$ partial wave must be included.

In general there are two amplitudes to consider for the f, with one for each possible helicity. However, in Chapter 1 we have seen that there is considerable evidence that the helicity-two amplitude is strongly dominant. For now, let

us assume zero coupling for helicity-zero, so the cross section is written, for $\gamma\gamma \to \pi^+\pi^-$, as

$$\frac{\mathrm{d}\sigma}{\mathrm{d}\Omega} = \tfrac{1}{2}\left|B_0(s,t)\right|^2 + \tfrac{1}{2}\left|B_2(s,t) + 5\sqrt{\tfrac{2}{3}}\, d^2_{2\,0}(\theta) R^0_{2\,2}(s)\right|^2 , \tag{7.44}$$

where the B_λ are as defined in Eqn. 7.27, and the $I = 0$ resonance contribution is defined as in Eqn. 7.34:

$$R^0_{2\,2}(s) = \frac{2}{\sqrt{s}} T^0_{2\,2}(s) = \frac{2}{\sqrt{s}} \frac{g}{m_f^2 - s - i m_f \Gamma(s)}; \quad g \equiv m_f \left[\Gamma_{\gamma\gamma}\Gamma_{\pi\pi}\right]^{\frac{1}{2}} . \tag{7.45}$$

Suppose that the inelastic channels still are small in the f region. Then the $J = 2$ partial wave should satisfy the unitarity constraint of Eqn. 7.43. It is interesting to see what that implies for the phase of g in Eqn. 7.45.† The $J = 2$ component of $B_2(s,t)$ is

$$\begin{aligned} \frac{2}{\sqrt{s}} \mathcal{B}_{2\,2}(s) &= \frac{1}{2}\int_{-1}^{1} B_2(s,t) d^2_{2\,0}(\theta)\, \mathrm{d}\cos\theta , \\ \mathcal{B}_{2\,2}(s) &= \frac{\alpha}{4}\sqrt{\frac{3\beta}{2}}\left[\frac{(1-\beta^2)^2}{2\beta^3}\ln\left(\frac{1+\beta}{1-\beta}\right) - \frac{1}{\beta^2} + \frac{5}{3}\right] . \end{aligned} \tag{7.46}$$

Consider the sum of the $I = 0$, $J = 2$ amplitudes, $\sqrt{2/3}\mathcal{B}_{2\,2}(s) + T^0_{2\,2}(s)$, for $s = m_f^2$. Equation 7.43 requires that the sum have a phase of $e^{i\pi/2}$ at that energy, so setting the real part of the sum to zero constrains the imaginary part of g:

$$\begin{aligned} \Im g &= \sqrt{\tfrac{2}{3}}\, m_f \Gamma \mathcal{B}_{2\,2}(m_f^2) \\ &= 0.00025\,\mathrm{GeV}^2. \end{aligned} \tag{7.47}$$

As for the real part of g, the experimental data definitely require $\Re g > 0$, since the f peak is shifted downwards in $\sqrt{s}$ relative to its position when observed without interference with the Born term.

† This analysis closely follows that of Ref. 56.

Equation 7.47 essentially means that the sum of the $I = 0$, $J = 0$ amplitudes may be written as

$$A^0_{2\,2}(s) = \sqrt{\tfrac{2}{3}}\,\mathcal{B}_{2\,2}(s) + T^0_{2\,2}(s) = \frac{g'}{m_f^2 - s - im_f\Gamma(s)}\,, \tag{7.48}$$

with $g' \equiv \Re g + \sqrt{2/3}(m_f^2 - s)\mathcal{B}_{2\,2}(s)$. This has the form of a resonance pole with an energy dependent coupling g' and explicitly satisfies Eqn. 7.43. The difference here from a more typical resonance amplitude is that g' has a relatively rapid variation across the resonance, due to the $1/\sqrt{s}$ energy dependence of the Born amplitude. This phenomenon causes difficulties when measuring the $\gamma\gamma$ width of the f from charged pion pairs. The problem results both because of the large resonance width Γ and because of the large $J = 2$ contribution from the Born term. If either of those quantities were small, then from Eqn. 7.47 it is clear that g would be essentially real and there would be no issue about whether the energy dependence is properly described.

The process $\gamma\gamma \to f \to \pi^0\pi^0$ has no Born term from pion exchange, so one expects that the Crystal-Ball measurement does not suffer from any serious theoretical ambiguities. Therefore, assuming that their measurement of the $\pi^0\pi^0$ spectrum yields a value for the *magnitude* of g, as defined above, then Eqn. 7.47 may be used to predict the phase of g. The Crystal-Ball result,[9] $\Gamma_{\gamma\gamma} = 2.7 \pm 0.2 \pm 0.6\,\mathrm{keV}$ (assuming only helicity-two coupling) yields $|g| = 0.00080\,\mathrm{GeV}^2$, and hence we predict a phase for the coupling of $\gamma\gamma$ to the f of $\phi = \sin^{-1}(\Im g/|g|) \approx 0.32\,\mathrm{radians}$.

7.4.7 *Further Consideration of the Unitarity Condition*

The prediction for the phase of the $\gamma\gamma \to \pi\pi$ amplitude relies upon the assumption, implicit in Eqn. 7.43, that the contributions from other inelastic processes in the $J = 2$, $I = 0$ partial wave are negligible. The validity of this assumption can be checked by a method due to Lukaszuk.[58] He writes the

inelastic contributions to Eqn. 7.42 as $\sum_{n\neq\pi\pi} a_n b_n^*$, where a_n is the $J = 2$, $I = 0$ partial wave for $\gamma\gamma \to n$, and b_n is the corresponding partial wave for $\pi\pi \to n$.† Only states n which are hadronic and kinematically accessible at the energy $\sqrt{s}$ are included in the sum. In this case, for $s = m_f^2$, the possibilities are $n = \{KK, 4\pi, K\pi\pi, \eta\eta, \eta\pi\pi\}$, of which only the first two have been measured in two-photon scattering.

First let us consider how the inelasticity η_J^I of Eqn. 7.24 is related to the reaction cross section. The result of squaring Eqn. 7.23 and integrating over the full solid angle is the total elastic cross section

$$\sigma^{I=0}_{\pi\pi\to\pi\pi} = \int |g^0(s,t)|^2 \mathrm{d}\Omega = \frac{4\pi}{s-s_0}\sum_J (2J+1)|\eta_J^0(s)\cdot e^{2i\delta_J^0(s)} - 1|^2\,, \qquad (7.49)$$

where $s_0 \equiv 4m_\pi^2$. The reaction or inelastic part of the cross section then is identified as

$$\sigma_r^{I=0} = \frac{4\pi}{s-s_0}\sum_J (2J+1)\left[1-(\eta_J^0)^2\right], \qquad (7.50)$$

from which it follows that the b_n have the property

$$\sum_{n\neq\pi\pi} |b_n|^2 = \tfrac{1}{4}\left[1-(\eta_2^0)^2\right]. \qquad (7.51)$$

Similarly, the total $I = 0$ cross section for $\gamma\gamma \to \pi\pi$ may be calculated:

$$\sigma_\lambda^I = \int |f_\lambda^I|^2 \mathrm{d}\Omega = \frac{16\pi}{s}\sum_J (2J+1)|T_{J\lambda}^I|^2\,. \qquad (7.52)$$

If we let $\sigma_{\gamma\gamma}^{0\,2}$ denote the total $\gamma\gamma$ cross section for $I = 0$, $J = 2$ and $\sigma_{\gamma\gamma\to\pi\pi}^{0\,2}$ the part of that cross section into two pions, then the a_n have the property

$$\sum_{n\neq\pi\pi} |a_n|^2 = \frac{s}{80\pi}(\sigma_{\gamma\gamma}^{0\,2} - \sigma_{\gamma\gamma\to\pi\pi}^{0\,2})\,. \qquad (7.53)$$

---

† Actually, Lukaszuk considers the form factor for the process $e^+e^- \to \pi\pi$, but the calculation is closely analagous to that presented here.

After substituting Eqn. 7.24 and $T^0_{2\,2}(s) \equiv |T^0_{2\,2}(s)|e^{i\psi(s)}$, then Eqn. 7.42 may be written as

$$|T^0_{2\,2}|\left(\frac{\eta^0_2 \exp[2i(\psi - \delta^0_2)] - 1}{2i}\right) = e^{i\psi} \sum_{n \neq \pi\pi} a_n b^*_n \,. \tag{7.54}$$

Lukaszuk's bound now follows from taking the absolute value squared of this equation and applying Schwartz's inequality to the right hand side:

$$|T^0_{2\,2}|\left[\tfrac{1}{4}\left(1 - \eta^0_2\right)^2 + \eta^2_0 \sin^2(\psi - \delta^2_0)\right] \leq \sum_{n \neq \pi\pi} |a_n|^2 \sum_{n \neq \pi\pi} |b_n|^2 \,. \tag{7.55}$$

Using equations 7.51 and 7.53, this may be written in the convenient form

$$\tfrac{1}{4}\left(1 - \eta^0_2\right)^2 + \eta^2_0 \sin^2(\psi - \delta^2_0) \leq \tfrac{1}{4}\left[1 - (\eta^0_2)^2\right] \cdot \left[r - 1\right], \tag{7.56}$$

where $r \equiv \sigma^{0\,2}_{\gamma\gamma}/\sigma^{0\,2}_{\gamma\gamma\to\pi\pi}$.

Now, at $s = m^2_f$, the inelasticity is known to be $\eta^0_2(m^2_f) = \Gamma_{\pi\pi}/\Gamma = 0.84$, so we have the limit $\sin^2(\psi - \delta^0_2) \leq 0.088(r - 1) - 0.0076$. In Ref. 53, Lyth uses the present-day results from $\gamma\gamma$ physics to estimate r and arrives at the result $r - 1 < 60\,\mathrm{nb}/240\,\mathrm{nb} = 0.25$, which in turn implies that the phase of the $J = 2$, $I = 0$ amplitude for $\gamma\gamma \to \pi\pi$ must be within about 0.1 radians of the value of the corresponding $\pi\pi$ phase shift. Relating this to the analysis of the previous section, we find that the imaginary part of g must be within the range

$$\Im g = 0.00025 \pm 0.00007\,\mathrm{GeV}^2, \tag{7.57}$$

and the phase of the $\gamma\gamma f$ coupling, assuming the Crystal Ball result for $\Gamma_{\gamma\gamma}$, is predicted to be in the range $\phi = 0.32 \pm 0.10$.

7.5 THE MODEL OF MENNESSIER

Mennessier has produced a complete model for meson pair production from two photons[59] which is similar to the model presented in the previous section but considerably more complicated in some respects. He begins with an effective Lagrangian, so there is the usual pion-exchange Born term, but also additional vector-meson exchanges. The vector-meson exchanges, which give contributions to the left hand cut in the complex s plane, are determined from the crossed channel reactions, so the coupling strengths of the vector mesons to $\pi\gamma$ are taken from the known radiative partial widths. That is the same approach taken in Section 7.4.3, except that there the effects of the crossed channels are estimated from the fixed-u dispersion relations, while Mennessier introduces terms such as $\varepsilon_{\mu\nu\alpha\beta} h_\rho \vec{\pi} \cdot [\partial_\mu \vec{\rho}_\nu - \partial_\nu \vec{\rho}_\mu] F_{\alpha\beta}$ into the Lagrangian density.† Although such point couplings often work well for single pion exchange at sufficiently low energy, it is well known that form factors must be introduced, when using such a formalism for the heavier mesons, in order to describe hadronic scattering data. Mennessier himself states in Ref. 59 that his model must overestimate even the ρ-exchange contribution. Therefore, the analysis of Section 7.4.3, which is due to Lyth,[51] may be more correct. There, we saw that the ρ-exchange contribution is negligible when compared with pion exchange, so when considering the Mennessier model, we always will neglect all of the vector-meson exchanges. Only pion exchange is included for the t and u channels.

Corrections required by unitarity are made for the t and u-channel contributions through an analytic, coupled channel K-matrix formalism for final state interactions, in which both pion and kaon intermediate states are included. All partial waves for the Born term are included, but only the S and D waves are unitarized. The solutions for these lowest partial waves of the K-matrix formalism are obtained by fitting to available hadronic scattering data. It is interesting to

† In this expression, h_ρ is the $\gamma\pi\rho$ coupling constant, $\vec{\pi}$ is the pion field, where the arrow refers to the three isospin components, $\vec{\rho}$ is the ρ field, and $F_{\alpha\beta}$ is the electromagnetic field strength tensor, which is composed of the photon field.

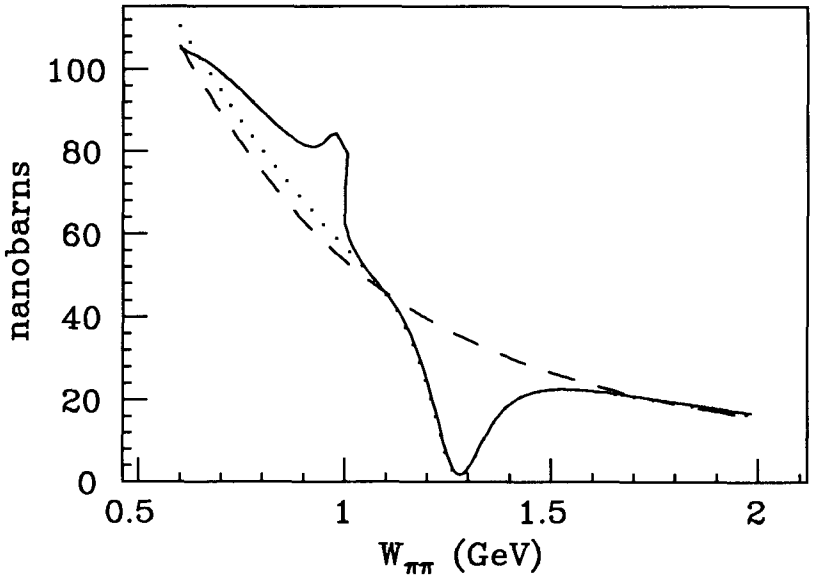

Figure 7.6. The Mennessier model at $\theta = \pi/2$ with and without unitarity corrections for final state interactions. The dashed line shows the simple Born term, which is identical to Eqn. 7.27, the dotted line includes unitarization of the D-wave, and the solid line includes unitarization of the S-wave as well. No direct resonance couplings are included.

see the effect of unitarization on the Born term. Figure 7.6 shows the invariant-mass spectrum at $\theta = \pi/2$ with no terms in the Lagrangian for coupling of $\gamma\gamma$ to s-channel resonances. We find that even with no resonance coupling, the S^* (980) scalar resonance forms a quite prominent peak. The effect of the $J = 2$, $I = 0$ phase shift in the f region actually is a dip rather than a peak. This is similar to the result obtained in Section 7.4.4. From equations 7.45 and 7.47, one can see that the additional term, involving the imaginary part of g, which was added to the $J = 2$, $I = 0$ part of the amplitude in order to satisfy unitarity, is negative at the resonance peak with respect to the Born term. In fact, it precisely cancels the $J = 2$, $I = 0$ part of the Born term at $s = m_f^2$.

Finally, there are direct s-channel resonance contributions, for both scalar and tensor mesons, which have $\gamma\gamma$ couplings to be adjusted at will. These couplings are the only parameters in the model which are not determined by strong interaction data, so they may be measured by fitting the model to data.

7.6 Comparison of the Two Models

In this section we look at the shapes of the invariant-mass and angular distributions of the models for $\gamma\gamma \to \pi^+\pi^-$ presented in the previous two sections, which we refer to as the Lyth model and the Mennessier model. When fitting these distributions to the data in Chapter 8, it is necessary to convolute them with the two-photon luminosity function and to integrate over the detector acceptance. Here we simply present the $\gamma\gamma \to \pi^+\pi^-$ predictions for the invariant mass spectrum at a fixed angle of $\theta = \pi/2$, which is the center of the DELCO acceptance.

First, consider the Born term, which is, before unitarity corrections, exactly the same in both models. As must be the case for two photons annihilating to form two particles of spin zero, the helicity-two cross section goes to zero at $\cos\theta = \pm 1$. However, as the energy increases, the angular distribution becomes more and more flat, and the points where it begins to fall to zero move closer to $\cos\theta = \pm 1$. In contrast, the helicity-zero amplitude is sharply peaked toward small angles. However, it falls rapidly with increasing energy, compared with the helicity-two amplitude, and is not very significant within the DELCO acceptance, as one can see from Fig. 7.7. Thus the Born term is, within the DELCO acceptance, rather well approximated by a $1/s$ energy dependence and a uniform angular distribution.

The $f\,(1270)$ resonance contributions are not identical for the two models. However, they do have the same angular distributions, since a single resonance is produced only in a single partial wave. Both models allow the introduction of a resonance contribution to the $J = 2$ partial wave in both the helicity-zero and helicity-two amplitudes, for which the angular distributions are plotted in Fig. 1.2. In such a case, the two-photon width of the f must be described by two independent parameters, $\Gamma^{\lambda}_{\gamma\gamma}$ $\{\lambda = 0, 2\}$, such that $\Gamma_{\gamma\gamma} = \Gamma^0_{\gamma\gamma} + \Gamma^2_{\gamma\gamma}$. The energy dependence of the resonance terms, however, differs between the two models. To see that, let us compare them for the most simple case, where unitarity corrections are neglected.

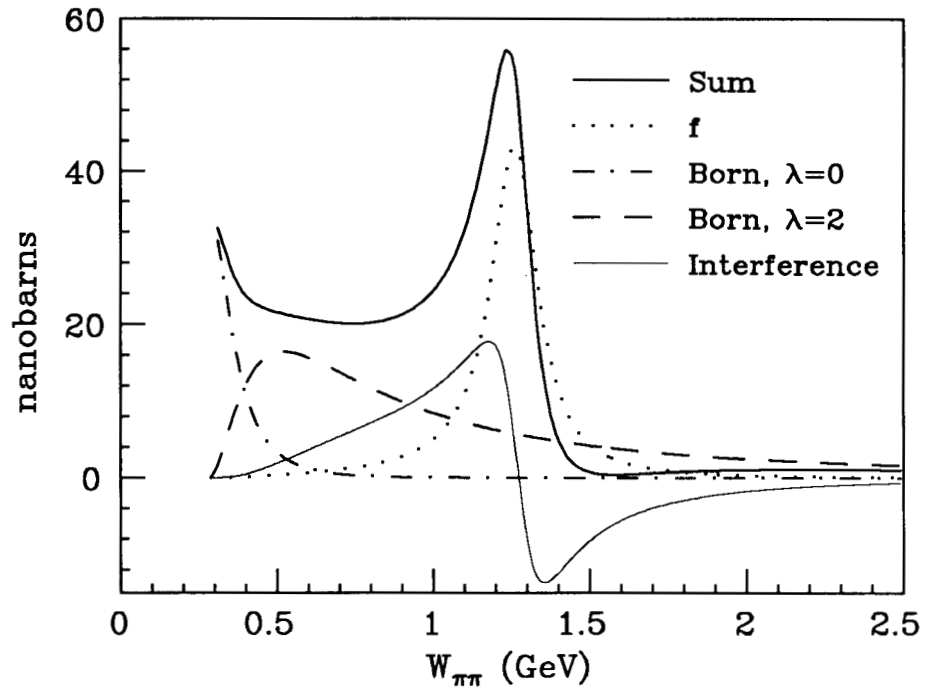

Figure 7.7. Prediction for the $\gamma\gamma \to \pi^+\pi^-$ cross section at $\theta = \pi/2$, assuming a simple model of the Born term plus the helicity-two Breit-Wigner amplitude, with interference of the helicity-two amplitudes. $\Gamma_{\gamma\gamma} = 3.0\,\mathrm{keV}$ is assumed, and the partial waves are not required to satisfy the unitarity condition.

The energy dependence of $\Gamma(s)$ in the Lyth model is determined by Eqn. 7.32. Note that it affects both the phase and the magnitude of the resonance amplitude. The phase is consistent with the measurements shown in Fig. 7.4, which is the same data as that which Mennessier used to fit his model. However, the energy dependence of $\Gamma_{\gamma\gamma}$ in the numerator of the Breit-Wigner amplitude, Eqn. 7.34, need not be the same as that of $\Gamma(s)$, which appears in the denominator and in the phase. Changing the energy dependence shown in Eqn. 7.32, by changing the parameter a, for example, actually produces only minor changes to the resonance shape itself. That is because although the tails are strongly affected, they already are small. With the interference shown in Fig. 7.7, however, the lower tail of the resonance plays an important part, and its energy dependence becomes significant. As a result, it is difficult to infer from the data whether any additional

contributions, from broad scalar resonances, for example, are necessary in the region between about 0.5 GeV and 1.0 GeV, unless one is very confident with the parameterization of the f. Fortunately, the fitted value of the two-photon width itself remains insensitive to the detailed parameterization of the energy dependence.

Figure 7.8 shows a comparison of the invariant-mass distributions of the two models. Below the f the Mennessier model gives a significantly lower cross section than the other, even though the two use exactly the same formula for the Born term (no unitarization corrections are included in either). When an additional energy dependence, or form factor, defined by

$$\Gamma_{\gamma\gamma} \Rightarrow \Gamma_{\gamma\gamma} \cdot \frac{a + m_f^2}{a + s}, \tag{7.58}$$

is introduced into the resonance contribution of the Mennessier model,[60] then the two models agree quite well for $a = 1.25\,\mathrm{GeV}^2$. It turns out that the Mennessier model fits the data on the low side of the resonance peak very poorly without this modification. Therefore, all subsequent calculations made with the Mennessier model assume the energy dependent width given by Eqn. 7.58.

Now let us consider the effects of requiring the models to satisfy the unitarity condition. Here is where some troublesome differences between the two appear. From Fig. 7.9, one sees that in the resonance region both models suffer a decrease in the cross section at the f peak when unitarity is required, but the decrease is much more severe for the Lyth model. We do not understand why that is so,† since one would expect about the same result from each. In the Lyth model we have required elastic unitarity of the amplitude. Mennessier includes in addition the effects of the coupled KK channel, but the branching ratio of the f to KK is only 3%, and the total inelasticity is but 16%, so it is hard to imagine how that could make much difference. Furthermore, the effect of unitarization when there

† The Mennessier model is essentially a black box to us, in the form of 700 lines of FORTRAN code. Only the details of the Lyth model can be given here.

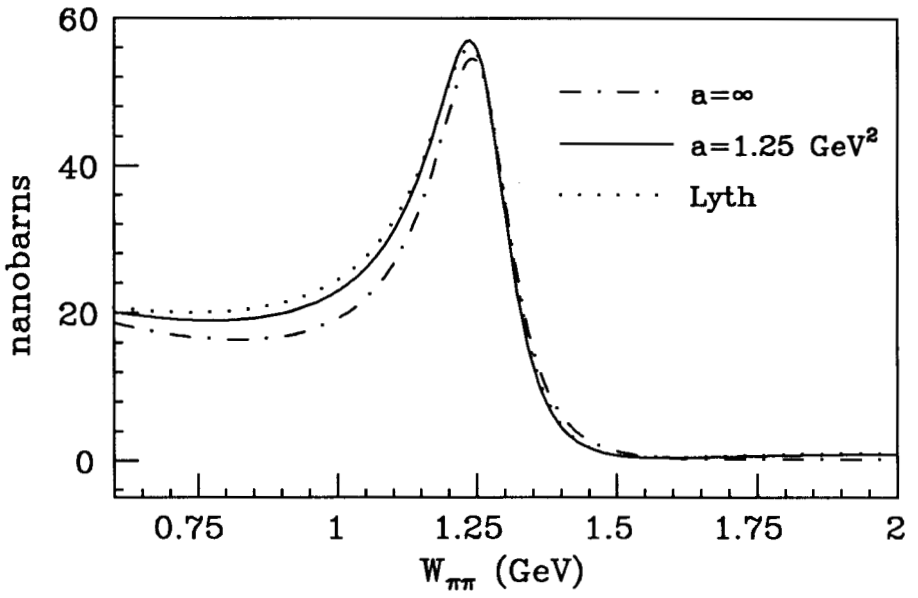

Figure 7.8. Effect of the energy dependence of the f resonance on the mass distribution of the Mennessier model at $\theta = \pi/2$. The parameter a determines the strength of the form factor, which goes at zero as $a \to \infty$. Also shown for reference is the same calculation using the Lyth model.

is no direct coupling of $\gamma\gamma$ to the f, as shown in Fig. 7.6, does not seem to be consistent with what we see in Fig. 7.9 with $\Gamma_{\gamma\gamma} = 3.0\,\text{keV}$. This question has not been resolved, but there is yet another difference to consider.

The two curves shown in Fig. 7.9 of the Lyth model differ from each other only by the addition of an imaginary part, according to Eqn. 7.47, to the *unchanged* real part of the coupling g. The real part of g thus remains $\Re g = m_f[\Gamma_{\gamma\gamma}\Gamma_{\pi\pi}]^{1/2}$, with $\Gamma_{\gamma\gamma} = 3.0\,\text{keV}$. But Lyth defines[53] the two-photon width by $|g| = m_f[\Gamma_{\gamma\gamma}^{\text{lyth}}\Gamma_{\pi\pi}]^{1/2}$. Thus he considers the unitarity correction to be part of the coupling of the resonance to the two photons.

Mennessier's definition is different. The unitarity correction is considered to be part of the Born term, yielding the *unitarized Born term*, to which the "direct coupling" of the resonance to $\gamma\gamma$ is added. Thus in Fig. 7.6, we see an obvious S^* peak and a big effect from the f even though all direct couplings of resonances were set to zero. Also, consider Ref. 61, in which the f signal observed with the

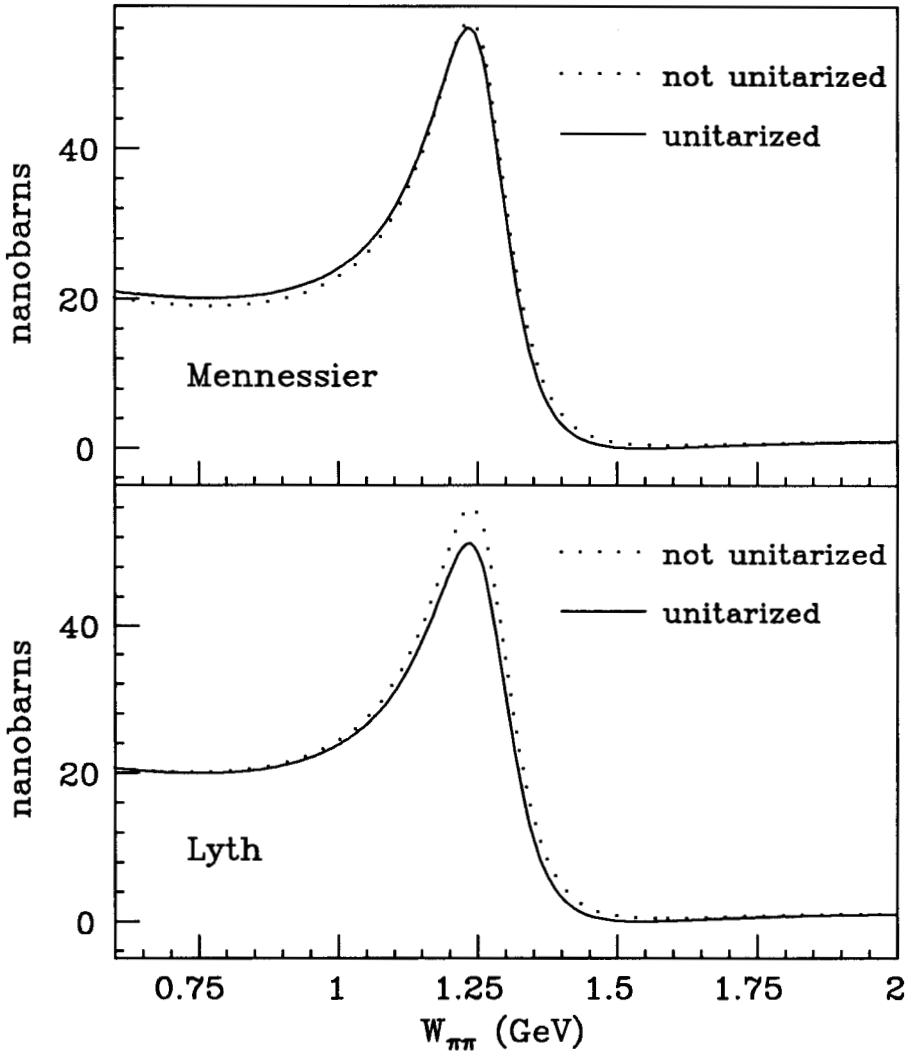

Figure 7.9. The effect of requiring unitarity for the D-wave on both the Lyth and Mennessier models.

CELLO detector is fit by the model of Mennessier. The authors state,

> "...the only free parameter fitted to our data is $\Gamma_{\gamma\gamma}(f_0)$ which describes the 'direct' $\gamma\gamma f_0$ coupling. This does not correspond exactly with the observed f_0 signal since the helicity 2 projection of the Born term may give a small contribution to the f_0 signal by final state scattering effects... $\Gamma_{\gamma\gamma}(f_0)$ is the relevant parameter for comparison with theoretical predictions based on internal meson structure (*e.g.*, the quark model), whereas in evaluating dispersion relations or sum rules the full partial wave amplitudes measured by the fit to the experimental distributions should be used."

It is true that in the quark model, the coupling of photons to a meson must be real, but then the quark model also has no provision for describing the finite width and associated energy dependencies of a resonance. Recall that if the resonance width may be neglected, then the imaginary part of the coupling, as specified in Eqn. 7.47, may also be neglected. Thus it is clear that comparisons with quark model predictions, such as the $SU(3)$ predictions for the ratios of two-photon widths, always will be limited in validity by the simple fact that in reality the tensor mesons have relatively large widths, compared with the pseudoscalar mesons, for example.

Perhaps a more important question about the definition of $\Gamma_{\gamma\gamma}$ is how to relate the charged and neutral pion-pair channels. The non-resonant part of the neutral cross section is small enough that whether the resonant coupling is complex becomes irrelevant—there simply are no significant interference effects. One would like to define $\Gamma_{\gamma\gamma}$ such that, for both the charged and neutral cases, the resonant contribution to the cross section is proportional to it. In other words, the same quantity should be measured whether one studies $\pi^+\pi^-$ data or $\pi^0\pi^0$ data.

Recall that the prediction for $\Im g$ was obtained from considering the sum of the f resonance and the $I = 0$, $J = 2$ projection of the Born term and requiring it to satisfy the unitarity condition. The Born term contains contributions to both $I = 0$ and $I = 2$, while the resonance is only $I = 0$. The unitarization procedure adds a contribution to the $I = 0$ amplitude, but the $I = 2$ amplitude is unchanged. The observed cross section then is calculated by taking the sum of the $I = 0$ amplitude and the unitarized $I = 2$ amplitude, projecting it onto either $|\pi^+\pi^-\rangle$ or $|\pi^0\pi^0\rangle$, according to Eqn. 7.19, and squaring the absolute magnitude. The Born term, of course, vanishes for the neutral final state, but the contribution of the term required to unitarize the $I = 0$ amplitude remains for both the charged and neutral final states. Therefore, in order for the model of Lyth to be consistent, his definition of the two-photon width must be accepted when using his model. A simple physical picture of how the Born term can affect $\gamma\gamma \to \pi^0\pi^0$ in the f

region is to imagine charged pion pairs being formed from the Born term and then resonating in the final state to $\pi^0\pi^0$.

It is not clear exactly how to interpret Mennessier's model. In particular, it is difficult to understand what is the physical significance of the distinction between "direct coupling" of $\gamma\gamma$ to the f and the contribution coming from unitarization. After all, the strong interactions occur on such a short time scale relative to the electromagnetic interactions that they cannot be considered in any meaningful sense to have occurred after and separate from the $\gamma\gamma$ coupling. In any case, in Chapter 8 we give results from data for both definitions and also for the case where no unitarization corrections at all are made. We will see that in fact the experimental errors are small enough for our $\pi^+\pi^-$ measurement that these problems cannot be neglected. Unfortunately, the statistical errors on measurements of the corresponding neutral channel are not yet small enough to check for consistency.

As a final note, we should point out that the f peak observed in $\pi^0\pi^0$ by the Crystal Ball experiment is about 40 MeV, or 3%, low compared with the known value of 1274 MeV. That is about the same magnitude of downward shift as observed in the charged channel. However, it is not clear whether it is real, because the systematic uncertainty in the energy scale is as large as 2%, and the statistical error on the determination of the peak position is 1.1%.† Such a downward shift in the neutral channel is not explained by either model so far considered. Presumably the neutral channel must have some continuum production from such processes as ω exchange, but its level cannot be determined from the available data—certainly there is no obvious large continuum as in the charged channel. Mennessier includes vector meson exchanges in his model and predicts that the $\pi^0\pi^0$ peak is at least 30 MeV above the $\pi^+\pi^-$ peak.‡

---

† The fit of the resonance width in the Crystal Ball data yields $\Gamma_f = 248 \pm 38$ MeV, which is almost two standard deviations high and also is unexplained.

‡ However, in Ref. 61, it is stated that a calculation using the Mennessier model with all vector exchanges set to zero yields a 20 MeV decrease in the position of the $\pi^0\pi^0$ peak. It is not clear

In a recent paper[62] a model has been proposed to explain why the $\pi^+\pi^-$ and $\pi^0\pi^0$ peaks might be identical. The model assumes some sort of $I = 2$ contribution in the f region, from a non-resonant process or an exotic resonance, in addition to the large $I = 2$ component of the $\gamma\gamma \to \pi^+\pi^-$ Born term. This additional $I = 2$ component effectively cancels that of the Born term in the f region. Then the amplitude in the f region is purely $I = 0$, in which case the $\pi^0\pi^0$ cross section must be the same as that for $\pi^+\pi^-$ in shape and half as large.

Nonetheless, we shall continue to assume that the Born term describes the continuum for the charged channel. The deviation of the peak position in the neutral channel could very well be an experimental effect.

---

whether that is consistent with Mennessier's conclusions.

8. Fitting the $\pi^+\pi^-$ Spectra

8.1 Summary of the $\gamma\gamma \to \pi^+\pi^-$ Model

The $\pi^+\pi^-$ data is to be fit to the phenomenological model of Chapter 7, consisting of the Born term calculated from exchange of point pions (Eqn. 7.27) plus terms for the f resonance calculated according to Eqn. 7.34 with the energy dependent width of Eqn. 7.32. The resonance can be formed in both helicity-zero and helicity-two states, so there are two parameters to describe the coupling to two photons: $\Gamma^0_{\gamma\gamma}$ and $\Gamma^2_{\gamma\gamma}$, where $\Gamma_{\gamma\gamma} = \Gamma^0_{\gamma\gamma} + \Gamma^2_{\gamma\gamma}$. The resonant partial wave amplitudes of Eqn. 7.34 must be multiplied by the appropriate angular factors, as given in Eqn. 7.22, in order to obtain the full amplitudes. Furthermore, the amplitudes are forced to satisfy the unitarity condition of Eqn. 7.43 by the addition of an imaginary part to the resonant coupling, according to Eqn. 7.47. However, no unitarity correction is made for the helicity-zero amplitude, because the $J = 2$ part of the helicity-zero Born term is negligible in the f region.

In summary, the cross section is given by

$$
\begin{aligned}
\frac{d\sigma}{d\Omega}(\gamma\gamma \to \pi^+\pi^-) =& \tfrac{1}{2}\left|B_0(s,t) + 5\sqrt{\tfrac{2}{3}}\, d^2_{0\,0}(\theta) R^0_{2\,0}(s)\right|^2 \\
&+ \tfrac{1}{2}\left|B_2(s,t) + 5\sqrt{\tfrac{2}{3}}\, d^2_{2\,0}(\theta) R^0_{2\,2}(s)\right|^2 , \\
\text{where} \quad d^2_{0\,0}(\theta) =& \tfrac{3}{2}\cos^2\theta - \tfrac{1}{2} , \\
d^2_{2\,0}(\theta) =& \tfrac{\sqrt{6}}{4}\sin^2\theta , \\
\text{and} \quad R^0_{2\,\lambda}(s) =& \tfrac{2}{\sqrt{s}} T^0_{2\,\lambda}(s) = \frac{2}{\sqrt{s}} \frac{g_\lambda(s)}{m_f^2 - s - i m_f \Gamma(s)} , \\
g_0(s) =& m_f \left[\Gamma_0(s)\Gamma_{\pi\pi}(s)\right]^{1/2} , \\
g_2(s) =& m_f \left[\Gamma_2(s)\Gamma_{\pi\pi}(s)\right]^{1/2} + i\sqrt{\tfrac{2}{3}} m_f \Gamma(s) \mathcal{B}_{2\,2}(m_f^2) .
\end{aligned}
\tag{8.1}
$$

Recall that $\Gamma_{\pi\pi}(s) = 0.843 \cdot \Gamma(s)$ and that the s dependence of $\Gamma(s)$ is given by Eqn. 7.32. The s dependence of $\Gamma_0(s)$ and $\Gamma_2(s)$ also is given by Eqn. 7.32, but with m_π replaced by $m_\gamma = 0$. This cross section is multiplied by the appropriate

$\gamma\gamma$ luminosity function to give the prediction for $e^+e^- \to e^+e^-\pi^+\pi^-$, and finally, the two-photon widths to be fitted are defined by the expressions

$$\begin{aligned} |g_0|^2 &= m_f^2 \Gamma^0_{\gamma\gamma} \Gamma_{\pi\pi}(m_f^2) \\ |g_2|^2 &= m_f^2 \Gamma^2_{\gamma\gamma} \Gamma_{\pi\pi}(m_f^2). \end{aligned} \tag{8.2}$$

Thus the complete two-photon width may be written as

$$\begin{aligned} \Gamma_{\gamma\gamma} &= \Gamma^0_{\gamma\gamma} + \Gamma^2_{\gamma\gamma} \\ &= \Gamma_0(m_f^2) + \Gamma_2(m_f^2) + \frac{\left[\Im g_2(m_f^2)\right]^2}{m_f^2 \Gamma_{\pi\pi}(m_f^2)} \\ &= \Gamma_0(m_f^2) + \Gamma_2(m_f^2) + 0.257\,\text{keV}. \end{aligned} \tag{8.3}$$

This corresponds to the definition by Lyth. The definition of $\Gamma_{\gamma\gamma}$ used by Mennessier is roughly the same as that of Eqn. 8.3 without the additional 0.257 keV added (see Section 7.6).

8.2 The Fitting Method

The fit itself may be done in two ways. Either the true $\pi^+\pi^-$ spectra are unfolded from the data and then compared directly with the calculation, or else the detector effects are folded into the Monte Carlo calculation, giving Monte Carlo spectra to be compared directly with the data. We take the latter approach for reasons of convenience. The Monte Carlo prediction for the pion spectrum is added to the QED prediction for the muon spectrum plus the estimates of the other minor backgrounds. That sum is compared to the uncorrected data. The precise normalizations of the backgrounds are allowed to vary within experimental errors and hence depend on the results of the fit.

There are several parameters which are adjusted simultaneously in the fit besides the two-photon widths. However, that does not mean that there is a lot of freedom available to fit the model to the data, because all parameters except for

the two-photon widths are considered to be known within certain error limits and are constrained to remain within those limits. That is done by adding a penalty function to the χ^2.† For n bins in the data and Monte Carlo and m constrained parameters, we have

$$\chi^2 = \sum_{i=1}^{n} \frac{(y_i - y_i^{\mathrm{mc}})^2}{\sigma_i^2} + \sum_{j=1}^{m} \frac{(p_j - \bar{p}_j)^2}{\sigma_{p_j}^2} . \tag{8.4}$$

The y_i are the bin contents, and the p_j are the adjustable parameters, $\bar{p}_j$ their nominal values, and σ_{p_j} their uncertainties. In addition, we will consider some fits in which the Born terms and the interference terms are multiplied by factors (most appropriately termed *fudge factors*) which are allowed to vary freely in the fit in order to judge the sensitivity to some assumptions made in the model.

In cases where an assumption is made to constrain to a fixed value the ratio $\Gamma^0_{\gamma\gamma}/\Gamma^2_{\gamma\gamma}$, only the invariant-mass distribution is included in χ^2. When the ratio is allowed to vary in the fit, then it is necessary to include in χ^2 the distribution of $\cos\theta_{\mathrm{cms}}$ as well.

The complete list of parameters which may be adjusted simultaneously in the fit is

1.	The $\gamma\gamma$ width of the f.	$\Gamma_{\gamma\gamma}$
2.	Ratio of widths.	$\Gamma^0_{\gamma\gamma}/\Gamma^2_{\gamma\gamma}$
3.	Helicity-one contribution.	$\Gamma^1_{\gamma\gamma}/\Gamma_{\gamma\gamma}$
4.	The unitarity correction.	$\Im g_2(m_f^2) = (2.5 \pm 0.7) \cdot 10^{-4}\,\mathrm{GeV}^2$
5.	The f mass.	$m_f = 1.274 \pm 0.013\,\mathrm{GeV}$
6.	Full width of the f.	$\Gamma_f = 0.178 \pm 0.020\,\mathrm{GeV}$
7.	Effective luminosity.	$\mathcal{L}_{\mathrm{eff}} = 102.3 \pm 2.3\,\mathrm{pb}^{-1}$
8.	The η' background.	$N_{\eta'} = 468 \pm 87$ events
9.	The K^+K^- and $p\bar{p}$ background.	$N_{\mathrm{tof}} = 342 \pm 34$ events

† Doing the fit by minimizing χ^2 assumes gaussian, rather than Poisson, distributions for the contents of each bin. In this case that is a very good approximation, because the number of events is greater than 200 for every bin of the untagged data.

10. The remaining background. $N_{\rm had} = 150 \pm 50$ events
11. $\pi^+\pi^-$ efficiency error at 0.6 GeV. $\varepsilon_1^\pi = 0 \pm 0.10$
12. $\pi^+\pi^-$ efficiency error at 2.0 GeV. $\varepsilon_2^\pi = 0 \pm 0.05$
13. Fudge factor for the Born term. $\alpha_B = 1$
14. Fudge factor for the interference. $\alpha_I = 1$

The values given here are appropriate for the untagged analysis, although nonzero $\Gamma^1_{\gamma\gamma}$ is considered only in the tagged analysis. The error on the f mass has been increased over the published value to account for uncertainty in the energy scale of the experiment. Parameter number ten refers to the hadronic background estimated from the number of pion-pair events found with non-zero charge. It and parameters eight and nine refer only to background normalizations; the shapes of the backgrounds are fixed. Note that these backgrounds are almost insignificant, especially in the f region, so the normalization parameters introduce little additional freedom into the fit. Normally α_B and α_I are fixed at unity.

Parameters 11 and 12 deserve some further discussion. They refer to Eqn. 6.3, which gives the uncertainty limits on the measurement of the detection efficiency as a function of the invariant mass. The fit allows the normalization of the $\pi^+\pi^-$ Monte Carlo to vary within the limits given by Eqn. 6.3, but the individual bins are not allowed to vary independently. Only the normalization corrections at the upper and lower W limits may vary independently—the corrections for each of the bins in between are determined by those at the upper and lower limits by Eqn. 6.3, which represents a smooth parabola with zero slope at the upper limit.

Since the theoretical model must be calculated by a large number of Monte Carlo iterations, then it is not completely straightforward to vary simultaneously all parameters for the purpose of doing the fit. But a method has been found which works well and is efficient. It relies upon the use of weighted events in the Monte Carlo. When generating events, the dominant $1/W^3$ behavior of the cross section is produced by an analytic change of variables (see Appendix B for a discussion of importance sampling in Monte Carlo integration), and all remaining factors are

lumped together to produce an event weight. Instead of using a rejection algorithm to produce unweighted events, one may simply accumulate histograms of weighted events. Such an approach is the more efficient one, unless the detector simulation is very long and there is a large fraction of events with very small weights.

The method also relies on the fact that, for all but two of the parameters, the $\pi^+\pi^-$ prediction plus background may be expanded into a sum of terms such that the parameters appear as factors multiplying various terms. That obviously is the case for the normalization corrections of the various backgrounds. Also, the correction to $\mathcal{L}_{\text{eff}}$ is a factor multiplying both the $\mu^+\mu^-$ and $\pi^+\pi^-$ predictions, while the pion efficiency correction multiplies only the $\pi^+\pi^-$ prediction. The mass and width of the f are exceptions and are handled by a special technique. For the other parameters, we define two more factors by $\Gamma_0 \Rightarrow \alpha_0\Gamma_0$ and $\Gamma_2 \Rightarrow \alpha_2\Gamma_2$, so the cross section in Eqn. 8.1 may be written as

$$\begin{aligned}
\frac{\mathrm{d}\sigma}{\mathrm{d}\Omega} =& \alpha_B \frac{\mathrm{d}\sigma_B}{\mathrm{d}\Omega} + \tfrac{1}{2}\alpha_0 g_0^2 R_0^2 + \sqrt{\alpha_0}\,\alpha_B\alpha_I g_0 B_0 R_0 \cos\delta \\
&+ \tfrac{1}{2}\alpha_2(\Re g_2)^2 R_2^2 + \sqrt{\alpha_2}\,\alpha_B\alpha_I(\Re g_2) B_2 R_2 \cos\delta \\
&+ \tfrac{1}{2}(\Im g_2)^2 R_2^2 - \alpha_B\alpha_I(\Im g_2) B_2 R_2 \sin\delta\,, \\
\text{where}\quad R_\lambda \equiv& 5\sqrt{\tfrac{2}{3}}\, d^2_{\lambda 0}(\theta)\frac{2}{\sqrt{s}}\left[(m_f^2 - s)^2 + m_f^2\Gamma(s)^2\right]^{-1/2}\,, \\
\frac{\mathrm{d}\sigma_B}{\mathrm{d}\Omega} =& \tfrac{1}{2}\left(B_0^2 + B_2^2\right)\,, \\
\tan\delta =& \frac{m_f\Gamma(s)}{m_f^2 - s}\,.
\end{aligned} \tag{8.5}$$

In the Monte Carlo calculation, a weight is calculated for each of the seven terms, assuming some nominal values for the two radiative widths. Furthermore, for all but the first term, a different weight is calculated for each of twenty-five combinations of values for the f mass and width. After the detector simulation, weighted histograms of both the W and $\cos\theta_{\text{cms}}$ distributions are produced for each of the total of 151 weights. To allow for the fitting program to have access to values of m_f and Γ_f between those included in the 5×5 arrays, each array,

one for each bin of each of the six terms, is interpolated by bicubic splines before beginning the iterations of the fit. Thus the fitting program is able quickly to add up the cross section defined by Eqn. 8.5 for any set of values of the 13 parameters (except that the values of m_f and Γ_f are limited to the range of the spline fits). Since all of the weights are calculated in a single Monte Carlo job, and every weight in a single event is calculated for the same W and $\cos\theta_{\rm cms}$, then there are no statistical fluctuations of one term of Eqn. 8.5 relative to another. Therefore, the statistical error of the sum of terms is just a linear sum of the statistical errors of the individual terms (the resulting error is the same as if all terms had been added together in the Monte Carlo job and accumulated into a single histogram). Finally, the general fitting program MINUIT[63] makes the job of fitting the Monte Carlo histograms to the data easy, convenient, and reliable.

8.3 Fit Results for the Untagged Analysis

In this section we compare the results for the fit of the f two-photon width under various theoretical assumptions. First, let us consider the most simple model, in which no unitarization corrections are made and the f is assumed to be produced only with helicity-two.

8.3.1 Fit to the $\pi^+\pi^-$ Model Without Unitarization

The theoretical model is almost identical to that used in the *1984* publication of DELCO results on $\gamma\gamma \to \pi^+\pi^-$.[64] There are only three differences: First, the parameterization of the energy dependent width is different. In Ref. 64 a form due to Blatt and Weisskopf[65] is used, which gives a result for the phase shift almost identical to that obtained from Eqn. 7.32 with $a = 1\,\mathrm{GeV}^2$. However, using $a = 0.5\,\mathrm{GeV}^2$ gives a better fit to the data shown in Fig. 7.4. The second difference is that Ref. 64 assumes an energy dependence for $\Gamma_{\gamma\gamma}$ according to $\Gamma_{\gamma\gamma}(s) = (\sqrt{s}/m_f)\Gamma_{\gamma\gamma}$, whereas the form used here is Eqn. 7.32 for both $\Gamma_{\gamma\gamma}$ and $\Gamma_{\pi\pi}$. Finally, Ref. 64 uses a value for the branching ratio of the f to $\pi\pi$ which is

1.5% lower than the value now found in Ref. 6. These differences all are minor, and one finds that the two predictions can only barely be distinguished from each other on a plot like that found in Fig. 7.7.

The invariant-mass spectrum to which the Monte Carlo predictions are fit is shown in Fig. 5.7*a*. When only the two-photon width is allowed to vary in the fit and only the points in the range from 0.95 GeV to 1.40 GeV are included in the fit, the result is $\Gamma_{\gamma\gamma} = 2.68 \pm 0.07$ keV. The χ^2 for the nine bins of data included over the range of the f peak is 6.7. Below the f peak the Monte Carlo prediction is on average about 7% higher than the data, but that is within the uncertainty limits on the trigger efficiency in that range. From this we conclude that the model gives a reasonable fit to the data even with the efficiencies and effective luminosity fixed exactly at the measured values. Also, the statistical error on the two-photon width coming only from fluctuations in the bins of the data and Monte Carlo is 0.067 keV, or 2.5%. However, we know that the efficiencies and effective luminosity, and even the f mass and full width, can be varied considerably about the measured values and still be within experimental errors. This reduces the predictive power of the model, allowing it to fit the data more closely and resulting in systematic errors on the two-photon width which are much larger than the statistical error.

Table 8.1 shows in detail the results of allowing all of the experimental parameters to vary within their known error limits. The region below the f is included in the fit, and as usual, the two-photon width is allowed to vary freely. All of the parameters remain within their error limits, including the f mass and full width. Note that the fitted error estimates for m_f and Γ_f actually are smaller than the constraints imposed on them in the fit. In fact, if m_f and Γ_f are allowed to vary completely freely in the fit, they still remain within their error limits. However, the data in the low range of W prefer that the $\pi^+\pi^-$ detection efficiency be almost 5% lower at $W = 0.6$ GeV than it was measured to be, and the effective luminosity is decreased by 1.5% in order to predict fewer muon pairs and pion pairs in that region. Furthermore, by shifting the f mass down slightly, the Monte Carlo

prediction fits in the peak of the f better. All of these changes are well within the respective error limits, but they together have the effect of increasing the fitted two-photon width by 4% over the value obtained when all other parameters are fixed. Nonetheless, this shift in $\Gamma_{\gamma\gamma}$, though greater than the statistical error, is well within the total error shown in Table 8.1 of $\pm 7\%$.

If only those bins with $0.95 \leq W \leq 1.40$ are included in the fit, then the result is $\Gamma_{\gamma\gamma} = 2.71^{+0.26}_{-0.25}$ keV, which is almost the same as the result obtained when all parameters but $\Gamma_{\gamma\gamma}$ were held fixed, although here the systematic errors are included. Another systematic error which has not yet been included is the uncertainty in the momentum resolution of the experiment (see Section 3.1). The fits presented so far have assumed that the resolution of the track curvature is $\sigma_\kappa/\kappa = 7\%$. When it is varied from 8% down to 6%, the two-photon width from the fit varies by less that the statistical precision of 2.5%, while the fitted value of the full width varies from 0.164 GeV up to 0.187 GeV. Thus the result is not sensitive to the value assumed for the momentum resolution, and the observed f peak is completely consistent with the known value of the f width.

A check is made on the validity of using the Born term to describe the continuum below and under the f by doing a fit with the coefficient α_B left free to vary. The range in W from 0.6 GeV to 1.4 GeV is included in the fit, and the main effect is that α_B decreases by 7% from unity, while the $\pi^+\pi^-$ trigger efficiency returns to its measured value. The value for the two-photon width increases by only 1.4%, while the size of the error estimate increases by 0.01 keV. Therefore, within experimental errors the Born term describes the continuum adequately at least below the f peak, and the fitted two-photon width is not changed when the normalization of the Born term is allowed to vary freely.

Figure 8.1 shows a histogram of the data with all of the background subtracted. It is compared with the $\pi^+\pi^-$ prediction as given in Table 8.1. Note that the fit is excellent for $W \leq 1.40$ GeV, but above that and up to 1.75 GeV the data are much higher than the prediction and are only slightly lower than

Table 8.1. Results of fitting the $\pi^+\pi^-$ model with no unitarization and with the helicity-zero two-photon width of the f fixed to zero. More complete definitions of the parameters may be found in Section 8.2.

	Parameter	Fit Value		Lower Error	Upper Error
1.	$\gamma\gamma$ width	2.82	keV	-0.19	+0.20
5.	f mass	1.262	GeV	-0.004	+0.004
6.	full width	0.169	GeV	-0.011	+0.011
7.	$\mathcal{L}_{\text{eff}}$	100.7	pb^{-1}	-1.2	+1.2
8.	η' background	423	events	-83	+83
9.	$K\overline{K}, p\overline{p}$ background	336	events	-34	+34
10.	$Q \neq 0$ background	150	events	-50	+50
11.	ε_1^π	-0.047		-0.085	+0.086
12.	ε_2^π	-0.003		-0.050	+0.050

Covariance Matrix Correlation Coefficients

	1	5	6	7	8	9	10	11
5	-0.056							
6	0.490	0.366						
7	0.011	-0.248	-0.073					
8	0.063	-0.064	-0.052	-0.037				
9	-0.043	-0.015	-0.026	0.004	-0.007			
10	-0.013	-0.017	-0.036	-0.023	-0.014	-0.009		
11	-0.324	0.297	-0.217	-0.803	-0.101	-0.002	-0.019	
12	-0.729	0.104	-0.082	0.021	-0.016	0.001	-0.004	-0.023

Fit range: $0.6 < W < 1.4$ GeV 16 bins
χ^2=11.8

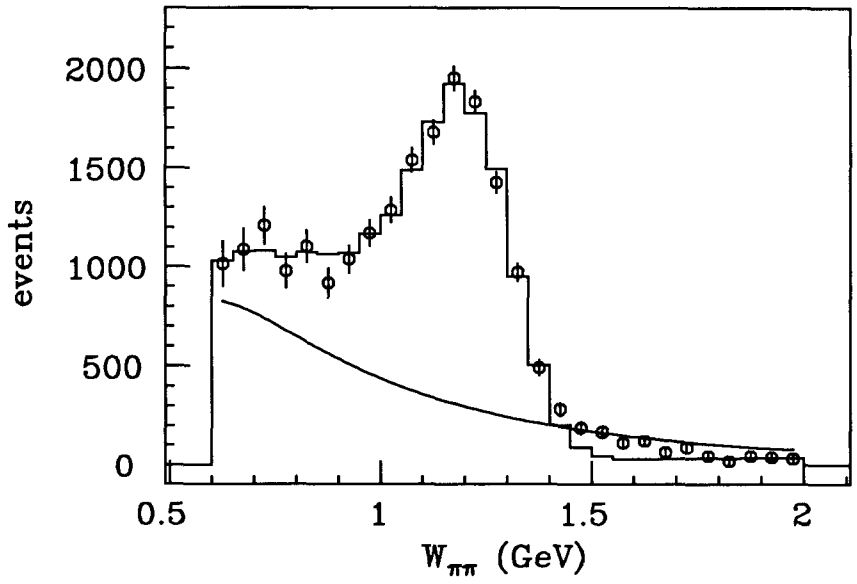

Figure 8.1. The background-subtracted $\pi^+\pi^-$ invariant-mass spectrum compared with the Monte Carlo prediction (solid histogram) with no unitarization and with no helicity-zero coupling to the f. The smooth curve shows the prediction for $\pi^+\pi^-$ from the Born term alone. The values of all the fit parameters are as given in Table 8.1.

the spectrum predicted from the Born term alone. It is the interference with the resonance which makes the prediction so low in that region. Why the full effect is not seen in the data is not known.

If the entire range of W is included in the fit, then as expected, the effective luminosity is increased by almost 2% in order to reduce the data above the f peak by subtracting more muon pairs. To compensate then below the f, the $\pi^+\pi^-$ detection efficiency is lowered to the point of being two standard deviations below the measured value. The net result is only a 2% increase in $\Gamma_{\gamma\gamma}$. The fit still is not good above the f peak, with $\chi^2 = 48$ for the entire 28 bins of data. It is clear that this model cannot be used over the full energy range without some modification.

This disagreement above $W = 1.4\,\mathrm{GeV}$ is worrisome because it indicates that something is wrong with the description of the continuum background. It is important to assess what affect this has on the measurement of the two-photon width of the f. It is possible that some of the effect is from non-gaussian tails in the

momentum resolution which are not reproduced by the Monte Carlo simulation. However, the same effect is seen by the *PEP-4/PEP-9* experiment.[5] Most of the disagreement is believed to be genuine.

In Ref. 5 the problem is handled by introducing an arbitrary parameter, which we call α_I, to multiply the interference terms of the cross section. This does yield a good fit over the full energy range, but only with α_I as low as 0.5. When α_I is allowed to vary freely in the DELCO fit, good agreement is achieved over the full energy range ($\chi^2 = 26$ for the 28 bins), but with $\alpha_I = 0.72$ for the best fit. However, the fit forces the f mass down to 1.249 GeV, which is getting rather far from the preferred value. That is to be expected, since the interference is necessary to shift the peak down to the observed position. The best fit for $\Gamma_{\gamma\gamma}$ is raised by only 1.8% compared with the result for $\alpha_I = 1$.

The parameter α_I is justified in Ref. 5 by arguing that one really does not know if the continuum is properly described by the Born term, in which case one cannot be sure that it really is all in helicity two in the f region. However, multiplying the interference terms by a fudge factor is a perversion of the model which makes it difficult to interpret physically. Another possible explanation for the discrepancy is resonance production in the S-wave (perhaps the $\epsilon\,(1300)$). To assess the effect of such a possibility, we try adding an additional non-interfering background to the fit. This is done with a gaussian curve centered at $W_0 = 1.5$ GeV with arbitrary width and height:

$$B(W) = A \exp\left(-\frac{(W - W_0)^2}{2\sigma^2}\right) . \tag{8.6}$$

The best fit over all 28 W bins has $\chi^2 = 15.0$ with $A = 126$ events and $\sigma = 0.13$ GeV. The best fit for $\Gamma_{\gamma\gamma}$ is lower by 3.5% relative to the result fit only on the range $W < 1.4$ GeV and without the gaussian background. Note that adding the gaussian background changes the fitted value of $\Gamma_{\gamma\gamma}$ in the opposite sense from the effect of the fudge factor in the interference term.

Taking into consideration all of the systematic effects, and in particular the effects of changing the region included in the fit and adding the gaussian background of Eqn. 8.6, leads to the result

$$\Gamma_{\gamma\gamma} = 2.77 \pm 0.31\,\text{keV}, \quad (\lambda = 2, \text{ no unitarization}). \tag{8.7}$$

Keep in mind that this result assumes a model which violates unitarity and also that the helicity-zero coupling is assumed to be exactly zero. Since this is identical to the model used in the DELCO analysis of Ref. 64, we may compare the results directly. The result of the analysis of Ref. 64 is $\Gamma_{\gamma\gamma} = 2.70 \pm 0.21\,\text{keV}$. Only about half of the presently available data were used, but the actual reasons for the difference with the present result are systematic. First of all, the analysis of Chapter 6 has been done since then. Reference 64 assumes that the relative detection efficiency of pion pairs compared with muon pairs is independent of energy. Second, in Ref. 64 the correction to $\mathcal{L}_{\text{eff}}$ necessitated by bremsstrahlung from electrons passing through the beampipe and drift chamber material was not made. These two corrections largely cancel each other with respect to the fitted two-photon width, but they do contribute significantly to the estimate of the systematic error.

8.3.2 Effect of Requiring Unitarity

The unitarity correction is added to the model by setting $\Im g_2$ nonzero and allowing it to vary in the fit. If it is allowed to vary completely freely, then one finds that the data give no constraint. That is expected from Fig. 7.9, where it is evident that the correction does not change the shape of the spectrum significantly but only lowers the peak a bit. Therefore, $\Im g_2$ must be constrained to remain within the range of the theoretical prediction of Eqn. 7.57. That is done by using the bounds given by Eqn. 7.57 as gaussian error limits. Assuming such a gaussian distribution cannot be well justified, but the bounds seem conservative enough that the error estimate is not likely to be an underestimate in any case.

We continue to assume that there is no helicity-zero resonance coupling. The result of the fit is in all respects almost identical to that done with no unitarization except that the two-photon width becomes larger and has slightly larger errors. The fitted value arrived at for $\Gamma_{\gamma\gamma}$ when fitting over the range $0.6 \leq W \leq 1.4\,\mathrm{GeV}$ with $\alpha_B = 1$ is $\Gamma_{\gamma\gamma} = 3.44^{+0.23}_{-0.21}\,\mathrm{keV}$. This is assuming the definition given by Lyth, as expressed in Eqn. 8.3. When all systematic effects, such as the dependence on the interval of W included in the fit, are accounted for as in the previous section, the final result for the unitarized model of Lyth, assuming zero helicity-zero coupling, is

$$\Gamma_{\gamma\gamma} = 3.34 \pm 0.35\,\mathrm{keV}, \quad (\lambda = 2,\ \text{unitarized}). \tag{8.8}$$

8.3.3 Comparison with the Mennessier Model

The Mennessier model may also be used to fit the two-photon width of the f. The procedure is similar to that discussed above, except that it is not possible to fit the f mass and full width simultaneously with the two-photon width in this case. It is not possible for us to separate the model into all of its separate terms as is done for the more simple model in Eqn. 8.5. Therefore, Mennessier's program was run once for each of several values of the two-photon width, and the result was interpolated by cubic splines.

Table 8.2 gives the results of the fit when all data up to $W = 1.4\,\mathrm{GeV}$ are included. The χ^2 is not as low as that shown in the fit of Table 8.1, but that is partly due to the inability to adjust the mass and full width of the f. Restricting the fit to only the region of the f peak has the same effect as with the model of the previous section. Taking that into account, plus the effects of changing m_f, Γ_f, and the Monte Carlo momentum resolution within the allowed limits gives the final result for the Mennessier model:

$$\Gamma_{\gamma\gamma} = 2.93 \pm 0.30\,\mathrm{keV}, \quad (\lambda = 2,\ \text{Mennessier}). \tag{8.9}$$

Table 8.2– Results of fitting the Mennessier model to the untagged $\pi^+\pi^-$ data with the helicity-zero two-photon width of the f fixed to zero. More complete definitions of the parameters may be found in Section 8.2.

	Parameter	Fit Value		Lower Error	Upper Error
1.	$\gamma\gamma$ width	3.01	keV	-0.15	+0.16
7.	$\mathcal{L}_{\text{eff}}$	95.8	pb^{-1}	-1.1	+1.1
8.	η' background	412	events	-87	+87
9.	$K\overline{K}, p\overline{p}$ background	342	events	-34	+34
10.	$Q \neq 0$ background	147	events	-50	+50
11.	ε_1^π	-0.043		-0.076	+0.076
12.	ε_2^π	0.00		-0.05	+0.05

Covariance Matrix Correlation Coefficients

	1	7	8	9	10	11
7	-0.052					
8	0.109	-0.049				
9	-0.046	0.002	-0.009			
10	-0.003	-0.022	-0.009	-0.003		
11	-0.088	-0.844	-0.100	-0.004	-0.032	
12	-0.783	0.063	-0.037	-0.001	-0.002	-0.154

Fit range: $0.6 < W < 1.4\,\text{GeV}$ 16 bins
χ^2=14.1

Note that this fit does include Mennessier's unitarization corrections. However, as we have seen in Chapter 7, those corrections have little effect. Furthermore, the definition used here for $\Gamma_{\gamma\gamma}$ is closer to that of the parameter $\Gamma_2(m_f^2)$ in the model given by Eqn. 8.1 (Lyth's model) than it is to $\Gamma_{\gamma\gamma}$ as defined by Eqn. 8.2. The unitarization correction is not considered to be part of the coupling of $\gamma\gamma$ to the f. According to Eqn. 8.3, $\Gamma_2(m_f^2)$ is 0.257 keV less than $\Gamma^2_{\gamma\gamma}$. Com-

paring the fitted value of $\Gamma_2(m_f^2)$ from Eqn. 8.8 with Eqn. 8.9, we find that the Mennessier result is about 5% lower. That is to be expected from the comparison of the two unitarized models shown in Fig. 7.9 and corresponds to more than two standard deviations of the statistical error (the systematic effects are the same for each model).

In summary, the two models fit the data equally well. When no unitarization corrections are made, they give results for $\Gamma_{\gamma\gamma}$ which agree with each other within the systematic errors. The principle differences lie in the definitions of $\Gamma_{\gamma\gamma}$ when unitarization corrections are made and in the fact that unitarization of the Mennessier model produces little change whereas it lowers by several percent the f peak in the Lyth model.

8.3.4 Including the Angular Distribution

It is important to consider the effect of a possible helicity-zero contribution to the resonant coupling, since there is no theoretical justification to assume that it is exactly zero. To do so, it is essential to include into consideration the measured angular distribution. We use the distribution of $\cos\theta_{\rm cms}$ integrated over the range $1.0 \leq W \leq 1.5\,\mathrm{GeV}$, in order to be most sensitive to the angular distribution of pion pairs coming from the f resonance.

First, let us consider the angular distribution alone. There are twelve bins of width 0.05 from $\cos\theta_{\rm cms} = 0$ to the detector limit of $\cos\theta_{\rm cms} = 0.60$. The predicted distribution is a combination of the flat distribution from the Born term interfering with the $d^2_{\lambda 0}(\theta)$ functions from the resonance decay, plus the approximately $(1+\cos^2\theta)/(1-\cos^2\theta)$ distribution from the muon-pair background. The experimental acceptance, given for the most part by the single cut $\cos\theta_{\rm lab} \leq 0.60$, falls sharply from a maximum at $\cos\theta_{\rm cms} = 0$ to zero at $\cos\theta_{\rm cms} = 0.60$ and strongly affects the observed shape. The result of fitting to only the angular distribution is that the data prefer essentially zero contribution from helicity-zero.

The 90% confidence level upper limit is

$$\frac{\Gamma^0_{\gamma\gamma}}{\Gamma^2_{\gamma\gamma}} < 0.15 \qquad \text{(90\% confidence)}. \tag{8.10}$$

It is interesting that this ratio actually is constrained substantially by the invariant-mass distribution alone. It is easy to see why that is so. The spectrum is dominated by the interference effect, which enhances the cross section below resonance and decreases it above. Such an effect does not occur for helicity zero, because the helicity-zero Born term is negligible in the resonance region. In fact, if the coupling is assumed to be only helicity zero, the model predicts far too few events below resonance and far too many above, and the best fit to the invariant-mass spectrum has a χ^2 of 150 for 16 bins (the two-photon width for that fit is 6 keV).

Table 8.3 shows the results of fitting simultaneously to the invariant-mass and angular distributions. Both helicity amplitudes are included, and the unitarization corrections to the helicity-two amplitude are included. Figure 8.2 compares the fitted spectra to the data. The additional systematic effects, such as the dependence on the range of W included in χ^2, are about the same as for the fit with only the invariant mass distribution included. Taking them into account results in

$$\begin{aligned} \Gamma_{\gamma\gamma} &= \Gamma^0_{\gamma\gamma} + \Gamma^2_{\gamma\gamma} = 3.42 \pm 0.37\,\text{keV} \\ \Gamma^0_{\gamma\gamma}/\Gamma^2_{\gamma\gamma} &< 0.14 \quad \text{(90\% confidence)}. \end{aligned} \tag{8.11}$$

Here, Lyth's definition of $\Gamma_{\gamma\gamma}$ (Eqn. 8.3) is assumed.

We have found that the DELCO constraint on the ratio of helicity amplitudes is much better than the Crystal Ball result (compare with Eqn. 1.3). That may be surprising at first, but it is because of the relatively small number of $\pi^0\pi^0$ events observed by the Crystal Ball collaboration. Their advantage lies in being

Table 8.3– Fit of the complete model of Eqn. 8.1 to the untagged $\pi^+\pi^-$ invariant-mass and angular distributions. Definitions of the parameters may be found in Section 8.2.

Parameter	Fit Value		Lower Error	Upper Error
1. $\Gamma_{\gamma\gamma}$	3.51	keV	-0.22	+0.27
2. $\Gamma^0_{\gamma\gamma}/\Gamma^2_{\gamma\gamma}$	0.01		-0.01	+0.13
4. $\Im g_2(m_f^2)$	0.00026	GeV^2	-0.00007	+0.00007
5. f mass	1.266	GeV	-0.005	+0.005
6. full width	0.168	GeV	-0.012	+0.011
7. $\mathcal{L}_{\text{eff}}$	100.8	pb^{-1}	-1.2	+1.2
8. η' backround	416	events	-82	+82
9. $K\overline{K}, p\overline{p}$ background	342	events	-34	+34
10. $Q \neq 0$ background	150	events	-50	+50
11. ε_1^π	-0.070		-0.085	+0.094
12. ε_2^π	-0.002		-0.050	+0.050

Covariance Matrix Correlation Coefficients

	1	2	4	5	6	7	11
2	0.374						
4	0.133	-0.038					
5	-0.106	-0.286	0.099				
6	-0.537	-0.060	0.031	-0.380			
7	0.041	0.116	0.003	-0.251	0.062		
11	-0.265	0.091	-0.016	0.216	0.224	-0.781	
12	-0.641	0.034	0.005	0.124	0.067	0.030	-0.035

Fit range: $0.6 < W < 1.4\,\text{GeV}$, $|\cos\theta_{\text{cms}}| \leq 0.60$ 28 bins
χ^2=17.3

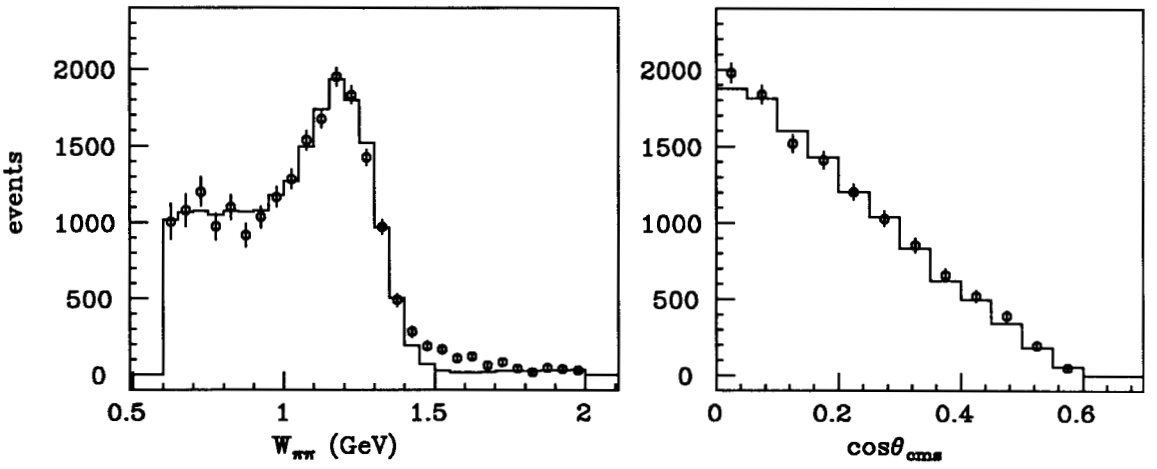

Figure 8.2. Best simultaneous fit to the W and $\cos\theta_{\rm cms}$ distributions of the untagged $\pi^+\pi^-$ data. The points with error bars are the data. The values of the fitted parameters are given in Table 8.3.

able to observe the region $|\cos\theta_{\rm cms}| > 0.80$, where the angular distributions differ greatly. However, their error bar in that region is too large to provide a very good constraint. The region near $|\cos\theta_{\rm cms}| = 0.70$ is not very helpful, since it is around there that the angular distributions cross. Thus DELCO is not at a disadvantage due to its acceptance limit of $|\cos\theta_{\rm cms}| < 0.60$. Also, the Crystal Ball limit may be more stringent if the $\lambda = 1$ fraction (which must be negligible for an untagged experiment) were not included in the fit.

If the ratio $\Gamma^0_{\gamma\gamma}/\Gamma^2_{\gamma\gamma}$ is fixed at the Crystal Ball 1-σ upper limit of 0.51, then the best fit has a χ^2 from the 12 bins of the angular distribution of 16, which is an increase of 9 units from the best fit with the ratio left free. This increase in χ^2 comes from a systematic deviation which is quite obvious when plotted—the Monte Carlo angular distribution with the helicity-zero contribution mixed in falls too rapidly in the region $0.2 < |\cos\theta_{\rm cms}| < 0.6$ relative to the data. Part of the reason for such a good constraint is that all the systematic problems, such as the pion-pair trigger efficiency, have a small effect on the observed angular distribution relative to the effect of the actual decay angular distribution. The major experimental effect is the detector angular acceptance, which is well understood.

8.3.5 *Extrapolating $\Gamma_{\gamma\gamma}$ to $Q^2 = 0$*

For the energy range subtended by the f peak, the EPA luminosity function predicts an average Q^2 of $\overline{Q^2} = 0.006\,\mathrm{GeV}^2$, where Q^2 is defined to be the maximum of $-q_i^2$ for the two photons. To extrapolate the results of the untagged analysis for the two-photon width to $Q^2 = 0$, we assume the GVDM form factor of Eqn. 2.20. It predicts that all the untagged results for $\Gamma_{\gamma\gamma}$ should be multiplied by a factor of 1.014. This change is small compared with the experimental errors, which are 11% or more, so it is not critical whether or not such a correction is made.

8.4 Fit Results for the Tagged Analysis

For the tagged events, the principle interest is to see the Q^2 dependence of the two-photon width of the f. To this end, we ignore for now the question of the unitarity correction and simply compare the result for a simple model of interfering Born plus Breit Wigner amplitudes with the equivalent result obtained at $Q^2 = 0$. The question of the ratio of helicity contributions takes on a greater importance, however. The average Q^2 for events with a single tag in the DELCO luminosity counters is calculated by Monte Carlo from Eqn. 2.18 to be $\overline{Q^2} = 0.44\,\mathrm{GeV}^2$. The authors of Ref. 66 give predictions, based on a non-relativistic quark model, for the Q^2 evolution of the three possible helicity amplitudes of the cross section for $\gamma\gamma \to f$. At $Q^2 = 0$ the $\lambda = 1$ cross section is, of course, zero, and the $\lambda = 0$ cross section is zero as well. But for an experiment with a minimum tagging angle of 0.25 milliradians, the $\lambda = 0$ contribution is 5%, and the $\lambda = 1$ contribution is 25%.

To model the continuum we continue to use the same Born term as given in Eqn. 7.27, except that it is multiplied by the GVDM form factor of Eqn. 2.20. This is justified by the fact that the result gives a reasonable fit below the f peak. The first bin, from $W = 0.6\,\mathrm{GeV}$ to $W = 0.65\,\mathrm{GeV}$, is an exception. It appears to be a factor of two too low, unless either the cross section or the

detector acceptance has some unknown sharply changing behavior at that point, but a statistical fluctuation cannot be ruled out.

Experiments in the past[5,3] commonly have analyzed tagged data with the assumption that the f resonance is produced only in helicity two. But then the results for the Q^2 dependence often are compared with the GVDM form factor, which is inconsistent. GVDM explicitly includes contributions for which one of the colliding photons is longitudinally polarized, which are suppressed only by factors of Q^2/m_V^2 (see Eqn. 2.20) relative to the transverse-transverse contributions. These additional contributions necessarily have helicity one. That is not a serious issue for the description of the continuum, but to measure the resonant cross section accurately within a limited angular acceptance, one must assume the proper angular distribution for the resonance decay. A Monte Carlo calculation of the resonance term multiplied by the GVDM form factor predicts that on average for the DELCO tagging acceptance

$$\frac{\sigma_{LT}}{\sigma_{TT}} = \frac{\Gamma^1_{\gamma\gamma}}{\Gamma^0_{\gamma\gamma} + \Gamma^2_{\gamma\gamma}} = 0.081\,. \tag{8.12}$$

Furthermore, it is safe to assume within this acceptance that the transverse polarization parameter ε of the $\gamma\gamma$ luminosity function (Eqn. 2.16) simply is unity.

The parameters in the fit differ only slightly from those presented in Section 8.2 for the untagged analysis. The background from K^+K^- and $p\bar{p}$ is negligible in this case and is ignored. The other parameters which differ from the untagged analysis are

$$\mathcal{L}_{\text{eff}} = 94.1 \pm 3.3\,\text{pb}^{-1},$$

$$N_{\eta'} = 72 \pm 16\,\text{events},$$

$$N_{\text{had}} = 560 \pm 112\,\text{events}.$$

In addition, the tagged analysis makes use of the helicity-one coupling. The helicity-one contribution is not shown in Eqn. 8.1, but it differs from the other two resonance terms only in the angular distribution. For simplicity, the continuum

production is assumed not to interfere with the helicity-one resonance amplitude, even though using the GVDM form factor implies some helicity-one contribution in the continuum.

First, let us see how well the data can constrain the helicity ratios. When all three helicity contributions are allowed to vary independently, the result is

$$\Gamma_{\gamma\gamma} = 1.42 \pm 0.33\,\mathrm{keV}, \qquad (\overline{Q^2} = 0.44\,\mathrm{GeV}^2), \tag{8.13}$$
$$\Gamma^0_{\gamma\gamma} : \Gamma^1_{\gamma\gamma} : \Gamma^2_{\gamma\gamma} = 40 : 0 : 60\,.$$

Included in the systematic error are the effects of changing the range of W included in the fit, but for the tagged data the results are not very sensitive to that change. In fact, even the prediction above the f peak agrees well with the data, partly because the statistical errors are large compared with the untagged data. The explicit results of such a fit, with the W range restricted to $0.65 < W < 1.4\,\mathrm{GeV}$, are shown in Table 8.4, and Fig. 8.3. The data prefer that there be no helicity-one contribution. If the fit is repeated with the helicity ratios fixed to the prediction of Ref. 66, then χ^2 for the twelve $\cos\theta_{\mathrm{cms}}$ bins increases from 4.8 to 10.7, so that prediction is not well supported by the data. On the other hand, the GVDM prediction of 8% for the $\lambda = 1$ contribution is consistent with the fit shown in Table 8.4. The fit does not constrain very well the ratio of the $\lambda = 0$ to $\lambda = 2$ contributions, since their angular distributions within the acceptance are relatively similar. If the $\lambda = 1$ contribution is taken from GVDM and the $\lambda = 0$ contribution from Ref. 66, and if the result is fit only over the mass spectrum, then χ^2 for the angular distribution is 7.3 for 12 bins. The best fit for the two-photon width then is found to be

$$\Gamma_{\gamma\gamma} = 1.16 \pm 0.18\,\mathrm{keV}, \qquad (\overline{Q^2} = 0.44\,\mathrm{GeV}^2), \tag{8.14}$$
$$\Gamma^0_{\gamma\gamma} : \Gamma^1_{\gamma\gamma} : \Gamma^2_{\gamma\gamma} = 50 : 75 : 875\,.$$

Table 8.4. A fit to the tagged $\pi^+\pi^-$ data with all three helicity amplitudes allowed to vary independently. Complete definitions of the parameters may be found in Section 8.2.

	Parameter	Fit Value		Lower Error	Upper Error
1.	$\Gamma_{\gamma\gamma}$	1.40	keV	-0.29	+0.34
2.	$\Gamma^0_{\gamma\gamma}/\Gamma^2_{\gamma\gamma}$	0.66		-0.66	+1.09
3.	$\Gamma^1_{\gamma\gamma}/\Gamma_{\gamma\gamma}$	0.00		-0.00	+0.13
5.	f mass	1.267	GeV	-0.010	+0.010
6.	full width	0.172	GeV	-0.019	+0.018
7.	$\mathcal{L}_{\text{eff}}$	92.3	pb^{-1}	-2.3	+2.3
8.	η' background	72	events	-16	+16
10.	$Q \neq 0$ background	538	events	-112	+112
11.	ε^π_1	-0.001		-0.095	+0.095
12.	ε^π_2	-0.002		-0.050	+0.050

Covariance Matrix Correlation Coefficients

	1	2	3	5	6	7	11
2	0.876						
3	0.066	-0.033					
5	-0.464	0.504	-0.005				
6	0.245	0.110	0.120	0.152			
7	0.005	0.278	-0.021	-0.113	-0.094		
11	0.046	-0.011	-0.234	0.144	0.132	-0.443	
12	-0.211	0.000	-0.026	0.053	0.018	-0.029	-0.103

Fit range: $0.65 < W < 1.40\,\text{GeV}$, $|\cos\theta_{\text{cms}}| \leq 0.60$ 27 bins
χ^2=11.4

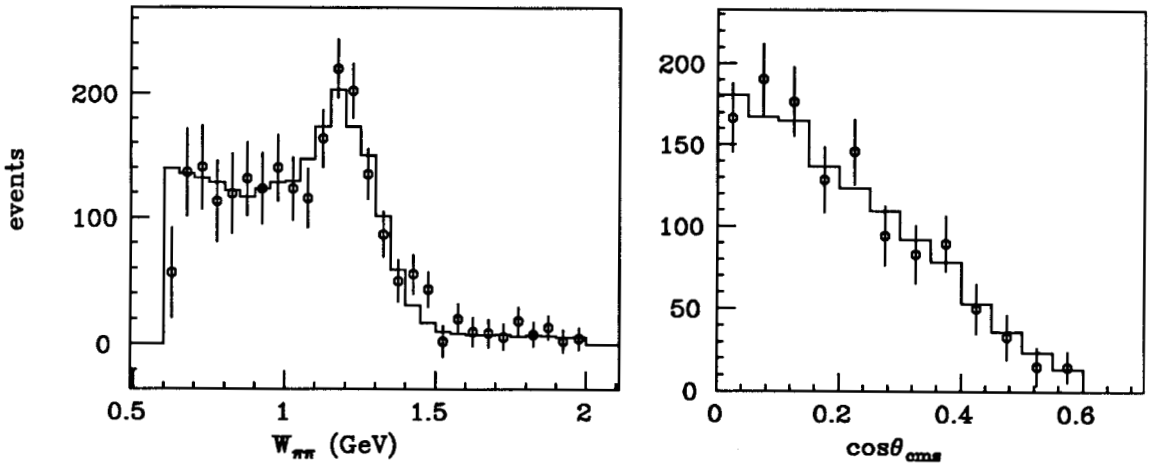

Figure 8.3. Complete fit of the tagged $\pi^+\pi^-$ data with all three helicity amplitudes allowed to vary independently. The results of the fit are detailed in Table 8.4.

8.5 Remarks on the Fitted f Mass

Recall that in Section 7.4.2 we have predicted that the energy dependence of the resonance requires that the parameter m_f actually be 1.284 GeV in order that the pole in the complex plane falls at the point specified in Ref. 6. Thus the best values for m_f presented in the fits of this chapter could be typically 2% low. If that really is so, then it actually is consistent with the K_s mass peak, which is observed to be 2% low (see Section 3.1). The fitted value of $\Gamma_{\gamma\gamma}$, however, is not sensitive to the assumption made for σ_{m_f}. The important point is that the uncertainty in the momentum scale does not affect the normalization of the $\mu^+\mu^-$ subtraction, because the normalization is derived from a measurement of $e^+e^- \to e^+e^-e^+e^-$, which is affected exactly the same by systematic shifts of the momentum scale as are the measurements of muon and pion pairs.

In this chapter we have seen the results of many fits for the two-photon width of the f under various theoretical and experimental assumptions. In Chapter 10 the implications of these results are discussed, and the unfolded spectra for the untagged pion pairs are presented.

9. The Time-of-Flight Analysis

The analysis of kaon and proton pairs differs from that of pion pairs only in that the time-of-flight counters must be used in addition to the other systems. The trigger is the same, although the response to the trigger differs. The tracking is the same, though for kaons it is essential to include in the Monte Carlo simulation the effects of in-flight weak decays. And the Čerenkov counters are used in the same manner to reject electron pairs, although when analyzing kaons and protons they are not as important, since the time-of-flight analysis would reject most electrons anyway. So up to the point of actually analyzing the timing information, the analysis is almost identical to that of the pion pairs. The main exception is that the lower cut on the invariant mass is changed to $W_{KK} > 1.3\,\mathrm{GeV}$, and no explicit upper cut is made. This chapter first discusses the performance of the time-of-flight system and how best to extract the maximum amount of information from it. The resulting analysis then is used to measure the cross sections for $\gamma\gamma \to K^+K^-$ and $\gamma\gamma \to p\overline{p}$.

The system consists of 52 plastic scintillators, 2.5 cm thick and of varying widths and lengths, mounted on the faces of the six aluminum boxes which house the barrel shower counter system and are arranged in a hexagon about the inner detector. Most of the counters actually are longer than the barrel shower counters, but two are cut a few centimeters shorter because of obstructions. Also, in addition to the gaps between sextants, there are a some ϕ gaps which do not appear in the shower counters. Therefore, within the range $-0.6 < \cos\theta < 0.6$, the time-of-flight acceptance is slightly smaller than that of the shower counters. The tracking is not used to define strictly the acceptance. Instead, since there are only two well separated tracks in each event, a fired counter is assumed to be associated with a track if the track passes near to it and there is a good time reading at both ends of the counter.

9.1 Calibration of the Time-of-Flight System

Calibration of the counters is done using the low-energy electrons from two-photon events. In fact, the detector was allowed to be triggered by events with only a single electron detected (usually produced by the process $e^+e^- \rightarrow e^+e^-e^+e^-$), so there is an abundant supply of such electrons for every few hours of data taken. That allows one to remove slight fluctuations in the timing which occurred on the time scale of a few days or less. Large fluctuations which occurred on time scales of several days or more divide the data into 30 run blocks, for which the entire calibration was done separately for each.

Muons and pions, also from two-photon events, also were used in the calibration, but only for measuring light attenuation and pulse-height gain. The corrected pulse height for a particular phototube is calculated from the raw pulse height by the formula

$$a_c = a_r \cdot g_i \cdot e^{\Delta z/\lambda_j} , \tag{9.1}$$

where g_i is the pulse-height gain for the ith phototube, Δz is the distance from the hit to the phototube, and λ_j is the attenuation length for the jth scintillator. For each run block, the g_i and λ_j were adjusted such that the corrected pulse-height distributions from minimum-ionizing particles all consisted of relatively narrow peaks centered about a pulse height which is independent of the phototube and its distance from the position of the hit. Evidence of large variations in counter quality is found in the measured attenuation lengths, which vary from 70 cm to 270 cm.

Then, using electrons, plots were made of the average time residual for each phototube versus the measured pulse height and the distance of the electron hit from the tube, as measured by tracking. The time residual is the measured time minus the time predicted by tracking. Since the electrons travel with essentially the velocity of light, the predicted time is $t_p = t_0 + \ell/c + \Delta z/v_i$, where t_0 is the time of the beam crossing, ℓ is the measured arc length from the interaction point to the counter, and v_i is the effective velocity of light in the scintillator. Corrected

times are determined from the measured times by adding a constant pedestal plus a term in $1/\sqrt{a_r}$ to correct for pulse-height slewing, where a_r is the uncorrected pulse height. An additional polynomial correction is made for very large pulse heights (greater than 15 times minimum ionizing), since there the $1/\sqrt{a_r}$ behavior no longer holds. Also, a nonlinear correction is made for the z dependence when the hit is near the phototube, because in that region the z dependence cannot be fully described by a constant effective velocity. All of these constants for the pulse-height slewing corrections, non-linear z dependence, the pedestals, and the v_i were adjusted iteratively for each phototube or scintillator until the time residuals formed a peak centered about zero and as narrow as possible.

9.2 Monte Carlo Simulation

The performance of the various components of the time-of-flight system must be measured in order to calibrate the Monte Carlo simulation. The same results also are needed in order to calculate probability weights for particle identification. The first priority is that the Monte Carlo simulate the pulse height distribution well. There is no interest in measuring the velocity of electrons, so only the heavy particles need to be handled properly.

For heavy charged particles, the energy deposit in the scintillator is approximately given by[67]

$$\frac{\mathrm{d}E}{\mathrm{d}x} \propto \frac{1}{\beta^2}\left[\ln\left(\frac{2m_e\eta^2c^2}{I}\right) - \beta^2\right], \tag{9.2}$$

where I is a phenomenological constant, βc is the incident particle's velocity, and $\eta^2 = \beta^2/(1-\beta^2)$. Fluctuations about this mean energy deposit are given by a Landau distribution,[68] which forms a peak with a width almost an order of magnitude more narrow than the resolution of the counter system and with a long, low tail extending to pulse heights more than twice as large as that of the peak. The proportionality constant for Eqn. 9.2 is measured for each counter from the position of the peak in a histogram of pulse heights, corrected for attenuation and the incident angle, of minimum-ionizing muons and pions. Also measured for each

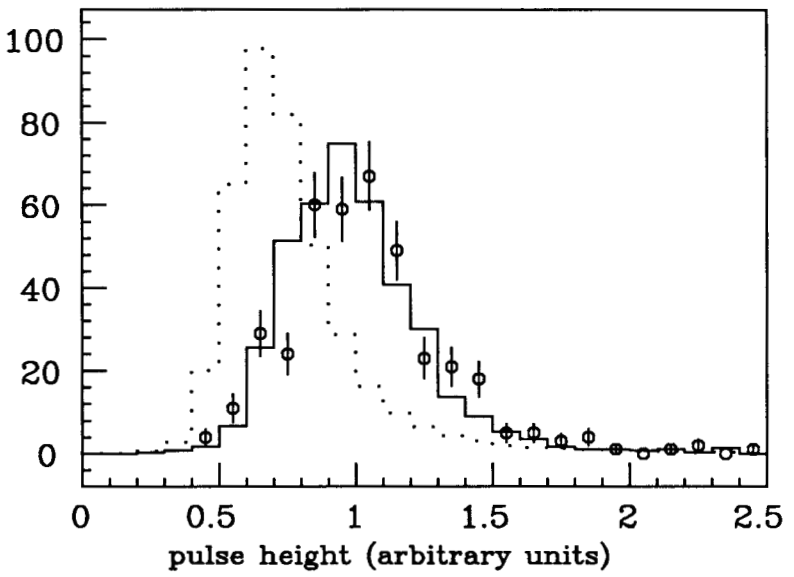

Figure 9.1. Energy deposit of kaons in the time-of-flight counters. The points with error bars show the corrected pulse height distribution for time-of-flight identified kaons, and the solid histogram is the Monte Carlo prediction. The dotted histogram shows the distribution for minimum-ionizing muons and pions, for which the counters were calibrated. The units of the abscissa are arbitrary.

phototube is the width of the pulse height distribution. In the Monte Carlo, the energy deposit is calculated from the path length through the counter by Eqn. 9.2. It then is smeared by a random number drawn from the Landau distribution, attenuated according to the distance from the hit to the tube, and smeared by a random number drawn from a gaussian distribution of the appropriate width. Figure 9.1 shows that the Monte Carlo performs well when predicting the pulse height distribution for incident kaons.

Next, the time resolution must be simulated. There are not enough data to measure accurately the pulse-height dependence of the resolution for each phototube. Instead, what is done is to make a histogram of the time residual of each phototube using only those electrons which produce a pulse height greater than 0.5 gx, where gx is an arbitrary unit defined by the calibration. Since above that cutoff the resolution is almost constant, then the resulting histograms are well

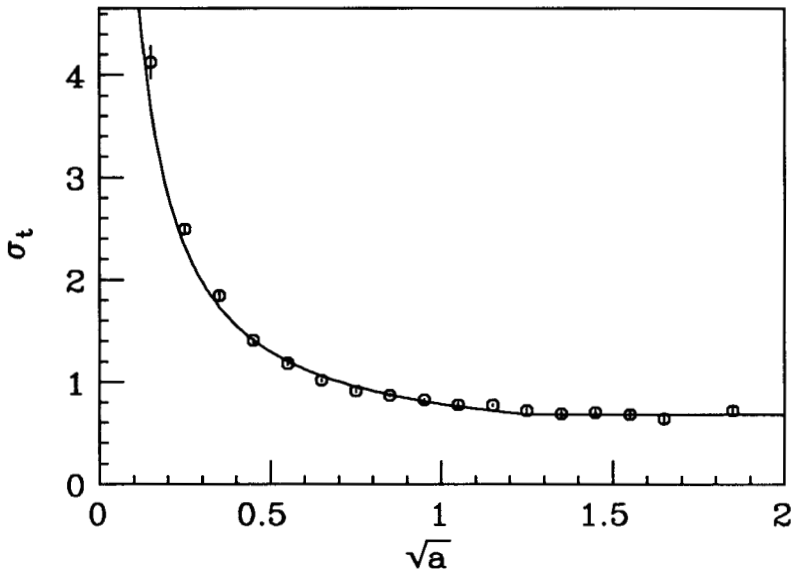

Figure 9.2. The pulse-height dependence of the resolution of the time-of-flight counters. The points show the gaussian widths of the distributions of time residuals divided by phototube-dependent widths. Hence the units of the ordinate are arbitrary. The smooth curve is the best fit to the parameterization described in the text.

fitted by gaussian curves. Then a new set of histograms is made by combining all phototubes and accumulating the time residual divided by the sigma of the gaussian fit for the particular phototube. One histogram is made for each of several ranges of pulse height, and each is fit to a gaussian curve. Figure 9.2 shows a plot of the resulting gaussian widths versus the square-root of the pulse height. The smooth curve is a fit to a constant plus $1/\sqrt{a_r}$, changing to a straight line at about 1.5 gx. This parameterization is what is used in the Monte Carlo simulation and the analysis. As a check of the method, Fig. 9.3 shows a histogram of the time residual divided by the expected resolution for a sample of high-energy muons from the process $e^+e^- \rightarrow \mu^+\mu^-$. The Monte Carlo agrees well with the data, and both samples are well fitted by a gaussian curve of width close to unity and mean close to zero.

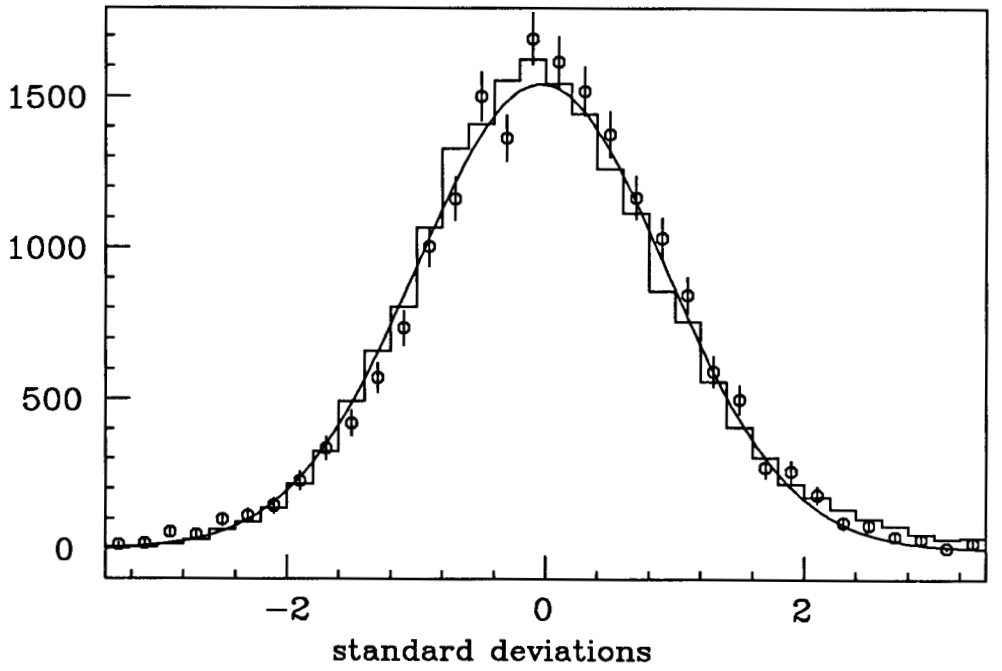

Figure 9.3. The time-of-flight phototube time resolution for 14.5 GeV muons, comparing data (solid histogram) with Monte Carlo (points with error bars). What are plotted are histograms of the time residual divided by the expected resolution. The smooth curve is a fitted gaussian curve with a width of $\sigma = 0.964$ and a mean of $\mu = -0.037$.

9.3 Time Consistency and the Timing Resolution

The time-of-flight analysis relies heavily on tracking information. Especially the momentum measurement is important, because it must be used along with the time-of-flight in order to identify kaons and protons. The tracking cuts of the pion-pair analysis are used again here, but with the addition of one cut. Both tracks in each event are required to have a χ^2 per degree of freedom less than 2.5 for the fit to the drift chamber hits. This helps to reduce the incidence of measurements with large non-gaussian errors. However, the most powerful cut in that respect is one made on the timing information itself. The time is measured independently at both ends of the counter, so it is possible to have a cut which requires the two times to be consistent without biasing the average.

Let t_1 be the time residual measured by the southern end of the counter and t_2 the time residual from the northern end, where time residual is defined to be the difference between the measured time and the time expected for a particle traveling the speed of light. With $\Delta t \equiv t_1 - t_2$, the time consistency is defined to be $\Delta t/\sigma_{\Delta t}$. The main contributions to the error estimate $\sigma_{\Delta t}$ are the timing uncertainties, σ_{t_1} and σ_{t_2}, which are calculated from the measured pulse height by using the parameterization shown in Fig. 9.2. There also is a contribution from tracking which introduces a small anticorrelation between t_1 and t_2. The error in the prediction for the z-position of the point of impact of the particle on the time-of-flight counter (denoted by z_t) comes primarily from errors in the tracking parameters z_0 and $\tan\lambda$. λ is the dip angle of the track, and z_0 is the z coordinate of the track at the point nearest the beam line. The error estimate for z_t is expressed in terms of the tracking covariance matrix by

$$\sigma_{z_t}^2 = \sigma_{z_0}^2 + \rho_{\text{eff}}^2 \sigma_{\tan\lambda}^2 + 2\rho_{\text{eff}} \sigma_{z_0,\tan\lambda}^2 \,. \tag{9.3}$$

The parameter ρ_{eff} is the effective moment arm between where the measurement occurs (in the drift chambers—not at the origin) and the counter. It has been found from Monte Carlo to be approximately half of the actual arc length. Finally, the error estimate for the time consistency is

$$\sigma_{\Delta t}^2 = \sigma_{t_1}^2 + \sigma_{t_2}^2 + 4\sigma_{z_t}^2/v_i \,. \tag{9.4}$$

Figure 9.4 shows a histogram of $\Delta t/\sigma_{\Delta t}$ for the entire sample of non-electron pairs used for time-of-flight analysis. The histogram is well fit by a gaussian curve with $\sigma = 1.05$ and $\mu = 0.003$, verifying the validity of the error estimates. Before continuing the analysis, all events are rejected which do not have two tracks with $\Delta t/\sigma_{\Delta t} < 2.5$. Outside the 2.5σ limit the gaussian curve begins to fall well below the data, which have a long tail extending as far as $\pm 10\sigma$. This cut reduces the data sample by about 5%.

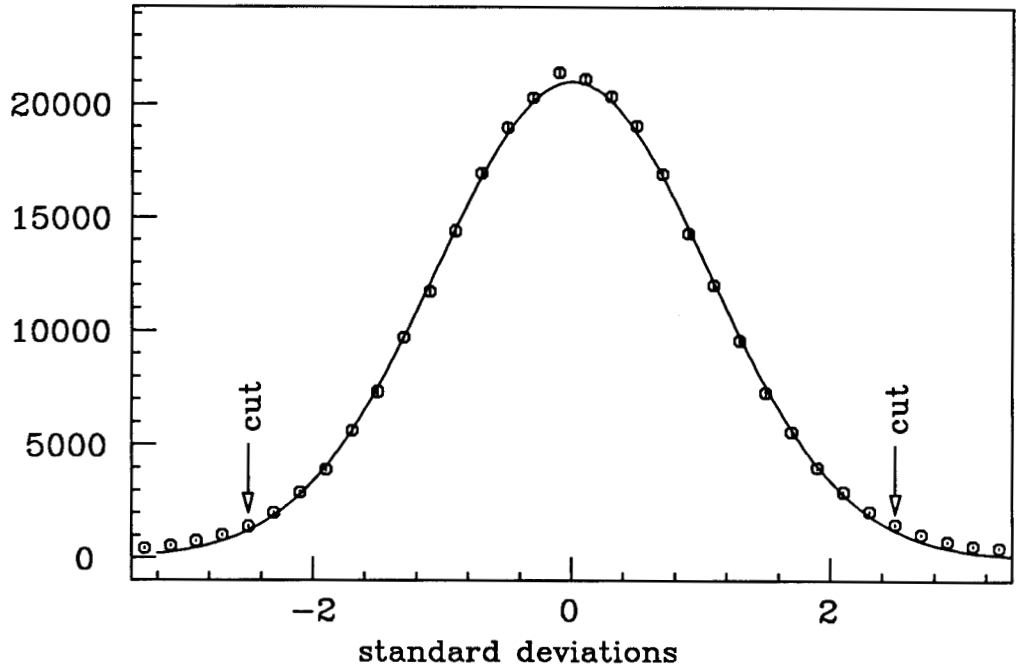

Figure 9.4. Histogram of the time consistency of the two measurements of the time residual made for each minimum-ionizing particle hitting a time-of-flight counter. Each entry of $t_1 - t_2$ is divided by the expected error, as calculated from Eqn. 9.4. The smooth curve is a gaussian fit.

Two more cuts are made on the data to reject tracks with inordinately large expected timing errors. Four of the counters consistently give time residuals more than twice as large as those of all the remaining counters, so events with tracks hitting those counters are not used. And those tracks which have a corrected pulse height, averaged over both phototubes, less than 0.2 gx are rejected because of the large timing errors expected from such a small pulse height. Also, events including tracks with pulse heights greater than 5.0 gx are rejected because they are suspected of being associated with some sort of noise contribution.

The best value for the time residual is a weighted average of t_1 and t_2:

$$\bar{t} = \left(\frac{1}{\sigma_{t_1}^2} t_1 + \frac{1}{\sigma_{t_1}^2} t_2 \right) \cdot \sigma_{\bar{t}}^2 , \qquad \sigma_{\bar{t}} = \left(\frac{1}{\sigma_{t_1}^2} + \frac{1}{\sigma_{t_2}^2} \right)^{-1} . \tag{9.5}$$

Figure 9.5 shows a histogram of $\bar{t}$ for high-energy muons. One does not expect

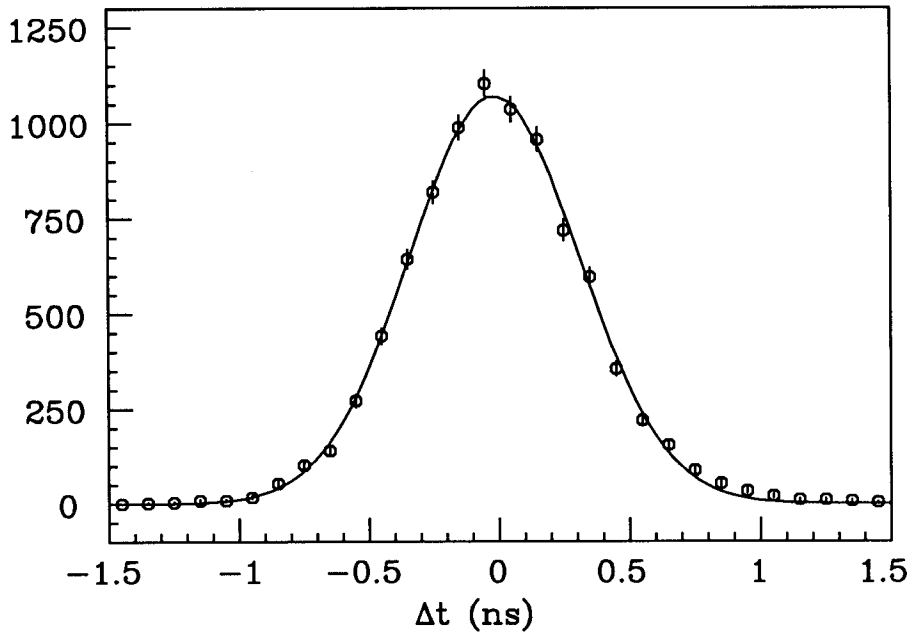

Figure 9.5. The time-of-flight resolution. The histogram is of the time residuals measured from 14.5 GeV muons, and the smooth curve is a gaussian fit.

the shape to be truly gaussian since the entries come from samples with varying resolution. However, as one can see, a gaussian curve does not fit too badly, and its width, $\sigma = 0.327\,\text{ns}$, can be considered to be the average time resolution of the system. When a histogram is accumulated with the time residuals divided by the expected error, then the gaussian fit is excellent. One finds that 0.50% of the entries are outside of the $\pm 3\sigma$ range, compared with 0.26% for a true gaussian distribution. Thus the non-gaussian tails are well suppressed.

Consider now the two-photon data set, which contains kaons and protons as well as muons and pions. The difference in time of flight between particle types decreases as their momentum increases. This can be seen clearly in Fig. 9.6, which shows a scatter plot of the inverse of the measured velocity as a function of the measured momentum. Both tracks are included from all events which have passed all analysis cuts except for cuts on the time of flight itself. It is clear that kaons can be statistically separated from pions only in the region below $p \approx 1\,\text{GeV}$.

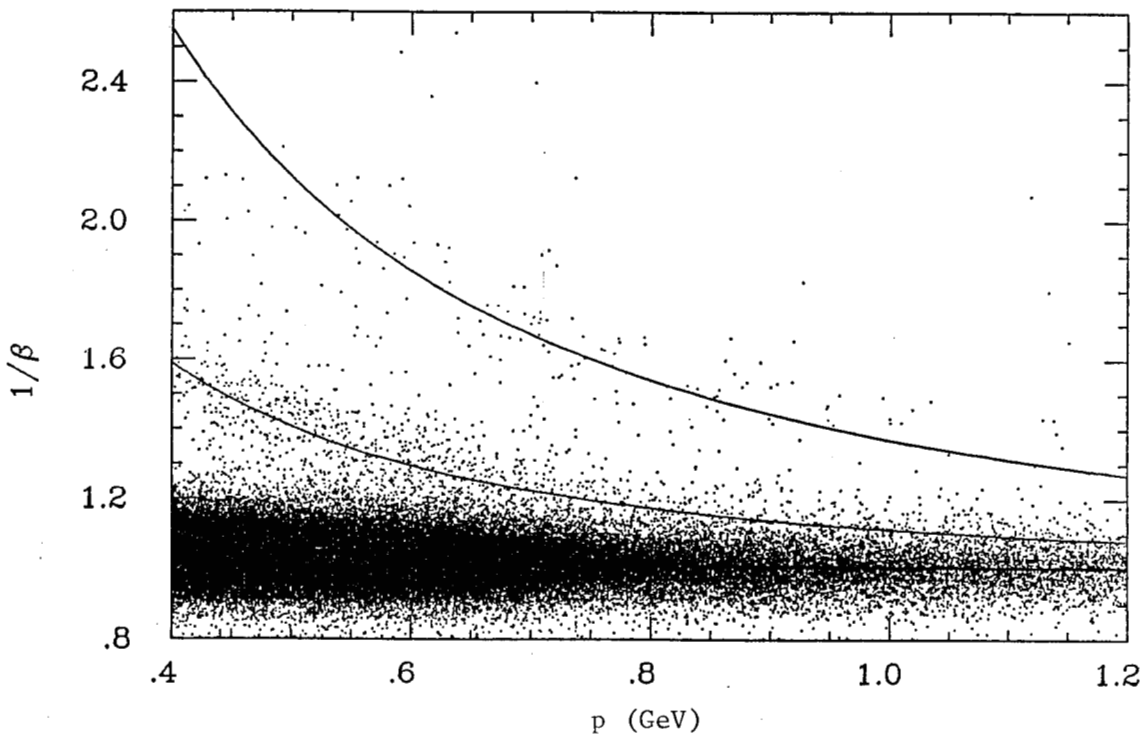

Figure 9.6. The momentum versus the inverse of the measured velocity for tracks from events of the two-photon data set. The smooth curves show the expected trajectories for muons, pions, kaons, and protons.

9.4 Mass Determination and Event Weights

The time-of-flight mass measurement is calculated from the measured momentum and time by

$$m^2 = p^2 \left(\frac{1}{\beta^2} - 1 \right) , \tag{9.6}$$

where $\beta c = \ell/(\bar{t} + \ell/c)$ is the measured velocity. The error in the momentum measurement comes primarily from errors in the curvature κ and the dip angle λ. The correlation between κ and λ is negligible, so we calculate from $p = \sqrt{1 + \tan^2 \lambda}/\kappa$ the linear propagation of errors:

$$\sigma_p^2 = \left(\frac{\partial p}{\partial \kappa} \right)^2 \sigma_\kappa^2 + \left(\frac{\partial p}{\partial \tan \lambda} \right)^2 \sigma_{\tan \lambda}^2 , \tag{9.7}$$

$$\frac{\partial p}{\partial \kappa} = -\frac{p}{\kappa}, \qquad \frac{\partial p}{\partial \tan \lambda} = \frac{1}{\kappa} \frac{\tan \lambda}{\sqrt{1 + \tan^2 \lambda}} .$$

The error estimate for m^2 is given by

$$\sigma_{m^2}^2 = \left(\frac{\partial m^2}{\partial p}\right)^2 \sigma_p^2 + \left(\frac{\partial m^2}{\partial \bar{t}}\right)^2 \sigma_{\bar{t}}^2 , \tag{9.8}$$

$$\frac{\partial m^2}{\partial p} = \frac{2m^2}{p}, \qquad \frac{\partial m^2}{\partial \bar{t}} = \frac{2p^2 \bar{t} c}{l^2} .$$

Figure 9.7 demonstrates that mass resolution is properly calculated and that the errors are very close to being from gaussian distributions. The histogram is of the quantity $(m^2 - m_\mu^2)/\sigma_{m^2}$, so one expects a gaussian shape centered about zero and of unit width.† That is found to be the case to within a few percent of one standard deviation. From the plot with a logarithmic scale, one can see well the non-gaussian tails in the data. They are very small. However, the overall number of muons and pions compared with kaons is enormous, so the tails remain a problem. For the most part, their effects can be avoided by requiring both particles in an event to be positively identified as kaons before calling the event a kaon pair. When the m^2 histogram is accumulated without dividing by the expected resolution for each entry, then a gaussian fit is rather poor, due to a significant variation in the resolution from one event to another. Nonetheless, the σ of the fit, $0.037\,\mathrm{GeV}^2$, can be considered to be approximately the average m^2 resolution of the system.

To identify the particle type, a χ^2 value is calculated for each of the four possible mass hypotheses m_x, where $x \equiv \{\mu, \pi, K, p\}$. The χ^2 is calculated by comparing the expected time residual to both of the measured time residuals:

$$\chi_x^2 = \sum_{i,j=1}^{2} (t_i - t_x)(\sigma^{-1})_{ij}(t_j - t_x) , \tag{9.9}$$

where t_x is the expected time residual for a particle of mass m_x traveling the arc of length ℓ and is given by $t_x = (\ell/\beta_x c)(1 - \beta_x)$, with $\beta_x = 1/\sqrt{1 + m^2/p^2}$. The

† About a quarter of the events in the sample actually are pion pairs. But $m_\pi^2 - m_\mu^2$ is only about 20% of the average resolution of m^2, which is a relatively minor effect.

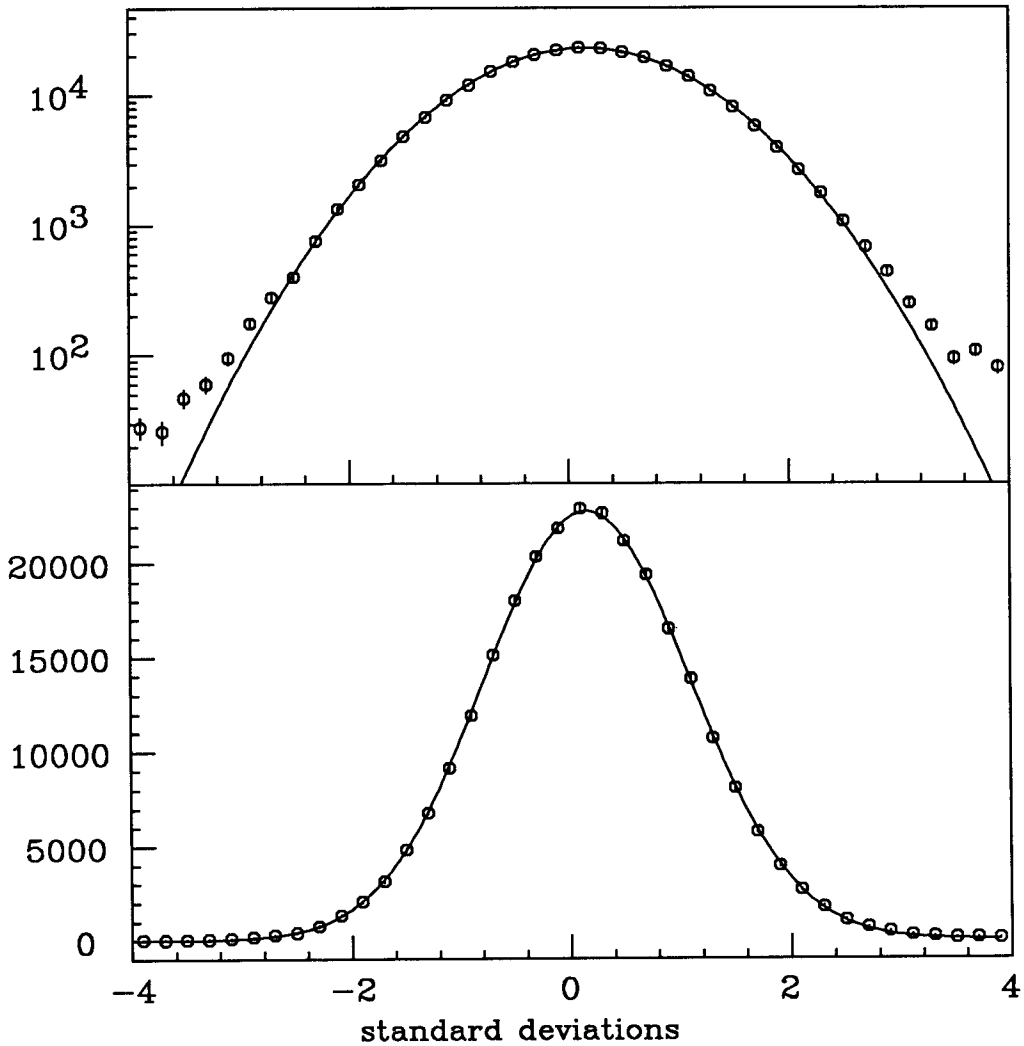

Figure 9.7. The time-of-flight m^2 for non-electron pairs. The histogram is of the difference of the time-of-flight m^2 and m^2_μ, divided by σ_{m^2}, the expected resolution. The solid curve is gaussian with $\sigma = 0.94$ and $\mu = 0.16$.

covariance matrix σ includes the effects of errors in the two time measurements and the errors from p, z_0, and $\tan\lambda$. The non-diagonal terms come from only the last two variables, so a 2×2 derivative matrix is defined:

$$\begin{pmatrix} A_{11} = \dfrac{\partial t_1}{\partial z_0} = -\dfrac{1}{v} & A_{12} = \dfrac{\partial t_1}{\partial \tan\lambda} = -\frac{1}{2}T_x\beta_x^2 \sin 2\lambda - \dfrac{\rho_{\text{eff}}}{v} \\ A_{21} = \dfrac{\partial t_2}{\partial z_0} = \dfrac{1}{v} & A_{22} = \dfrac{\partial t_2}{\partial \tan\lambda} = -\frac{1}{2}T_x\beta_x^2 \sin 2\lambda + \dfrac{\rho_{\text{eff}}}{v} \end{pmatrix}, \tag{9.10}$$

where $T_x \equiv \ell/\beta_x c = t_x + \ell/c$. Also needed are the derivatives of the times with respect to the track curvature:

$$\frac{\partial t_1}{\partial \kappa} = \frac{\partial t_2}{\partial \kappa} = T_x(1-\beta_x^2)p\cos\lambda\,. \tag{9.11}$$

Let $V_{ij}\,\{i,j=1,2\}$ be the 2×2 covariance matrix for z_0 and $\tan\lambda$, as obtained from track fitting. Then the covariance matrix σ takes the form

$$\begin{aligned} \sigma_{ii} &= \sum_{jk} A_{ij}V_{jk}A_{ik} + \left(\frac{\partial t_i}{\partial \kappa}\right)^2 \sigma_\kappa^2 + \sigma_{t_i}^2 \\ \sigma_{12} = \sigma_{21} &= \sum_{jk} A_{1j}V_{jk}A_{2k} + \left(\frac{\partial t_1}{\partial \kappa}\right)^2 \sigma_\kappa^2\,. \end{aligned} \tag{9.12}$$

Finally, the *weight* of a given track is defined for each particle type to be proportional to the gaussian probability that such a particle would produce the measured times:

$$W_x = \frac{1}{\sqrt{\det(\sigma)}} \cdot \exp(-\tfrac{1}{2}\chi_x^2)\,. \tag{9.13}$$

The *event weight* is determined by the product of the weights of the two tracks. To normalize it properly, however, it is necessary to determine roughly the relative abundance of the various event types in the data. To do so, a scatter plot is made of m^2 of the positively charged particle versus m^2 of the negatively charged particle. Figure 9.8 shows such a plot including all data after all analysis cuts have been made, excepting those cuts made on the time of flight itself. The concentrations of events consisting of $p\bar{p}$, $\pi^+\bar{p}$, and π^-p are clearly separated from each other and from the rest of the data, so it is simple to determine the abundances of those event types. The πp events come primarily from beam-gas scattering, as is evident from the fact that more protons than antiprotons are observed. K^+K^- events also are fairly well separated from muons and pions, so an estimate of their fraction is possible. $K\pi$ events are possible, though they must always come from interactions from which at least one final-state particle has been

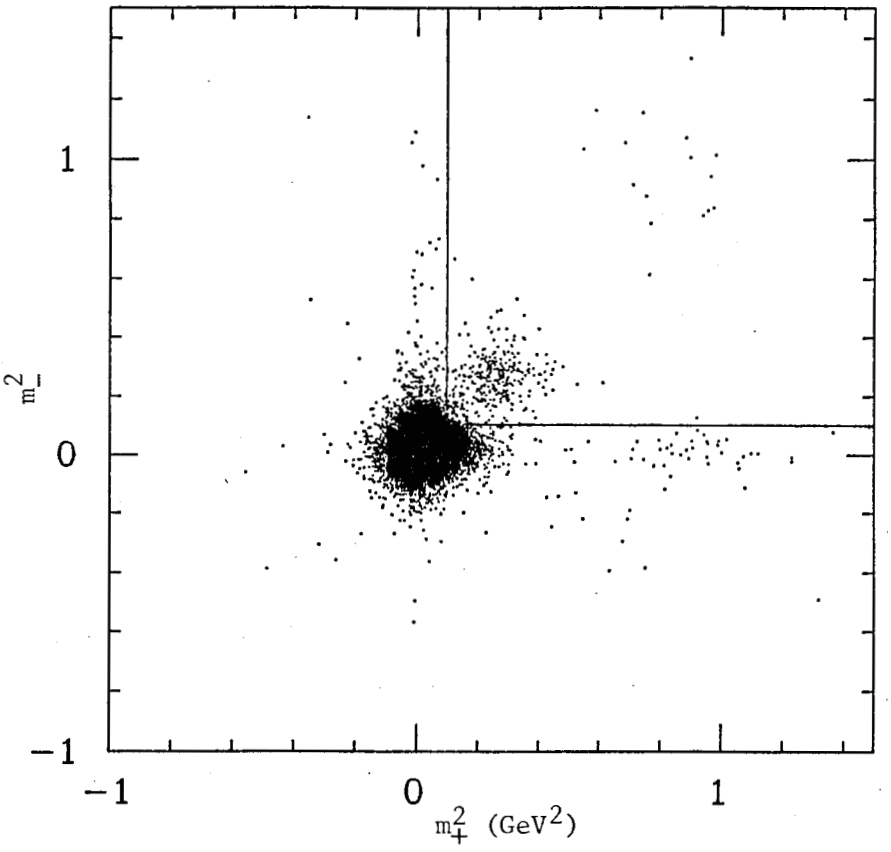

Figure 9.8. Scatter plot of time-of-flight m_+^2 *vs* m_-^2. The abscissae of each point is m^2 of the positive track, and the ordinate is m^2 of the corresponding negative track. The total number of entries is 37,536.

missed by the detector. It is not possible to separate them from $\pi^+\pi^-$ and $\mu^+\mu^-$ data, so their fraction is simply a guess based on what can be seen in Fig. 9.8.

The relative abundances of events types are

$$f_{\mu\mu} = 0.7000, \quad f_{\pi\pi} = 0.2895, \quad f_{\pi K} = 0.0005, \tag{9.14}$$
$$f_{KK} = 0.0080, \quad f_{p\overline{p}} = 0.0005, \text{ and } \quad f_{\pi p} = 0.0015\,.$$

Using these fractions, the weight for each event type is determined by multiplying the appropriate fraction by the product of the two single-particle weights. To normalize, the six weights are summed, and each weight is divided by that sum. Hence, the sum of all weights for a given event is unity.

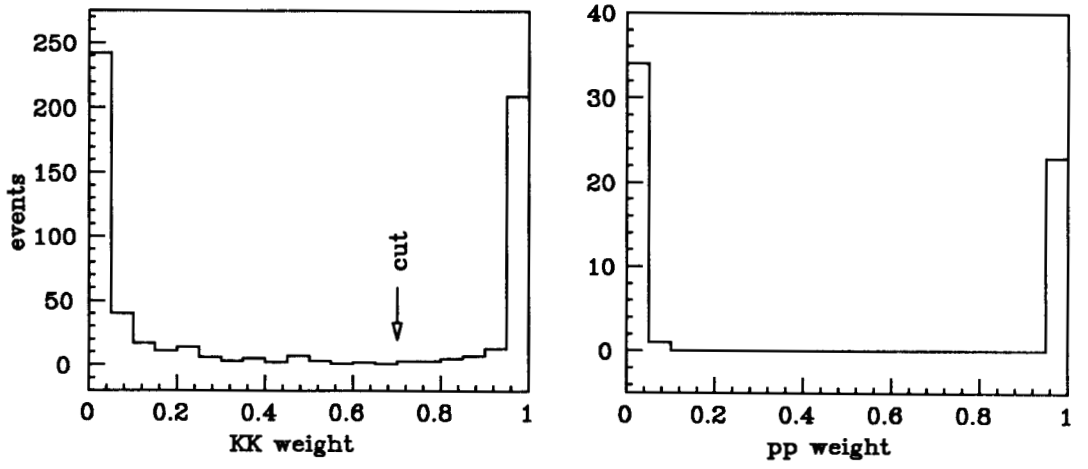

Figure 9.9. The $p\bar{p}$ and K^+K^- event weights for the time-of-flight analysis after the χ^2 have been made.

9.5 Selecting Kaon and Proton Pairs

The first cut imposed on time-of-flight residuals is to require that for both tracks $m_i^2 > 0.01\,\mathrm{GeV}^2$. It is shown by two intersecting lines on Fig. 9.8. Clearly it does not reject any kaon pairs which could be separated with confidence from the background. The second cut requires that each track have a χ_x^2, as calculated from Eqn. 9.9, less than 6.0 for kaons and 8.0 for protons. There are two degrees of freedom, so $\chi^2 = 6$ is the 95% level of the χ^2 distribution.

The final cuts are on the event weights. Figure 9.9 shows histograms of the event weights for kaon pairs and proton pairs for only those events in which both tracks pass the corresponding χ^2 cut. Keeping only those events with either a K^+K^- weight or a $p\bar{p}$ weight greater than 0.7 results in the final samples of 240 K^+K^- events and 23 $p\bar{p}$ events. A sum over events of the difference of the event weight from unity gives background estimates of five background events in the K^+K^- sample and none in the $p\bar{p}$ sample. Note that these background estimates include only contributions from time-of-flight misidentification and explicitly assume gaussian distributions for the errors.

9.6 Background Estimates

From the way that the event weights are defined, it is simple to estimate how much background is present from gaussian distributed fluctuations of the large pion-pair and muon-pair samples. The effect of non-gaussian tails, however, is more difficult to estimate. A rough idea can be had from looking at the size of the tail on the negative side of the time residual distribution. An easy way to do that is simply to repeat the analysis and look for particle pairs in which each has, assuming we are studying kaon pairs, a time-of-flight mass squared of $m^2 = -m_K^2 + m_\pi^2$. It is reasonable to translate by m_π^2 in this way because the expected time residual is approximately proportional to the square of the particle mass. The whole analysis based on χ^2 and event weights follows without change.

One finds that 81 events pass the "kaon-pair" χ^2 cut, but only 4 pass the cut on event weights. These numbers actually are consistent with gaussian tails, so we conclude that the background from time-of-flight misidentification in the kaon-pair sample is only the order of 5 to 10 events. The gaussian distributions predict zero background in the proton-pair sample, but 2 events pass the cuts when analyzed for negative m^2. Thus the corresponding background in the proton-pair sample is about 2 events.

Another potential source of background is from beam-gas collisions. Only 3 kaon-pair events with non-zero charge pass all of the cuts. Also, the distribution of the z-component of the event vertex is completely consistent with assuming all observed K^+K^- events to be from beam-beam collisions. For the proton pairs, there are 23 events consisting of two positively charged protons, but there are none with two antiprotons. The events of charge 2 have a vertex distribution which is consistent with being uniform in z, while the charge 0 events are clustered well within the beam-beam region. Since the probability for an incident electron to scatter two protons from a gas molecule is expected to be much greater than the probability for pair production of protons in such a collision, all evidence indicates that none of the observed $p\bar{p}$ events are produced from beam-gas

collisions. Additional background from beam-beam events in which some particles are not detected must be proportionally less than the corresponding background in the pion-pair sample and is completely negligible with respect to the statistical precision of the K^+K^- and $p\bar{p}$ samples.

9.7 Analysis of the K^+K^- Mass Spectrum

9.7.1 Data Reduction and Normalization

The K^+K^- data are analyzed in the region $1.3 \leq W_{KK} \leq 2.3\,\mathrm{GeV}$. Below the lower cut the trigger inefficiency is too severe to be adequately modeled. Except for the invariant-mass cut and the time-of-flight cuts which have been presented, all other cuts on the data are identical to those used in the pion-pair analysis.

Because of the dependence of the time-of-flight cuts on details of the detector geometry, and because of the greater importance of kaon decays compared with pion decays, all Monte Carlo results include the complete detector simulation. Simulation of the time-of-flight system has been discussed in Section 9.2. The decay products of kaons which have decayed in flight and of positive kaons which have decayed after ranging out in the detector material are included in full detail. The trigger is simulated in two ways. First, the dominant effect at low momentum is caused by electromagnetic range-out and is simulated during the detailed detector simulation by use of Eqn. 9.2. Second, the inefficiency due to nuclear interactions is assumed to be the same as for pions and is parameterized by Eqn. 6.1. While this surely is a crude approximation, the effect is not so important in the kaon-pair analysis because of relatively large statistical errors and because of greater importance of the simple electromagnetic energy loss. The error estimates on the efficiency are expanded by a factor of 1.5 relative to those for the pion pairs. Figure 9.10 shows a plot of the detection efficiency as calculated by the detector simulation for events generated within the cut $|\cos\theta_{\mathrm{lab}}| < 0.65$.

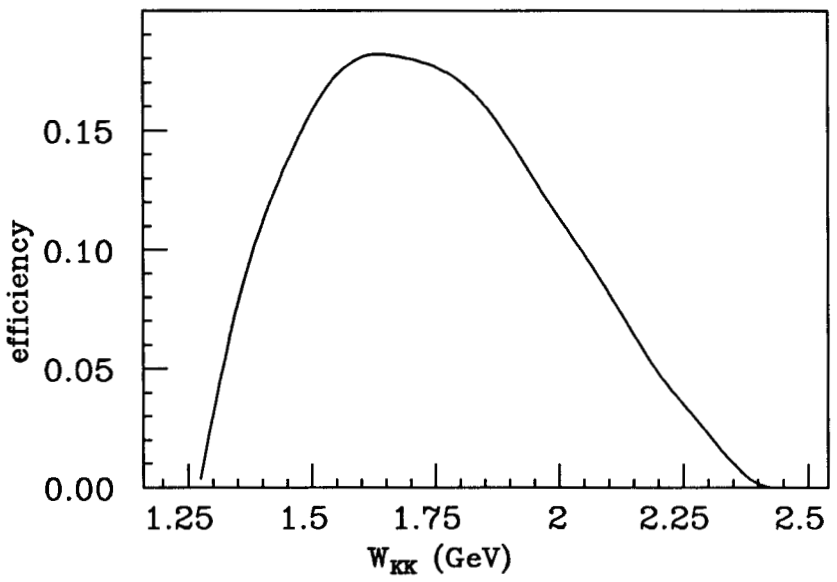

Figure 9.10. The detection efficiency for K^+K^- as calculated by Monte Carlo detector simulation assuming an angular distribution in the K^+K^- center-of-mass frame of $\sin^4\theta$.

The angular distribution assumed is appropriate for a tensor resonance produced with helicity two.

The normalization again is obtained from the electron-pair data. To avoid a relatively difficult analysis of electron pairs in data taken with the nitrogen Čerenkov radiator, small angle Bhabha scattering data from the luminosity monitors is used to extrapolate the effective luminosity measured from data taken with the isobutane radiator. Within a given data-taking season the luminosity monitors remain in the same position relative to the beam, so they are reliable when used to obtain the *ratio* of luminosities for two data samples taken within the same year.

The normalization from isobutane data is determined before making any cuts on the time-of-flight information, and it is measured within a fiducial cut requiring both tracks to pass at least one centimeter inside the edge of a barrel shower counter. Full detector simulation, including EGS for electromagnetic interactions in the beam pipe and drift chamber material and in the material preceding the

shower counter trigger, is made for Monte Carlo electron pairs in order to calculate the effective luminosity corresponding to the number of electron pairs observed in the isobutane data. Note that in this case the effective luminosity is close to the actual beam luminosity, since the detector simulation includes all known inefficiencies. The result from the *1983* isobutane data alone agrees with the result calculated in Section 4.10 for the same data but with different cuts. The total for the combined data set is

$$\mathcal{L} = 169.6 \pm 5.1\,\mathrm{pb}^{-1}, \qquad \text{(full data set)}. \tag{9.15}$$

In Fig. 9.11 is a histogram of the K^+K^- invariant mass from data. The spectrum in dominated by a peak centered about 1.525 GeV, which is identified as the f' resonance. But there also is a relatively large number of events below the f' peak, suggesting a significant background under the resonance. The overplotted histogram and smooth curve refer to the model which is presented and fit in the following two sections.

9.7.2 Model for $\gamma\gamma \to K^+K^-$

The model which is used to fit the data is a coherent sum of Breit-Wigner resonant amplitudes including all three tensor mesons. All resonances are assumed to be produced only with helicity two, as there are not enough data to consider seriously the angular distribution. The relative phases of the three resonances are taken to be real and positive, in accordance with $SU(3)$ quark model predictions.[69]

For the purpose of fitting the data, the cross section for $\gamma\gamma \to K^+K^-$ is written in this convenient form:

$$\begin{aligned}\frac{\mathrm{d}\sigma}{\mathrm{d}\Omega} =& \tfrac{1}{2}R_f^2 + \tfrac{1}{2}R_{A_2}^2 + \tfrac{1}{2}R_{f'}^2 + R_f R_{A_2}\cos(\delta_f - \delta_{A_2}) \\ &+ R_f R_{f'}\cos(\delta_f - \delta_{f'}) + R_{A_2} R_{f'}\cos(\delta_{A_2} - \delta_{f'})\,.\end{aligned} \tag{9.16}$$

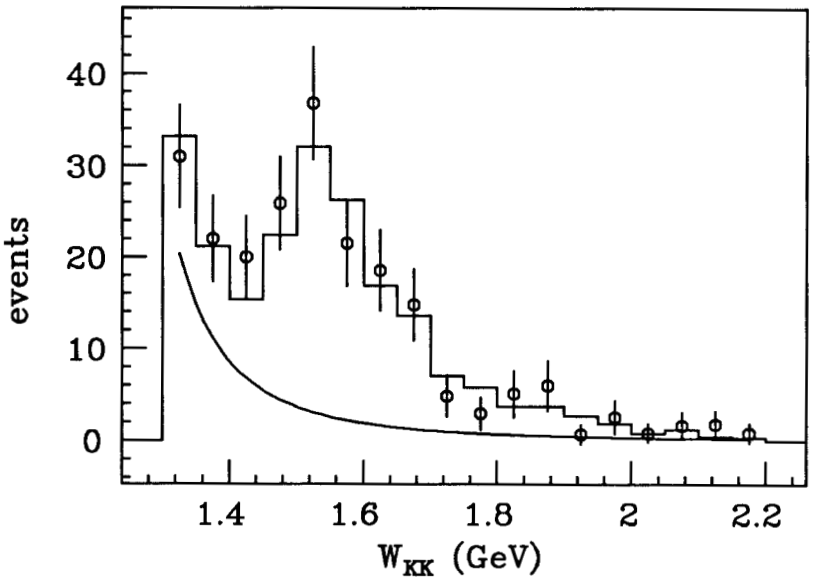

Figure 9.11. The measured K^+K^- invariant-mass spectrum. The points with error bars are data, while the overplotted histogram is the best fit of the model presented in Section 9.7.2. The smooth curve is an estimate of the continuum background, which is included in the histogram as well.

The phase shifts are given by $\tan\delta_r = m_r\Gamma(s)/(m_r^2 - s)$, and the resonance terms are

$$R_r = 5\sqrt{\tfrac{1}{2}}\, d^2_{20}(\theta)\frac{2}{\sqrt{s}}\frac{m_r\left[\Gamma_{\gamma\gamma}(s)\Gamma_{K\overline{K}}(s)\right]^{1/2}}{\left[(m_r^2 - s)^2 + m^2\Gamma_r(s)^2\right]^{1/2}}\,. \tag{9.17}$$

The factor of $\sqrt{1/2}$ comes from the fact that the isospin-zero amplitude is half K^+K^- and half $K^0\overline{K^0}$. The energy dependencies of the widths are parameterized as in Eqn. 7.32, except that m_π must be replaced by m_K for $\Gamma_r(s)$ and $\Gamma_{K\overline{K}}(s)$, and by $m_\gamma = 0$ for $\Gamma_{\gamma\gamma}(s)$. The properties assumed for the f and A_2 resonances are given in Table 1.1, except that the DELCO result, $\Gamma_{f\to\gamma\gamma} = 2.77 \pm 0.31\,\text{keV}$, is used. This is the result obtained when the coupling is assumed to be only in helicity two and the amplitudes are not unitarized. Questions of unitarity are not considered in the kaon-pair analysis, because the continuum production is not understood and, anyway, the statistical precision is not sufficient that it matters.

In addition to the f, A_2, and f' there is another $J^P = 2^+$ meson called the $\theta\,(1690)$ in the relevant mass range which has been observed to decay to $K\overline{K}$.

However, neither its branching ratio to $K\overline{K}$ nor to $\gamma\gamma$ are known. Furthermore, it is in a region which still is dominated by the other three tensor mesons. Certainly one can see no evidence of it in the DELCO data. We do not attempt to set a hard limit on the product of branching ratios, because any such result would be highly model dependent due to interference with the long tails of the other resonances. In Ref. 5 one finds the upper limit $\mathrm{BR}(\theta \to K^+K^-) \cdot \Gamma_{\theta\to\gamma\gamma} < 0.08\,\mathrm{keV}$.

Figure 9.12 shows a plot of the resulting cross section with the two-photon luminosity function folded in. The spectrum is integrated numerically over the angular range $-0.6 \leq \cos\theta \leq 0.6$ and assumes a cut on total transverse momentum of $k_\perp/W_{\gamma\gamma} \leq 0.2$. Compared with that is a plot of the result with the f and A_2 resonances not included. One can see that the interference has a large effect on the predicted f' peak. That raises the issue of how dependent is the spectrum in the f' region on the parameterization of the energy-dependent widths of the f and A_2. In fact, if the widths are given no energy dependence at all, then the cross section in the f' region and above is decreased by 25% or more. However, when the parameter a in Eqn. 7.32 is changed from zero to infinity, the change in the spectrum is negligible with respect to the statistical errors of the data. Thus the results are not too sensitive to the *details* of the parameterization of the resonance shape, but it is essential to assume some reasonable parameterization.

Some amount of continuum production must also be expected, but there exists no reliable prediction for it in the energy range accessible to DELCO. The Born term gives a prediction which is much too large to fit the data, as one can see by comparing Fig. 9.11 with Fig. 9.12. There are three reasons why that would be expected. First, the assumption of point coupling generally is worse for kaons than for pions. Second, the KK phase shifts are known to be large even near threshold, so Watson's theorem (Eqn. 7.43) would require substantial modifications of the Born term. Third, inelastic effects are more important than for $f \to \pi^+\pi^-$, so even Watson's theorem is not useful. Furthermore, the energy is too low to rely on QCD predictions. Therefore, we follow the procedure of Ref. 7 and introduce

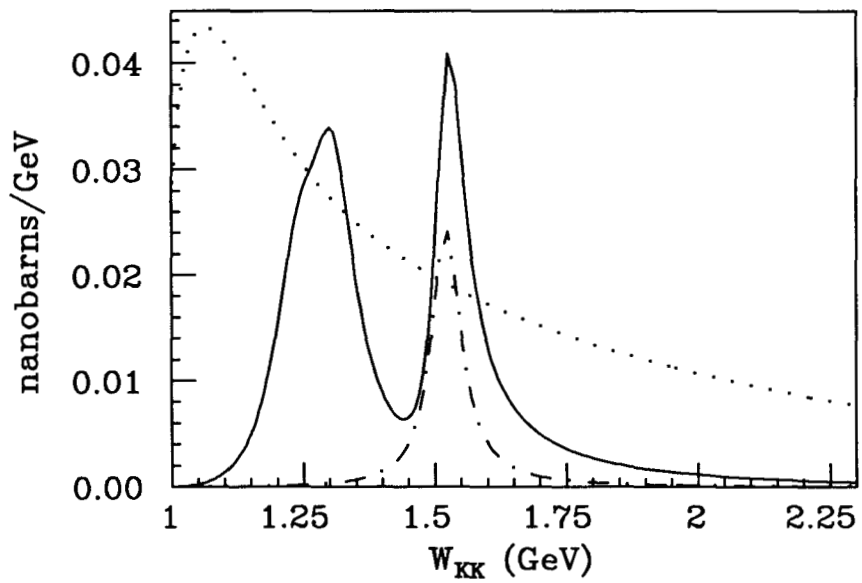

Figure 9.12. Predictions for the K^+K^+ mass spectra. The solid curve is a coherent sum of the three tensor meson resonances. The dot-dash curve shows the f' contribution alone. The two-photon widths are assumed to be as given in Eqn. 1.1. The dotted curve is the cross section for K^+K^- production as given by the Born term (Eqn. 7.27 with m_π replaced by m_K).

arbitrary functions of W_{KK} to describe the background for the purpose of fitting the two-photon width of the f'. The functions used are of the forms

$$B_1(W) = A \cdot \exp\left(-\frac{(W-\overline{W})^2}{2\sigma^2}\right), \qquad \overline{W} < 1.1\,\text{GeV}, \tag{9.18}$$

and

$$B_2(W) = A \cdot [W - W_0]^{-n}, \quad 1 \leq n \leq 10. \tag{9.19}$$

The parameters A, W_0, and σ are allowed to vary freely, and several fixed values are tried for n and $\overline{W}$. Both forms give good fits to the data, whereas the resonance terms alone fail to describe the spectrum below the f' peak. Also, both forms have a reasonable shape in the resonance region, since one generally expects the continuum spectrum to be continuously decreasing with increasing energy. Note that QCD predicts that at sufficiently high energy the spectrum should fall

as $1/W^7$ when convoluted with the EPA spectrum, while the Born prediction decreases as $1/W^3$. Probably, the truth in the f' energy range is somewhere between those two extremes.

Events generated by this model are processed through detector simulation and the full analysis procedure. Because of the limited statistical precision of the data, it is not necessary to vary the resonance masses and full widths in the fit. It is important to be able to vary the two-photon widths of all three resonances. That is simple to do with the cross section expressed as it is in Eqn. 9.16. One simply retains throughout the analysis the fraction of the total event weight contributed by each of the six terms. Each term is proportional either to one $\gamma\gamma$ width or else to the square root of the product of two $\gamma\gamma$ widths, so the fitting program can vary all three $\gamma\gamma$ widths independently by appropriately varying the contributions of the six terms to the sum.

9.7.3 Fitting the Invariant-Mass Spectrum

There are a total of nine parameters which may be varied within a single run of the fitting program:

1. $\mathrm{BR}(f' \to K\overline{K}) \cdot \Gamma_{f'\to\gamma\gamma}$
2. $\mathrm{BR}(A_2 \to K\overline{K}) \cdot \Gamma_{A_2\to\gamma\gamma}$ $= 0.040 \pm 0.013\,\mathrm{keV}$
3. $\mathrm{BR}(f \to K\overline{K}) \cdot \Gamma_{f\to\gamma\gamma}$ $= 0.080 \pm 0.011\,\mathrm{keV}$
4. Luminosity. $\mathcal{L} = 169.6 \pm 5.1\,\mathrm{pb}^{-1}$
5. Norm. of ToF background. $N_{\mathrm{tof}} = 1.0 \pm 1.0$
6. Efficiency error at $W = 1.3\,\mathrm{GeV}$. $\varepsilon_1 = 0 \pm 0.14$
7. Efficiency error at $W = 2.3\,\mathrm{GeV}$. $\varepsilon_2 = 0 \pm 0.10$
8. Background parameter #1.
9. Background parameter #2.

Parameter number 5 refers to the background estimate which follows from the gaussian event weights. That background is only a few events total and is confined mostly to the invariant mass range above the f' region. This parameter allows

the normalization of that background to vary within reasonable limits and is not important. Parameters 6 and 7 account for the uncertainty in the trigger efficiency, which is assumed to vary linearly between the values, ε_1 and ε_2, specified at the upper and lower limits of the invariant mass range. The last two parameters are those of the background parameterizations specified in equations 9.18 and 9.19.

As a specific example, consider a fit in which the background parameterization of Eqn. 9.19 with $n = 3$ is assumed and all nine parameters are allowed to vary within the specified limits. Table 9.1 shows the explicit results of the fit, and Fig. 9.11 shows a comparison of the result with the data. A large part of the contribution to χ^2 comes from the single low bin at $W = 1.925\,\mathrm{GeV}$. When only the first 10 bins are included in the fit, then $\chi^2 = 9.8$, and the fitted f' two-photon width decreases by 0.003 keV.

Such a fit as is shown in Table 9.1 assumes gaussian distributions for those parameters which are constrained within known error limits. The resulting overall error estimate for the f' two-photon width corresponds to addition of the various error contributions in quadrature. Let us consider the contributions to the error individually. When only the f' two-photon width and the background parameterization (with $n = 3$) are allowed to vary, then the best fit for the two-photon width does not change, but the error estimate becomes only $\pm 0.017\,\mathrm{keV}$. Fixing the background as well yields an estimate of the *statistical error* of $\pm 0.015\,\mathrm{keV}$. Contributions to the error from the other parameters are determined by fixing them one by one at their upper and lower limits and then fitting the spectrum by varying all remaining parameters. Table 9.2 lists the individual contributions. That from the background parameterization takes into consideration the varying results obtained from using Eqn. 9.18 as well as Eqn. 9.19 and also the effects of changing the exponent n between 1 and 10 and the mean of the gaussian between 0.1 GeV and 1.1 GeV. Hence the error is larger than in Table 9.1, where n is held fixed at $n = 3$. With all things considered, the final

Table 9.1. A fit of the model for $\gamma\gamma \to K^+K^-$ to time-of-flight identified data. The parameterization of the background is given by Eqn. 9.19 with $n = 3$.

Parameter	Fit Value		Lower Error	Upper Error
1. $\mathrm{BR}(f' \to K\overline{K}) \cdot \Gamma_{f'\to\gamma\gamma}$	0.070	keV	-0.021	+0.025
2. $\mathrm{BR}(A_2 \to K\overline{K}) \cdot \Gamma_{A_2\to\gamma\gamma}$	0.039	keV	-0.013	+0.013
3. $\mathrm{BR}(f \to K\overline{K}) \cdot \Gamma_{f\to\gamma\gamma}$	0.080	keV	-0.011	+0.011
4. luminosity	169.5	pb^{-1}	-5.1	+5.1
5. ToF background	1.4		-1.0	+1.0
6. ε_1	-0.03		-0.14	+0.14
6. ε_2	-0.03		-0.10	+0.10
8. A (Eqn. 9.19)	0.31		-0.22	+0.49
9. W_0 (Eqn. 9.19)	1.09		-0.10	+0.08

Covariance Matrix Correlation Coefficients

	1	2	3	4	5	6	7	8
2	-0.201							
3	-0.102	0.024						
4	-0.140	0.017	-0.048					
5	-0.012	-0.013	-0.006	-0.013				
6	-0.531	-0.004	0.034	0.030	0.004			
7	-0.155	-0.013	-0.079	0.005	-0.019	0.053		
8	-0.280	-0.234	-0.131	-0.054	-0.080	-0.132	-0.065	
9	0.330	0.139	0.090	0.035	0.080	0.057	0.062	-0.972

Fit range: $1.3 < W < 2.0\,\mathrm{GeV}$ 14 bins
χ^2=18.1

result for the f' is obtained by adding the systematic errors in quadrature:

$$\Gamma_{f'\to\gamma\gamma} \cdot \mathrm{BR}(f' \to K\overline{K}) = 0.07 \pm 0.04\,\mathrm{keV}. \tag{9.20}$$

Unfortunately, the branching ratio of the f' to $K\overline{K}$ is not yet known to sufficient accuracy to quote a measurement of the two-photon width alone.

Table 9.2– Contributions to the error on $\mathrm{BR}(f' \to K\overline{K}) \cdot \Gamma_{f'\to\gamma\gamma}$ from the fit to the K^+K^- invariant-mass spectrum.

Source of Error	Error in keV
size of K^+K^- sample	$\pm$ 0.015 (stat.)
luminosity measurement	$\pm$ 0.002 (syst.)
detection efficiency	$\pm$ 0.015 (syst.)
$\mathrm{BR}(f \to K\overline{K}) \cdot \Gamma_{f\to\gamma\gamma}$ and $\mathrm{BR}(A_2 \to K\overline{K}) \cdot \Gamma_{A_2\to\gamma\gamma}$	$\pm$ 0.015 (syst.)
background parameterization	$\pm$ 0.027 (syst.)

9.8 Measurement of $\gamma\gamma \to p\overline{p}$

Not enough proton pairs have been detected to allow any analysis of the shapes of kinematic distributions. Therefore, we consider only a measurement of the average cross section for $\gamma\gamma \to p\overline{p}$ over the range in which data are available ($2.2 < W < 2.9\,\mathrm{GeV}$).

There is no large sample of protons in any data set which may be used to measure the detector response for protons, so the Monte Carlo detector simulation must be relied upon to calculate the detection efficiency for $p\overline{p}$. The dominant systematic effect again comes from the barrel shower counter latch efficiency. The contribution from electromagnetic range-out is calculated the same as for

the K^+K^- analysis, using Eqn. 9.2. For protons, the resulting momentum cutoff is predicted to be at about 0.6 GeV. Above that momentum, some inefficiency is caused by nuclear interactions. An HETC calculation predicts that the shower counter latch efficiency for protons incident on a counter is 92% at $p = 0.7$ GeV and rises slowly to 98% at $p = 2.0$ GeV. The HETC program does not handle antiprotons, so the same efficiency is assumed for them. Thus the loss of events from nuclear interactions is estimated to be about 15% overall. The error in this result can only be guessed, but even a very conservative estimate gives an error bar no larger than the statistical error.

To measure the detection efficiency, Monte Carlo events of the type $e^+e^- \to e^+e^-p\bar{p}$ are generated using the EPA luminosity function and a unit cross section for $\sigma_{\gamma\gamma\to p\bar{p}}$. Thus the Monte Carlo assumes a uniform angular distribution. The detector is simulated for the generated events, and the full analysis procedure is applied, just as for data. One finds that the predicted detection efficiency rises sharply from zero at $W = 2.2$ GeV and peaks at about 2.7 GeV, falling slowly above that point. The maximum efficiency is about 5%.

The luminosity of the data is $170\,\mathrm{pb}^{-1}$, and 23 $p\bar{p}$ events are found within the range $2.2 < W < 2.9$ GeV. Assuming a uniform angular distribution to calculate the detection efficiency, this corresponds to a cross section for $\gamma\gamma \to p\bar{p}$, integrated over the acceptance $|\cos\theta_{\mathrm{cms}}| < 0.6$, of 1.01 ± 0.21 nb. The observed angular distribution may be taken into account by calculating with Monte Carlo the detection efficiency as a function of both W and $\cos\theta_{\mathrm{cms}}$. When such a calculation is used to correct the data event by event, then the result is a cross section of 1.25 ± 0.32 nb. The errors quoted are statistical only. Including a 20% uncertainty in the detection efficiency and accounting for the dependence on the assumed angular distribution, we arrive at the result

$$\sigma_{\gamma\gamma\to p\bar{p}} = 1.2 \pm 0.5\,\mathrm{nb} \qquad |\cos\theta_{\mathrm{cms}}| < 0.6\,, \tag{9.21}$$

averaged over the region $2.2 < W < 2.9$ GeV.

10. Conclusions

10.1 The QED Channel

Kinematic distributions from a sample of over 45,000 events from the process $e^+e^- \to e^+e^-e^+e^-$ have been compared with leading-order QED predictions. The shapes of the distributions for untagged ($Q^2 \approx 0$) data are in complete agreement with leading-order (α^4) QED predictions within statistical error limits which range over the histogram bins from 1% at $W_{\text{min.}} = 0.6\,\text{GeV}$ to 10% at $W_{\text{max.}} = 2.6\,\text{GeV}$. Figures 4.14 and 4.16 show comparisons between data and QED predictions for the invariant mass and angular distributions of the detected electron pair. The shapes of distributions from tagged data ($\overline{Q^2} = 0.4\,\text{GeV}^2$) agree as well, with statistical errors ranging from 4% to 22%. Figures 4.19 and 4.20 show those results. Other experiments also have published results on this reaction channel, but only with far less statistical precision and only for relatively large[70] ($W > 1\,\text{GeV}$) or small[71] ($W < 0.5\,\text{GeV}$) invariant masses.

Absolute normalization of the measured cross sections has been obtained from the beam luminosity as measured from another QED process, $e^+e^- \to \mu^+\mu^-$, but only within systematic errors of 7 to 10 percent. At that level the cross sections agree with QED predictions. The measurement of the four-electron final state is itself used to determine the normalization of the $e^+e^-\mu^+\mu^-$ channel and the two-photon hadronic channels to an accuracy of better than 3%.

10.2 Cross Section for $\gamma\gamma \to \pi^+\pi^-$

10.2.1 Measurements from Untagged Data ($Q^2 \approx 0$)

The cross section for $\gamma\gamma \to \pi^+\pi^-$ has been measured at $Q^2 \approx 0$ from a sample of 21,000 pion pairs plus 50,000 muon pairs within the laboratory acceptance $0.6 < W < 2.0\,\text{GeV}$, $|\cos\theta| < 0.6$. DELCO has an advantage over previous measurements due to the fact that electron pairs need not be subtracted from the data and that the normalization for subtraction of muons pairs can be

obtained with an accuracy of 2.3% from a measurement of the four-electron final state.† The normalization of the pion-pair cross section is normalized to the same QED measurement, but uncertainty in the detection efficiency, due to nuclear interactions, contributes systematic errors of 5 to 10 percent.

Figure 10.1 shows the differential cross section measured for the invariant mass of the pion pair, with all known detector effects, including the momentum resolution, corrected for by the procedure detailed in Appendix C. The prominent peak is due to production of the $f(1270)$ resonance. Figure 10.2 shows the measured angular distribution of the pions in their center-of-mass system. It has been corrected for detector effects, of which the most important by far is the loss of acceptance caused by the boost of the $\gamma\gamma$ system in the laboratory frame of reference. The data are compared with predictions for helicity-two and helicity-zero coupling of $\gamma\gamma$ to the f resonance. It is clear that the helicity-two assumption is preferred. A detailed simultaneous fit to both distributions, assuming that the continuum is described by the simple Born term prediction, gives a limit on the ratio of the helicity-zero to helicity-two $\gamma\gamma$ coupling (see Eqn. 8.11):

$$\frac{\Gamma^{\lambda=0}_{f\to\gamma\gamma}}{\Gamma^{\lambda=2}_{f\to\gamma\gamma}} < 0.14 \qquad \text{(90\% confidence)}. \tag{10.1}$$

This is consistent with theoretical expectations and may be compared with the best previously published limit of 0.12 ± 0.39.[9] The latter result was obtained from $\gamma\gamma \to \pi^0\pi^0$ and is somewhat less model dependent, because of the lack of a significant continuum contribution to the neutral channel.

In Chapter 2 we have seen how the cross section for $e^+e^- \to e^+e^-\pi^+\pi^-$ may be decomposed for untagged events into a luminosity function for quasi-real photon pairs times the cross section $\sigma_{\gamma\gamma\to\pi^+\pi^-}$. By using the equivalent-photon approximation (EPA), the luminosity function is easily calculated as a function of $W_{\gamma\gamma}$. Therefore, one can determine $\sigma_{\gamma\gamma\to\pi^+\pi^-}$ from the data of

† The recent results of the *PEP-4/PEP-9* experiment[5] have roughly the same advantages.

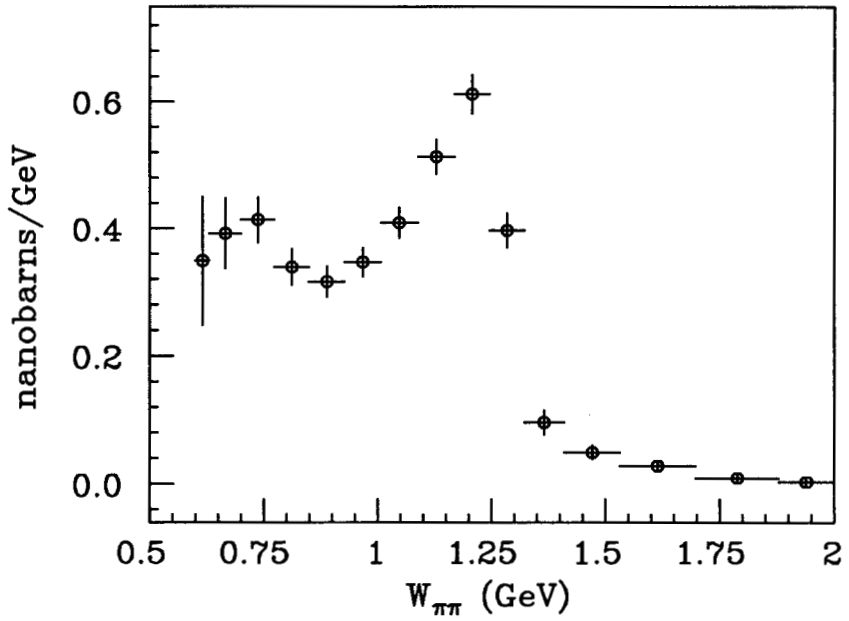

Figure 10.1. The measured differential cross section for the invariant mass of pion pairs from $e^+e^- \rightarrow e^+e^-\pi^+\pi^-$. The data have been corrected for all known detector effects within the acceptance defined by $|\cos\theta_{\rm lab}| < 0.6$, $k_\perp/W < 0.2$, and $k_\perp < 0.3\,{\rm GeV}$.

Fig. 10.1. First, the data are corrected for the loss of acceptance due to the boost of the $\gamma\gamma$ system in the $\pm z$ direction. That is done by using the EPA Monte Carlo to predict the distribution of the boost and then calculating the inefficiency from the cut $|\cos\theta_{\rm lab}| < 0.6$. The angular distribution of the resonance decay is assumed to be $\sin^4\theta$, as is appropriate for helicity-two production. Then the result is divided by the calculated luminosity function. Figure 10.3 shows the result. It is not extrapolated to an acceptance of 4π steradians, so when comparing with a theoretical model, the cross section must be integrated over the range $-0.6 < \cos\theta_{\rm cms} < 0.6$. Note that there is a small amount of model dependence in the result, because in order to correct for the effects of the detector acceptance, some assumption must be made about the angular distribution. It is assumed to be given by a coherent sum of the Born term and the f resonance in helicity two, which has been shown to give an excellent fit to the observed angular distribution. The angular distribution cannot be observed by DELCO outside of

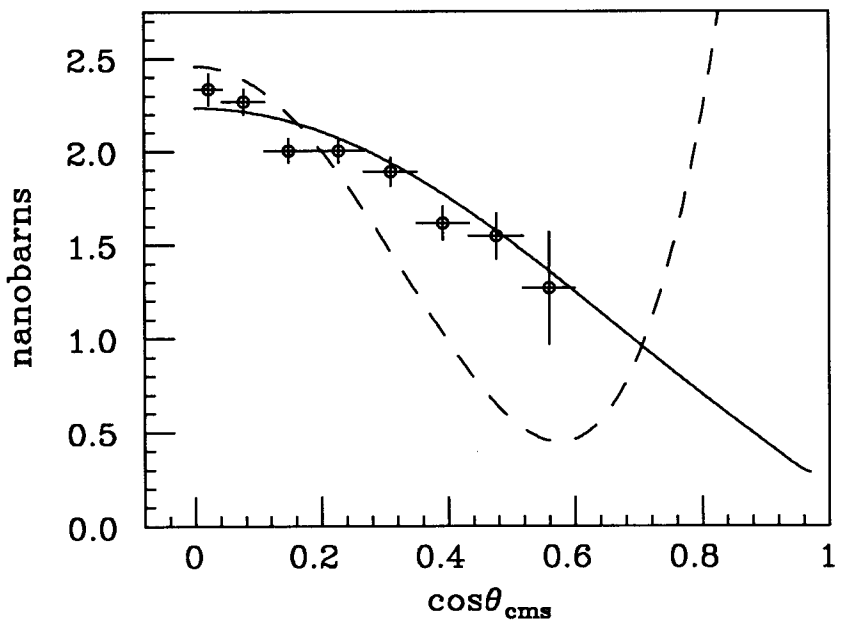

Figure 10.2. The measured differential cross section for $\cos\theta_{\rm cms}$ of pion pairs from $e^+e^- \to e^+e^-\pi^+\pi^-$. The smooth curves show predictions for helicity-two (solid curve) and helicity-zero (dashed curve) coupling of $\gamma\gamma$ to the f resonance. The data have been corrected for all known detector effects within the acceptance defined by $1.0 < W < 1.5\,\mathrm{GeV}$, $k_\perp/W < 0.2$, and $k_\perp < 0.3\,\mathrm{GeV}$.

$|\cos\theta| < 0.6$, so to extrapolate to the full solid angle would be even more model dependent.

The smooth curve shown in Fig. 10.3*a* represents a calculation of the unitarized Lyth model (Eqn. 8.1) for $\sigma_{\gamma\gamma\to\pi^+\pi^-}$, integrated over the range $-0.6 < \cos\theta_{\rm cms} < 0.6$ with $\Gamma^{\lambda=0}_{f\to\gamma\gamma} = 0$ and $\Gamma_{f\to\gamma\gamma} = 3.34\,\mathrm{keV}$ (from Eqn. 8.8). There appears to be substantial disagreement both below and above the f peak. However, systematic errors are not shown in Fig. 10.3. The uncertainty in the beam luminosity and in the $\pi^+\pi^-$ trigger efficiency is larger than the disagreement below the f peak. Also, there is some uncertainty in the energy scale of the experiment, and the agreement is better if the f mass is shifted downward by about 1%. The disagreement just above the f peak is not understood. Figures 8.1 and 8.2 show how well the measured spectra agree with the model prediction

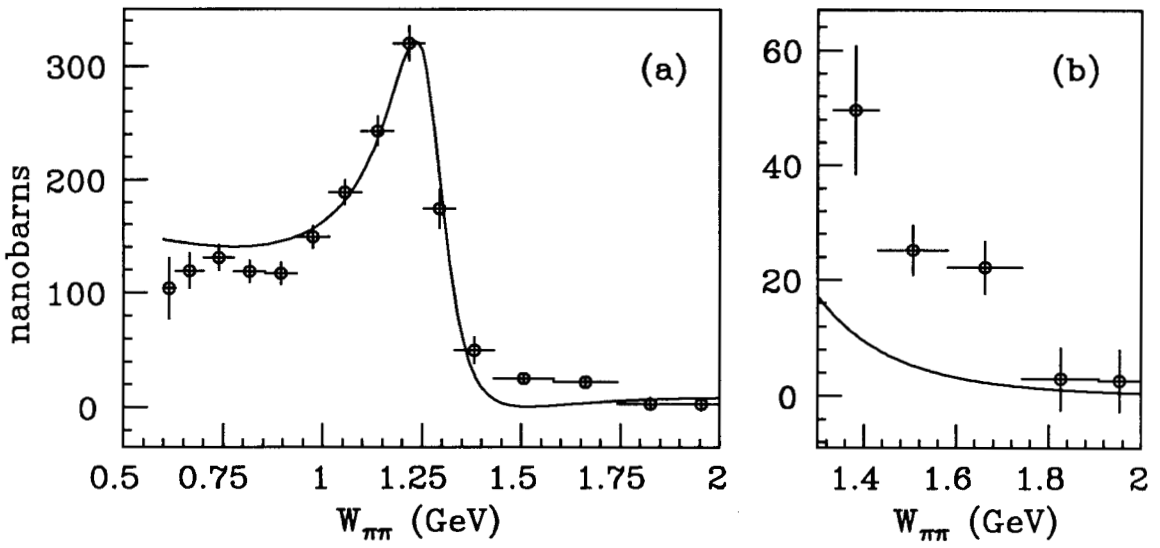

Figure 10.3. The cross section for $\gamma\gamma \to \pi^+\pi^-$ measured from untagged data for $-0.6 < \cos\theta_{\rm cms} < 0.6$. The error bars include only statistical errors. The smooth curve in (*a*) is the theoretical prediction of Eqn. 8.1 assuming purely helicity-two coupling to the resonance. The smooth curve in (*b*) is the QCD prediction for continuum production given by Eqn. 7.2.

when systematic errors are taken into account. For reference, in Fig. 10.3*b* the QCD prediction of Eqn. 7.2 is compared with the data points between 1.4 GeV and 2.0 GeV.

The two-photon width of the f has been determined from the data by fitting the observed mass spectrum with the theoretical model. With systematic errors accounted for, good fits are obtained up to $W = 1.4$ GeV. There is significant disagreement above that point, but it has been found to contribute only a minor amount of uncertainty to the measured two-photon width. Results have been presented in Chapter 8 for several different theoretical assumptions about the angular distribution and unitarity constraints. In order to compare with previous measurements, first the results are presented under theoretical assumptions common to most of the measurements. Most experiments have assumed a simple model of a coherent sum of the Born term (Eqn. 7.27) and a Breit-Wigner amplitude (Eqn. 7.34) with no corrections made to satisfy unitarity

constraints. The coupling of $\gamma\gamma$ to the f is assumed to occur only in the helicity-two amplitude. With those assumptions, the DELCO result is, after extrapolating to $Q^2 = 0$ by the GVDM form factor (see Eqn. 8.7 and Section 8.3.5),

$$\Gamma_{\gamma\gamma} = 2.81 \pm 0.31\,\text{keV}, \quad (\lambda = 2, \text{ no unitarization}). \tag{10.2}$$

This is compared in Table 10.1 with previously published measurements. All of the measurements quoted assume that the coupling is exclusively helicity-two. The CELLO result assumes the Mennessier model (see Section 7.5), which satisfies unitarity constraints which are essentially elastic except for a small $K\overline{K}$ contribution. However, as stated by the CELLO collaboration in Ref. 61, the unitarity constraint has negligible effect. None of Mennessier's options for vector meson exchanges and scalar resonances are used in the CELLO analysis, so their model is not significantly different from the simple Born term plus Breit-Wigner. The Mark II and *PEP-4/PEP-9* results allow the normalization of the term describing the interference of the resonance and continuum to float free in the fit, and the Mark II analysis of *PEP* data assumes that the continuum is described by a QCD prediction (see Eqn. 7.2) above $W = 1\,\text{GeV}$. However, these differing assumptions do not affect the results for the two-photon width significantly with respect to the stated error limits. The Crystal Ball result is unique in that it is from a measurement of $e^+e^- \to e^+e^-\pi^0\pi^0$, instead of the usual charged pion channel. The neutral channel has negligible continuum background, so the Crystal Ball result should be relatively model independent.

When corrections are made to the simple model of the Born term plus a Breit-Wigner amplitude in order to satisfy elastic unitarity constraints according to the prescription by Lyth (see Section 7.4.6), we find that the fitted two-photon width increases by 20% over the value quoted in Eqn. 10.2 (see Eqn. 8.8). When, in addition, the contribution from helicity-zero coupling is allowed to be free in the fit and both the invariant mass and angular distributions are fit simultaneously,

Table 10.1– Summary of published measurements of $\Gamma_{f\to\gamma\gamma}$ in chronological order. All measurements assume helicity-two coupling. The DELCO result is without unitarity corrections. For each measurement quoted, the first error is statistical and the second is systematic.

Collaboration	Reference	$\Gamma_{f\to\gamma\gamma}$ [keV]	Final State
PLUTO, 1982 analysis	72	2.3 ±0.5 ±0.3	$\pi^+\pi^-$
TASSO	73	3.2 ±0.2 ±0.7	$\pi^+\pi^-$
Mark II, *SPEAR* data	41	3.6 ±0.3 ±0.5	$\pi^+\pi^-$
Crystal Ball	9	2.7 ±0.2 ±0.6	$\pi^0\pi^0$
Mark II, *PEP* data	3	2.52±0.13±0.38	$\pi^+\pi^-$
CELLO	61	2.5 ±0.1 ±0.5	$\pi^+\pi^-$
PLUTO, 1984 analysis	74	3.25±0.25±0.50	$\pi^+\pi^-$
PEP-4/PEP-9	5	3.2 ±0.1 ±0.4	$\pi^+\pi^-$
DELCO, this thesis		2.81±0.07±0.30	$\pi^+\pi^-$

then the result is (from Eqn. 8.11, but extrapolated to $Q^2 = 0$)

$$\Gamma_{f\to\gamma\gamma} = \Gamma^0_{\gamma\gamma} + \Gamma^2_{\gamma\gamma} = 3.47 \pm 0.37\,\text{keV}. \tag{10.3}$$

The statistical contribution to the error is only $\pm 0.07\,\text{keV}$ and is included in quadrature with the systematic error. The systematic error includes contributions from the uncertainty in the ratio of helicity amplitudes and in the degree to which elastic unitarity should be satisfied (see Section 7.4.7), but it is dominated by the uncertainty in the pion-pair trigger efficiency. The result in Eqn. 10.3 is best compared with the Crystal Ball result with no constraint on the ratio of helicity amplitudes.[9] Their result of $\Gamma_{\gamma\gamma} = 2.9^{+0.6}_{-0.4} \pm 0.6\,\text{keV}$ is in agreement with DELCO. However, it is unfortunate that the error estimates are so large, because this result gives no information on the consistency of the unitarization procedure applied to the model for charged pion-pair production (see Section 7.6). When unitarization corrections are not made, the result for $\Gamma_{\gamma\gamma}$ is lower than that presented in Eqn. 8.11 by a factor of 0.83.

10.2.2 *Measurements from Tagged Data* ($\overline{Q^2} = 0.44\,\mathrm{GeV}^2$)

The tagged data have been analyzed according to the same theoretical model as used for untagged data, except that the prediction for the continuum is multiplied by a GVDM form factor $F(Q^2)$ according to Eqn. 2.20. The Q^2 dependence of the single-tag luminosity function is given by Eqn. 2.18, and the range of Q^2 is limited by the geometric extent of the DELCO luminosity counters. The average over the acceptance is $\overline{Q^2} = 0.44\,\mathrm{GeV}^2$. This model is found to give an excellent fit to the data within statistical error limits.

For tagged events, the incoming two-photon state consists of all three possible helicity states, and the theoretical expectations for $\sigma_{\gamma\gamma\to\pi\pi}(Q^2)$ are that the helicity-zero and helicity-one contributions increase rapidly with Q^2. The measured angular distribution of pion pairs constrains the helicity-one contribution to less than 15% of the two-photon width but allows the helicity-zero contribution to be as large as or larger than the helicity-two contribution. In Section 8.4 one may find the results of fitting the two-photon width under two different assumptions about the angular distribution. In order to account fully for the uncertainty in the angular distribution, it is best to use the result with the ratio of helicity amplitudes left free in the fit:

$$\Gamma_{\gamma\gamma}(\overline{Q^2} = 0.44\,\mathrm{GeV}^2) = 1.42 \pm 0.33\,\mathrm{keV}, \qquad \text{(no unitarization)}. \tag{10.4}$$

The result with the ratios of helicity amplitudes constrained to certain theoretical expectations (see Eqn. 8.14) is consistent with Eqn. 10.4, but the error bar is, of course, much smaller. Figure 10.4 shows a comparison of the tagged measurement with the untagged measurement. Both values assume the theoretical model *without* unitarity corrections. The decrease in cross section with Q^2 is consistent with the prediction of the GVDM form factor.

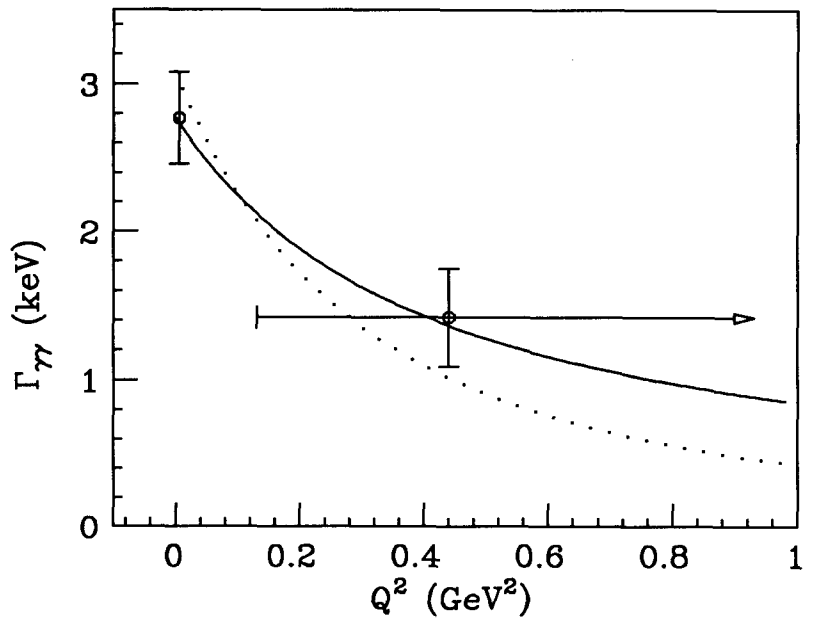

Figure 10.4. The measured Q^2 dependence of $\Gamma_{f\to\gamma\gamma}$ compared with the GVDM form factor (solid curve). The horizontal error bar indicates the large range of Q^2 over which the tagged measurement is made. The point are placed at the average value of Q^2 predicted by the appropriate $\gamma\gamma$ luminosity function. The dotted curve shows for comparison a simple ρ-pole form factor.

10.3 Measurement of the f' Two-Photon Width

A sample of 240 events from the process $e^+e^- \to e^+e^-K^+K^-$ have been identified by time-of-flight measurements in the kaon-pair mass range from 1.3 GeV to 2.3 GeV. The mass spectrum may be found in Fig. 9.11. One can see clear evidence for production of the f' resonance. There also is a relatively high cross section below the f' peak. The spectrum has been fit to a coherent sum of three interfering tensor resonances, but it still is necessary to assume a significant amount of continuum production. Lacking a reliable theoretical description of the continuum production, the simple parameterizations given by equations 9.18 and 9.19 are assumed. The branching ratio of the f' to $K\overline{K}$ is not known, so the result is expressed as (from Eqn. 9.20)

$$\Gamma_{f'\to\gamma\gamma} \cdot \mathrm{BR}(f' \to K\overline{K}) = 0.07 \pm 0.04\,\mathrm{keV}. \tag{10.5}$$

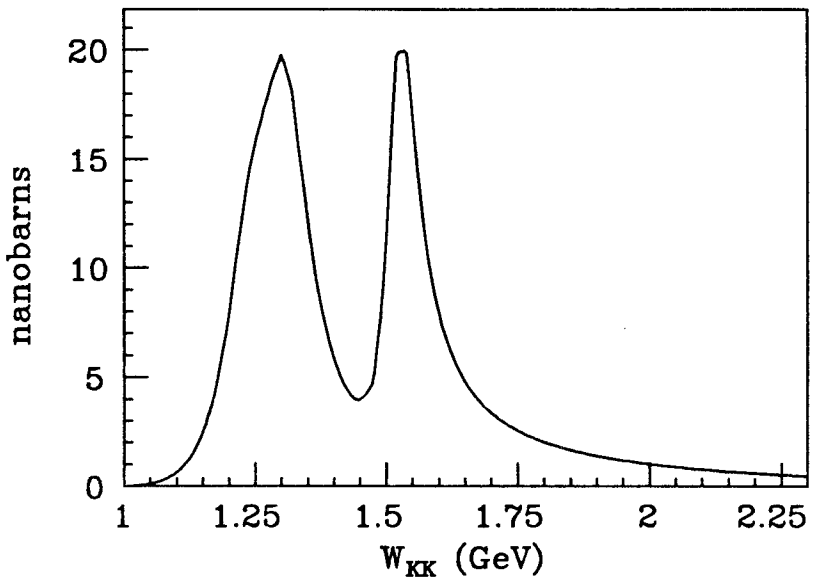

Figure 10.5. Predictions for the resonant contribution to $\sigma_{\gamma\gamma\to K^+K^-}$ integrated over the center-of-mass acceptance defined by $-0.6 < \cos\theta < 0.6$. The values used for $\Gamma_{f\to\gamma\gamma}$ and $\Gamma_{f'\to\gamma\gamma}$ are the DELCO measurements, while $\Gamma_{A_2\to\gamma\gamma}$ is taken from Ref. 6.

The statistical error is 0.015 keV, and the principle contribution to the systematic error is from the uncertainty in the shape of the continuum spectrum. Figure 10.5 shows the resonant contribution to the cross section assumed in the fit, including the fitted value of the f' two-photon width. The resonances all are assumed to be produced purely with helicity two.

Table 10.2 compares the DELCO result with previous measurements. The DELCO spectrum has been analyzed in the same way as that of TASSO,[7] so some of the systematic effects should be the same for the two experiments. Therefore, there may be some discrepancy between TASSO and DELCO. The *PEP-4/PEP-9* spectrum is analyzed without including interference between the three tensor resonances. If the same is done for the DELCO spectrum, then the data fit just as well as with interference included (assuming the same background shape), while the fitted two-photon width for the f' is increased by a factor of 1.8 up to 0.13 keV.

The ratio of the DELCO measurements for the two-photon widths of the f

Table 10.2. Comparison of measurements and limits on $\Gamma_{f'\to\gamma\gamma}$ between several experiments. For each measurement quoted, the first error is statistical and the second is systematic.

Collaboration	Reference	$\Gamma_{f'\to\gamma\gamma} \cdot \mathrm{BR}(f' \to K\overline{K})$ [keV]
Mark II, *SPEAR* data	75	< 0.6
TASSO	7	$0.11 \pm 0.02 \pm 0.04$
PEP-4/PEP-9	5	$0.12 \pm 0.06 \pm 0.06$
DELCO, this thesis		$0.070 \pm 0.015 \pm 0.035$

and f' may be compared with the $SU(3)$ predictions expressed by Eqn. 1.10. To do so, the branching ratio for the f' decaying to $K\overline{K}$ is assumed to be greater than 0.5, as is consistent with the estimate $\Gamma_{f'\to K\overline{K}} = 55 \pm 22\,\mathrm{MeV}$ from Ref. 76. Since the quark model does not consider any consequences of the finite width of the resonances, and since the experimental errors on the f' two-photon width are so large that it does not matter anyway, the value of the f two-photon width obtained from the non-unitarized model is used. Figure 10.6*a* compares the DELCO results with $SU(3)$ predictions as a function of the mixing angle. Two separate regions are allowed when solving for the mixing angle, but prior knowledge favors the solution most near to ideal mixing:

$$\Theta = 28^\circ \pm 4^\circ. \tag{10.6}$$

This agrees well with the prediction $\Theta \approx 28^\circ$ obtained from the mass differences of particles in the tensor nonet.[77] Figure 10.6*b* shows the comparison between $SU(3)$ predictions and data for the ratio of the f and A_2 two-photon widths, where the value for the A_2 two-photon width is taken from Ref. 6. For a mixing angle of 28°, the $SU(3)$ prediction is outside of the experimental error limits, but only slightly so. Both theoretical and experimental uncertainties are large enough that one must conclude that the data are in agreement with these simple predictions of the nonrelativistic quark model and $SU(3)$ symmetry.

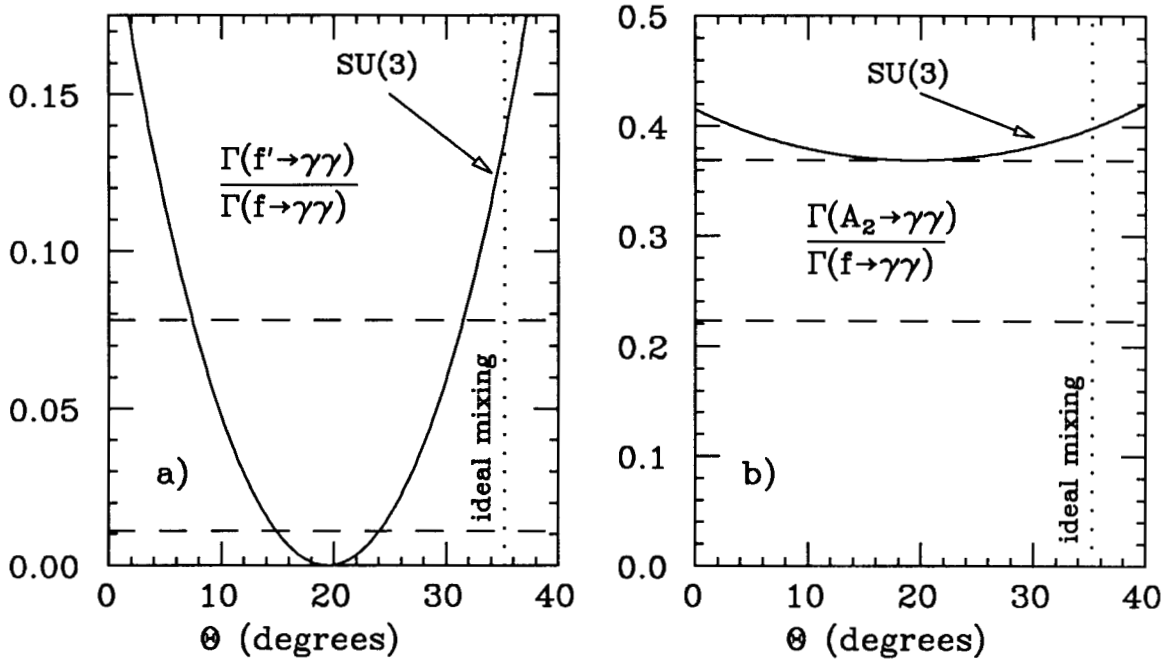

Figure 10.6. $SU(3)$ quark model predictions for the ratios of two-photon widths as functions of the mixing angle. The solid curves represent the predictions of Eqn. 1.10, while the dashed lines give the upper and lower one-standard-deviation limits on the measured ratios of partial widths.

10.4 Cross Section for $\gamma\gamma \to p\bar{p}$

From a sample of 23 events from the process $e^+e^- \to e^+e^-p\bar{p}$ in the proton-pair mass range $2.2 < W < 2.9\,\mathrm{GeV}$, the average cross section within the angular acceptance $-0.6 < \cos\theta_{\mathrm{cms}} < 0.6$ has been measured to be

$$\sigma_{\gamma\gamma\to p\bar{p}} = 1.2 \pm 0.5\,\mathrm{nb}, \qquad (2.2 < W < 2.9\,\mathrm{GeV},\ |\cos\theta| < 0.6). \tag{10.7}$$

The TASSO collaboration has published[78] results for this channel based on a sample of 72 events, which are enough to see the forms of invariant mass and angular distributions. The angular distribution is flat, while the invariant-mass distribution falls from about 4 nb at $W = 2\,\mathrm{GeV}$ to less than 0.5 nb above $W = 3\,\mathrm{GeV}$. Averaging the TASSO points over the range measured by DELCO gives $\sigma_{\gamma\gamma\to p\bar{p}} \approx 1.8\,\mathrm{nb}$ for $-0.6 < \cos\theta_{\mathrm{cms}} < 0.6$, which is in agreement with the DELCO result.

The Born cross section for $\gamma\gamma \to p\bar{p}$ integrated over $-0.6 < \cos\theta_{\rm cms} < 0.6$ is an average of 24.5 nb over the range $2.2 < W < 2.9$ GeV, which is a factor of 20 greater than the DELCO measurement. That is not surprising, since the proton is a poor approximation for a point Dirac particle. QCD calculations for this process have been attempted using methods which are similar to those discussed for meson pairs in Chapter 7, but considerably more complicated, with many more Feynman diagrams and greater uncertainty about the wave functions and normalization. TASSO compares the calculations of Damgaard[79] with their measurements, and they find that the calculated cross sections are a factor of 3 to 5 low. Another calculation of the same process by Farrar *et al.*[80] predicts that the cross section is a factor of 20 to 100 lower than the prediction of Ref. 79 and has a flatter angular distribution, even though the same assumptions are made about the proton wave function. Farrar *et al.* estimate that the momentum transfer in the collision should be greater than 5 GeV for such calculations to be valid, especially with an asymptotic form for the proton wave function. Since that is at least a factor of two greater than the momentum transfers observed by DELCO and TASSO, they repeat the calculations with a proton wave function recently proposed by Chernyak and Zhitnitsky[81] and find better agreement with the data. For example, they predict a cross section of 0.17 nb integrated over the angular range $-0.6 < \cos\theta_{\rm cms} < 0.6$ at $W = 2.4$ GeV.

Appendix A. Integration of the EPA spectrum

The experimental implications of the EPA spectrum can be studied by making simple integrations with limits determined by only the most significant features of the detector acceptance. For two-prong production, if some additional approximations are made, then the integrations can easily be done analytically, with the nice result that the salient features quickly are exposed in an intuitive manner. Integrations of more complex final states and over more detailed models of the acceptance are done with Monte Carlo techniques.

It is instructive to carry out an integration of the differential cross section for $e^+e^- \to e^+e^-e^+e^-$ over what is roughly the DELCO acceptance, in order to obtain the distribution of the invariant mass of the electron pair which is observed in the central detector. This exercise gives an understanding of the behavior of the invariant-mass spectrum for production of pairs of fermions and also provides an understanding of the effects of the limited detector acceptance. Electron pairs are of special interest because ultrarelativistic approximations can readily be made and because that is a channel which is easily observed by DELCO.

A procedure for doing such integrations for general two-prong final states and a number of typical acceptance cuts has been given in detail by A. Courau.[82] Here we give just an outline of the calculation as it is done to obtain the invariant-mass distribution of the electron pairs. The first step is to integrate over the Q^2 dependence of the photon flux of Eqn. 2.4 from $Q^2_{\text{min.}}$ up to some value $Q^2_{\text{max.}}$, which generally is determined by experimental constraints. Defining $\Delta \equiv (Q^2_{\text{max.}} - Q^2_{\text{min.}})/Q^2_{\text{min.}}$, one finds

$$\mathrm{d}n_i = \frac{\alpha}{\pi} S(x_i) \frac{\mathrm{d}x_i}{x_i}\,, \tag{A.1}$$

with

$$\begin{aligned} S(x_i) &= (1 - x_i + \tfrac{1}{2}x_i^2)\ln(1+\Delta^2) - (1-x_i)[1 - 1/(1+\Delta^2)] \\ &\approx 2(1 - x_i + \tfrac{1}{2}x_i^2)\ln\Delta - (1-x_i)\,. \end{aligned} \tag{A.2}$$

Using this photon flux along with the cross section for $\gamma\gamma \to e^+e^-$, given for the case of relativistic electrons by

$$\frac{d\sigma_{\gamma\gamma}}{du\,dW} = \frac{2\pi\alpha^2}{W^2}\frac{1+u^2}{1-u^2}, \qquad u \equiv \cos\theta_{\rm cms}, \tag{A.3}$$

results in the differential cross section

$$\frac{d^3\sigma}{dx_1\,dx_2\,du} = \frac{\alpha^4}{2\pi E^2}\frac{S(x_1)S(x_2)}{x_1x_2}\frac{2E}{W}\frac{1+u^2}{1-u^2}. \tag{A.4}$$

In the limit of zero-angle scattering of the beam electrons, the relations $Z^2 \equiv (W/2E)^2 = x_1x_2$ and $x_i = Ze^{\pm y}$ may be used, where $y = \tanh^{-1}\beta$ and βc is the velocity of the $\gamma\gamma$ system along the beam axis. Changing variables in Eqn. A.4 gives

$$\frac{d^3\sigma}{dZ\,dy\,du} = \frac{\alpha^4}{\pi E^2}\frac{1}{Z^3}S(Ze^y)S(Ze^{-y})\frac{1+u^2}{1-u^2} \tag{A.5}$$

Already it is evident that the behavior of the invariant-mass spectrum is dominated by a factor of $1/W^3$. To complete the calculation, both u and y must be integrated over the experimental acceptance.

Let us define the acceptance in such a way that only the most significant limits of DELCO are accounted for. These are the angular acceptance in θ and the lower momentum limit defined by the detector trigger. Neither quantity is cut off sharply at its limits by the detector itself. In the analysis, however, sharp cuts are made which are well inside the complicated boundary of the detector hardware. These cuts are made on $\cos\theta_{\rm lab}$ and W, which is convenient for the integration.

If first the rapidity, y, and then $\cos\theta$ are integrated over, the integration limits are as follows. The rapidity is limited by both the energy (since $x_i < 1$) and the angular acceptance ($|\cos\theta| \le u_0$), so the upper limit on y is the minimum of $\ln(1/Z)$ and $(\tanh^{-1}u_0 - \tanh^{-1}u)$. Because of symmetry in $\cos\theta$, it is only

necessary to integrate over half of the angular range, so the lower limit can be taken to be zero. Then the integration over u can be done from 0 to u_0.

Finally, the upper limit on the integration over Q^2 is yet to be specified. If the experimental limit is imposed by anti-tagging of the scattered electrons, then

$$\Delta_i = \frac{E}{m_e}\frac{1-x_i}{x_i}(2\sin\theta_m/2)\,, \qquad (A.6)$$

where θ_m is the minimum tagging angle. Usually, a more important limit is produced by cuts on the transverse momentum, $k_\perp$, of the electron pair. When applying either of these limits to the integration, it is possible to assume that all of the contribution near the limits comes from scattering of one beam electron, because the probability for both electrons to scatter at large angles is relatively minute. In that case, $Q^2 \approx k_\perp^2$, so a cut on $k_\perp$ is directly a cut on the Q^2 of the virtual photons.

For DELCO, some typical values used are $u_0 = 0.6$, $W_{\text{min.}} = 0.6\,\text{GeV}$, and $k_\perp \leq 0.2W$. Integrating the cross section of Eqn. A.5 over this acceptance yields the mass distribution of Fig. A.1*a*. Because the integration region is rectangular for most values of W, there is little deviation of the mass distribution from the simple $1/W^3$ behavior. Included in Fig. A.1 are two additional curves for larger angular acceptances, so one can see the drastic reduction in the cross section due to the limited angular acceptance.

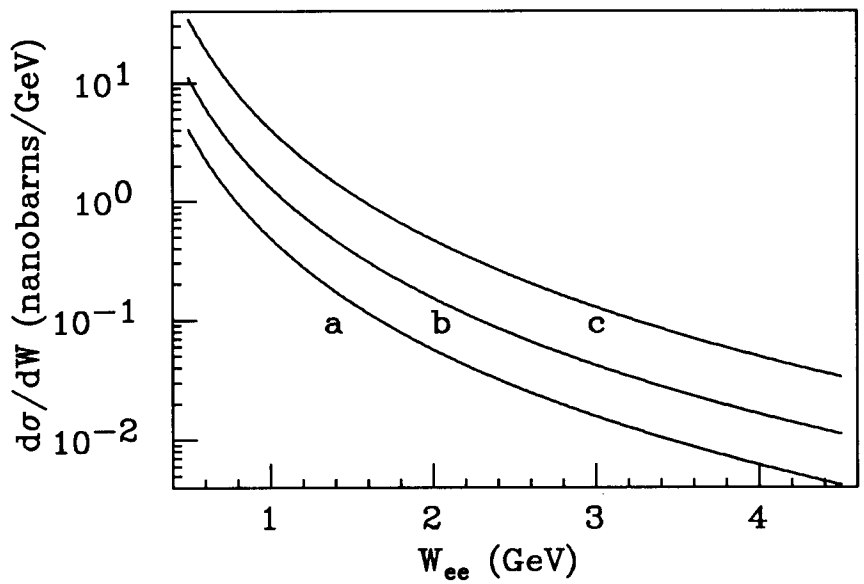

Figure A.1. The invariant-mass differential cross section for e^+e^- pairs from $e^+e^- \to e^+e^-e^+e^-$. The acceptance for the pair observed in the central detector is defined to be $k_\perp \leq 0.2W$ and (a) $|\cos\theta| \leq 0.60$, (b) $|\cos\theta| \leq 0.80$, (c) $|\cos\theta| \leq 0.95$

Appendix B. Monte Carlo Integration and Event Generation

In Appendix A an integration of the $e^+e^- \rightarrow e^+e^-e^+e^-$ cross section was done over a simplified detector acceptance by using the equivalent photon approximation. Any integration involving a more complex region or a more complicated spectrum is best done by Monte Carlo methods. This chapter first provides some general background about the use of Monte Carlo integration and then discusses the specific calculations used in the data analysis.[83]

B.1 The Monte Carlo Method

The basis for Monte Carlo integration is the integral expression for the mean of a function:

$$\overline{f} = \frac{1}{V}\int f(x_1 \ldots x_n)\,\mathrm{d}V\,, \qquad V \equiv \int \mathrm{d}V\,. \tag{B.1}$$

Since the mean may be approximated by an average over many randomly selected points within the n-dimensional volume, then so may the integral. In practice, the integration region often is so complex that the integral $V = \int \mathrm{d}V$ also must be done by Monte Carlo methods. The usual approach is to use a *hit-or-miss* method. One randomly chooses points from a uniform distribution in an n-dimensional box which contains the actual region. If a point falls outside the region, then it is rejected. The ratio of the number of points retained to the total number selected times the volume of the box gives the volume of the desired region.

Extending this idea gives a method for generating differential distributions of $f(x_1 \ldots x_n)$ in any variable $v = v(x_1 \ldots x_n)$. Any bin in the range of v defines an n-dimensional integration region which is contained within the full region. It follows that each time a point is selected which gives a value for v which falls within the ith bin, then that bin should be incremented by the amount $f/(\Delta v_i \cdot N)$, where Δv_i is the bin width and N is the total number of points selected.

The Monte Carlo procedure gives only an approximation to the integral, so it is important to evaluate the uncertainty in the result. In contrast to most

numerical integration methods, this estimate is easy to produce. Its square is given by $\sigma^2 = V(f)/N$, where $V(f)$ is the variance of the function f. Calculating it requires integrating the square of the function, which is done by Monte Carlo also. Thus the variance is calculated from the formula

$$V(f) = \left[\frac{\sum_{j=1}^{N}[f(x_1^j \ldots x_n^j) - \overline{f}]^2}{N}\right]^{\frac{1}{2}} . \qquad (B.2)$$

If the volume of the region is calculated by the hit-or-miss method, then that introduces further uncertainty. It becomes especially important for the case of small bins in a differential distribution, for which the number of counts in a given bin have a Poisson distribution. Then the additional uncertainty is approximately $\sigma_i = \overline{f}_i/\sqrt{n_i}$, where $\overline{f}_i$ is the average of f over the ith bin and n_i is the number of bin entries.

It is clear that in all cases the uncertainty decreases like $1/\sqrt{N}$ as N increases. It is remarkable that this remains true no matter how many dimensions are included in the integration. Even so, the variance may in fact be so large that an absurdly large N is necessary to bring the error down to a reasonable level. That is bound to be a problem if the function to be integrated has one or more large peaks. In such cases, special methods should be used to reduce the variance. One way is to divide the region into a number of pieces, so the integral is a sum of integrations over small regions in which the function does not vary greatly. That alone generally will reduce the variance, but a better reduction is obtained if the number of points chosen in each region is taken to be proportional to the average function value within that region. An iterative procedure can be used which uses the results of the integration from one iteration to provide the number of points to be calculated in each region for the next iteration.

Such *importance sampling* often can be done analytically by using explicit knowledge about the behavior of the function to be integrated. The method simply amounts to a change of integration variables. Consider a one-dimensional

case for simplicity. The trick is to find a simple function, $g(x)$, which has the same behavior in the peaks as the more complicated $f(x)$. For convenience, the normalization $\int_a^b g(x)\,\mathrm{d}x = 1$ is assumed, where a and b define the boundary for the Monte Carlo integration. For each iteration a uniform random number R_j between 0 and 1 is generated, and a new variable x_j is calculated from

$$R_j = \int_a^{x_j} g(y)\,\mathrm{d}y, \qquad 0 \leq R_j \leq 1\,. \tag{B.3}$$

After N iterations, an estimate of the integral is given by $(1/N)\sum_j f(x_j)/g(x_j)$. Note that if $g = f$ then the variance is zero. To make use of that fact, however, one must already know the analytic solution to the integral. It is important to realize that, in the multidimensional case, even if $f = g$ the integral still will have some uncertainty if the region boundaries are so complicated that the hit-or-miss method must be used.

In experimental physics, the most useful aspect of Monte Carlo integration is that it is a simple method for integrating over arbitrarily complex regions. In fact, the region may be taken to be defined by a very detailed simulation of the apparatus, with all sorts of inefficiencies and resolution effects included. Usually histograms are made of the various kinematic variables, just as is done with data. In such a case the analysis is simplified if the histograms can be accumulated without including weights. That may be done by using the hit-or-miss method. The point in the space $\{x_i\}$ is chosen as usual, using some variance reduction technique if necessary. Let w represent the weight, which simply is $f(x_1 \ldots x_n)$ if importance sampling is not used. A uniform random number R is selected, and with $w_{\text{max.}}$ being the maximum weight over the region, the point is rejected if $R \cdot w_{\text{max.}} > w$. A lot of calculation time will be wasted if w has any significant peaks, so in practice it often is necessary to divide the region into many subregions and then estimate the maximum weight for each.

An integration made without weights almost always is considerably less efficient than one which uses the weights, so it should be avoided unless there

is a good reason for it. The advantages of an unweighted *event generator* often can be more important, however. The simulated events can be treated just as the data are, and the uncertainty in each bin always is simply the square root of the bin contents. Furthermore, it is common for the simulation of the apparatus to require much more computation than the event generation, so there is a danger of wasting a lot of time simulating events with very small weights if unweighted events are not produced.

B.2 Monte Carlo Integration of the EPA Spectrum

A Monte Carlo program was written for the DELCO analysis to generate $\gamma\gamma$ states according to the EPA spectrum of equations 2.14 and 2.15.[84] It can be used in conjunction with a variety of other programs for generating the final state from the $\gamma\gamma$ system, and it is interfaced into the DELCO detector simulation software. Here the program is illustrated by considering the specific case of production of lepton pairs.

We assume that the $\gamma\gamma \to X$ cross section has the typical form

$$\frac{\mathrm{d}\sigma}{\mathrm{d}u\,\mathrm{d}W} = \frac{2\pi}{W^2} f(u,W)\,. \tag{B.4}$$

For the EPA spectrum, a change of variables is made from the set $\{Q_1^2, Q_2^2, x_1, x_2\}$ to the set $\{Z, y, t_1^2, t_2^2\}$, where we have *defined*

$$Z \equiv x_1 x_2\,, \qquad y \equiv \tfrac{1}{2}\ln\frac{x_1}{x_2}\,, \qquad t_i^2 \equiv \frac{Q_i^2}{Q^2_{\text{min.}}}\,. \tag{B.5}$$

The limits between which these variables must be integrated should be chosen to be somewhat outside the acceptance of the detector. In particular, Z is only approximately proportional to W, so it is a mistake to set the Z limits exactly at the acceptance limits in W. For all the produced particles to be within the angular acceptance, it is necessary, though not sufficient, that $|\tanh y|$ be smaller

than u_0, the upper limit on $\cos\theta$. Since the cross section is dominated by events with t^2 close to unity, while the experimental limits are well out on the tail of the distribution, then the efficiency is not unduly harmed by taking the limits on t^2 to be large and rejecting events with scattering angles too large for the experiment. $1 \leq t_i^2 \leq E/m_e$ is chosen as the appropriate integration range.

In the new variables, the cross section is

$$\mathrm{d}\sigma = \frac{2\alpha^2}{\pi^2} S(Ze^y, t_1^2)\, S(Ze^{-y}, t_2^2) \frac{\mathrm{d}t_1^2}{t_1^2} \frac{\mathrm{d}t_2^2}{t_2^2} \frac{\mathrm{d}Z}{Z^3} \mathrm{d}y \, \frac{Z^2}{W^2}\, 4\pi f(u, W)\, \mathrm{d}u\,, \qquad (B.6)$$

where $S(x, t^2) \equiv \left[(1 - x + \frac{1}{2}x^2) - (1-x)/t^2\right]$. The $1/t_i$ and $1/Z^3$ behavior must be removed by importance sampling. To do so, the variables are generated as follows from four uniform random numbers R_i.

$$\begin{aligned} R_i =& \frac{1}{\ln(E^2/m_e^2)} \int_1^{t_i^2} \frac{\mathrm{d}x}{x}, \qquad i = 1,2 \\ R_3 =& \left[\frac{1}{2}\left(\frac{1}{Z_1^2} - \frac{1}{Z_2^2}\right)\right]^{-1} \int_{Z_1}^{Z} \frac{\mathrm{d}x}{x^3} \\ y =& (2R_4 - 1) \cdot \tanh^{-1} u_0\,. \end{aligned} \qquad (B.7)$$

The first two expressions of Eqn. B.7 are easily inverted to give the formulas

$$\begin{aligned} t_i^2 =& \exp(2R_i \ln \frac{E}{m_e}) \\ Z =& \left[\frac{1}{Z_1^2} - \left(\frac{1}{Z_1^2} - \frac{1}{Z_2^2}\right) R_3\right]^{-\frac{1}{2}}\,. \end{aligned} \qquad (B.8)$$

Once the variables have been chosen, it is possible to calculate the momenta of the scattered electrons and of the $\gamma\gamma$ state. At that point, the event should be rejected if the scattering angle of either electron is larger than the maximum value allowed experimentally. The weight for the event, aside from additional factors

resulting from the cross section for $\gamma\gamma \to X$, is

$$w_{\gamma\gamma} = \frac{2\alpha^2}{\pi^2} S(Ze^y, t_1^2)\, S(Ze^{-y}, t_2^2) \times [\ln(E^2/m_e^2)]^2 \left[\frac{1}{2}\left(\frac{1}{Z_1^2} - \frac{1}{Z_2^2}\right)\right] [2\tanh^{-1} u_0] \frac{Z^2}{W^2}\,. \qquad (B.9)$$

The variance of this weight is small, especially compared with the variance of the original integrand, Eqn. B.6. Therefore, the Monte Carlo is efficient, and it is practical to use it for generation of unweighted events. To do so, first the maximum weight is estimated, and then all events with $R_5 \cdot w_{\gamma\gamma}^{\text{max.}} > w_{\gamma\gamma}$ are rejected.

B.3 Including the Cross Section for $\gamma\gamma \to l^+l^-$

The cross section for production of lepton pairs from two real photons is, to leading order in QED,[85]

$$\frac{\mathrm{d}\sigma}{\mathrm{d}\Omega} = \frac{\alpha^2}{W^2}\left[2(2-\beta_l^2) - (1-\beta_l^2 u^2) - 2\frac{(1-\beta_l^2)^2}{1-\beta_l^2 u^2}\right]\frac{\beta_l}{1-\beta_l^2 u^2}\,, \qquad (B.10)$$

where $\mathrm{d}\Omega = \mathrm{d}u\,\mathrm{d}\phi$ is the volume element in the center-of-mass of the $\gamma\gamma$ system. The variable $u = \cos\theta$ is defined with respect to the axis made by the colliding photons in their center-of-mass system, but for untagged events, that is very close to being parallel to the laboratory z axis, along which the electron beams travel. Note that $\beta_l = \sqrt{1-(m_l/k^0)^2}$, where $k^0 = W/2$, so the cross section contains a dependence on W, which in turn is a function of both Z and y. Therefore, the integration does not contain the angular integral as a separate factor. When doing importance sampling in such a multidimensional integral, it usually is only possible to consider one dimension at a time. Since importance sampling is equivalent to a change of variables, if the transformation function used depends on more than one of the variables, one must be careful to include properly the Jacobian of the transformation. So far, all the changes of variables made to Eqn. B.6 have involved

only one variable at a time. Here we make a change of variables from u to $R(u)$ with a dependence on β, which in turn is a function of both Z and y:

$$R(u) = \frac{\tanh^{-1}\beta_l u}{\tanh^{-1}\beta_l u_0}\,. \tag{B.11}$$

In this case, the contribution to the Jacobian simply is

$$1/R'(u) = \tanh^{-1}\beta u_0\,\frac{1-\beta_l^2 u^2}{\beta_l}\,. \tag{B.12}$$

In other words, we can generate R uniformly from 0 to 1 and calculate $u = \tanh(R\tanh^{-1}\beta u_0)/\beta$. Then the overall weight for an event is Eqn. B.9 times

$$4\pi\alpha^2\left[2(2-\beta^2)-(1-\beta^2u^2)-2\frac{(1-\beta^2)^2}{1-\beta^2u^2}\right]\tanh^{-1}\beta_l u_0\,, \tag{B.13}$$

where an extra factor of 2 has been introduced so that the integration can be done on only half of the symmetric range of $-u_0$ to u_0.

B.4 Monte Carlo for the Single-Tag Luminosity Function

For the analysis of tagged events which are not entirely governed by QED, the single-tag luminosity function of Section 2.4 is used in place of the EPA spectrum. The set of variables to generate are for this case $\{x_1, x_2, \theta_2\}$, where θ_2 is the scattering angle of the tagged electron. An equivalent set is $\{Z, y, \theta_2\}$, where Z and y are defined in Eqn. B.5. Again, Z and y are generated according to the formulas of equations B.7 and B.8, but θ_2 is generated according to a $\cot\frac{1}{2}\theta_2$ distribution, between the limits $\theta_{\rm min}$ and $\theta_{\rm max}$, by the formula

$$\theta_2 = 2\sin^{-1}\left\{\sin\tfrac{1}{2}\theta_{\rm min}\exp\left[R\ln\left(\frac{\sin\frac{1}{2}\theta_{\rm max}}{\sin\frac{1}{2}\theta_{\rm min}}\right)\right]\right\}\,, \tag{B.14}$$

where R is a uniform random number between zero and one.

The event weight follows from Eqn. 2.18 and is given by

$$
\begin{aligned}
w = {} & \frac{\alpha^2}{2\pi^2} \ln\left(\frac{\sin\frac{1}{2}\theta_{\max}}{\sin\frac{1}{2}\theta_{\min}}\right)\left(\frac{1}{Z_1^2} - \frac{1}{Z_2^2}\right)\tanh^{-1} u_0 \\
& \times \left[\frac{(K+2x_1)^2}{K^2} + 1\right]\left[\left(\frac{[K - 2(x_2 + (Q_2/2E)^2)]^2}{K^2} + 1\right)\right. \\
& \left. \times \ln\left(\frac{2E}{m}\frac{(1-x_1)}{x_1}\sin\tfrac{1}{2}\hat{\theta}_{\min}\right) - 2\frac{1-x_1}{x_1^2}\right] \cdot K \cdot \frac{Z^4}{W^2} \cdot w_X \,,
\end{aligned}
\tag{B.15}
$$

where $K \equiv (W^2 + Q_2^2)/4E^2$, $\hat{\theta}_{\min}$ is the minimum tagging angle for the apparatus, and w_X/W^2 is the weight for the process $\gamma\gamma \to X$. Although it is by no means obvious at a glance, for the range of θ available for tagging in DELCO this weight has a reasonably small variance, so it can be used for generation of unweighted events without any serious inefficiency, as long as w_X also is reasonably well optimized.

B.5 Calculations Without EPA

If it is necessary to investigate a region of Q^2 in which EPA is not valid, then more complex calculations must be performed. Monte Carlo programs have been written to handle some specific cases.[22,32] When the Feynman diagrams are complicated and large in number, it is prohibitively difficult to sum the amplitudes and square them analytically. Therefore, the programs calculate the complex amplitudes numerically, add them together, and square them. Much care must be exercised to avoid numerical instabilities.

The program which we use is the one of Ref. 22 for the process $e^+e^- \to e^+e^-l^+l^-$. There are contributions to this process in addition to the two double-bremsstrahlung (*multiperipheral*) diagrams, but they give no significant contribution to the cross section in the experimental situation where only the l^+l^- are observed in the detector.[32] Six diagrams are included in Ref. 22, whereas for the four-electron final state there actually are a total of thirty six. The six which

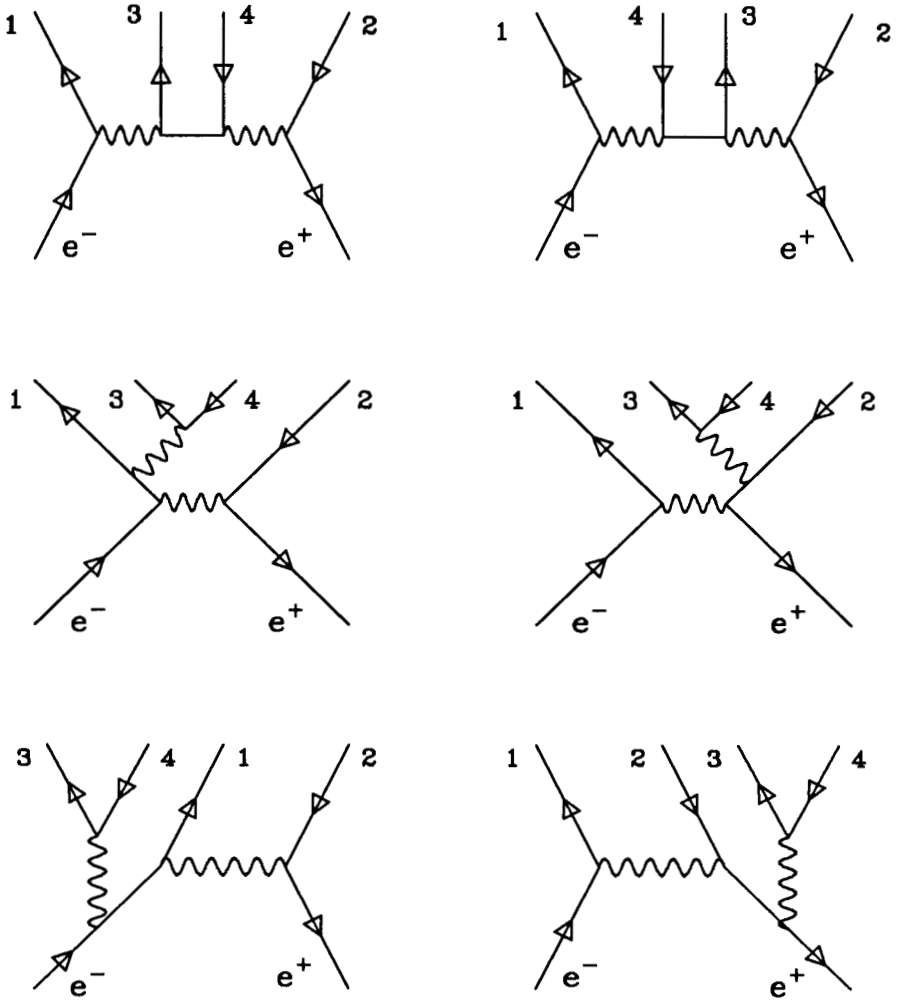

Figure B.1. Six diagrams for the process $e^+e^- \to e^+e^-l^+l^-$. These are the diagrams included in the calculation of Ref. 22.

are included are shown in Fig. B.1. The diagrams in which the beam electrons annihilate are entirely neglected, and for the case of four final-state electrons, interference between the fermions originating in the beam and those originating from the $\gamma\gamma$ interaction is neglected. A general purpose adaptive Monte Carlo routine called VEGAS[86] is used to do the integration. VEGAS works by the method of importance sampling, but rather than using continuous functions to approximate the integrand, which would require prior knowledge of the integrand, it uses step functions, which are adjusted iteratively to adapt to the integrand in use.

The procedure is to divide each axis of the n-dimensional space into N intervals. Then the probability of choosing a point from any given interval is defined to be a constant. Initially the intervals along an axis are of equal length. During the first iteration a specified number of function evaluations are made. They give estimates for the mean values of the function in each interval, which are used to change the grid spacing for the next iteration. The intervals are made more narrow where the function value is relatively large, so in the next iteration more points will be concentrated there than where the function is small.

All function evaluations in all iterations are used in the determination of the integral and its uncertainty. Individual iterations also produce a value for the integral and an associated error estimate. The χ^2 of all the values should not greatly exceed the number of iterations, or else one must suspect that the procedure has become unstable. Such an instability could be due to making not enough function evaluations in each iteration. That number and the number of iterations must be chosen by the user. A good choice will result in a reasonable χ^2 per iteration and a standard deviation per iteration which decreases at first but levels off before the last iteration is made.

The program also can be used to generate unweighted events.[87] To do so, VEGAS is run through several iterations just for the purpose of finding the optimum grid spacing. At this time, the rough limits of the detector acceptance are included by defining the integrand to be zero outside of it. Therefore, after the initial iteration, points will not be chosen which lie outside of the acceptance. After the grid spacing is specified, another program considers the behavior of the integrand and estimates its maximum for each interval. After that, points are chosen according to the optimized grid and kept or rejected according the ratio of the function value to the maximum of the interval. This procedure provides for efficient generation of events within the detector acceptance even with such a complicated integrand.

It is of interest at this point to compare the Vermaseren program with the

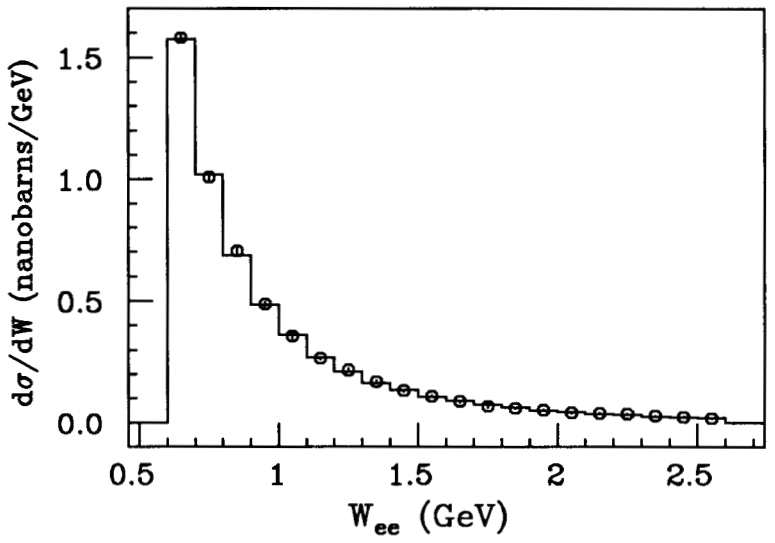

Figure B.2. Two calculations of the e^+e^- invariant-mass distribution. The line histogram is from the EPA Monte Carlo, and the points are from the Vermaseren Monte Carlo.

EPA Monte Carlo described in the previous section. Figure B.2 and Fig. B.3 show for the electron pair observed within the DELCO acceptance the invariant mass and angular distributions. The acceptance has been simplified and is defined by only the cuts $0.6\,\mathrm{GeV} \leq W \leq 2.6\,\mathrm{GeV}$, $-0.6 \leq \cos\theta \leq 0.6$, and $k_\perp \leq \min(0.2W, 0.3\,\mathrm{GeV})$. Within such an acceptance, EPA calculates well even the distribution of total transverse momentum ($k_\perp$), as shown in Fig. B.3. It is clear that as long as a strict cut is made on $k_\perp$, one can expect the EPA to be valid for all of the untagged analysis. Any resulting theoretical errors will be much smaller than the statistical uncertainty of the data.

The full leading-order calculation, including all 36 diagrams, has been done by Berends, Daverveldt, and Kleiss.[32] They also use variance reduction techniques to handle the sharp peaks that the cross section makes in various regions of the seven-dimensional space, but they do so explicitly, rather than rely upon an adaptive Monte Carlo integration routine. Different subsets of diagrams have differing peaking properties. For example, we already have seen from the EPA calculation of the first two diagrams in Fig. 4.1 (the multiperipheral diagrams) that they are

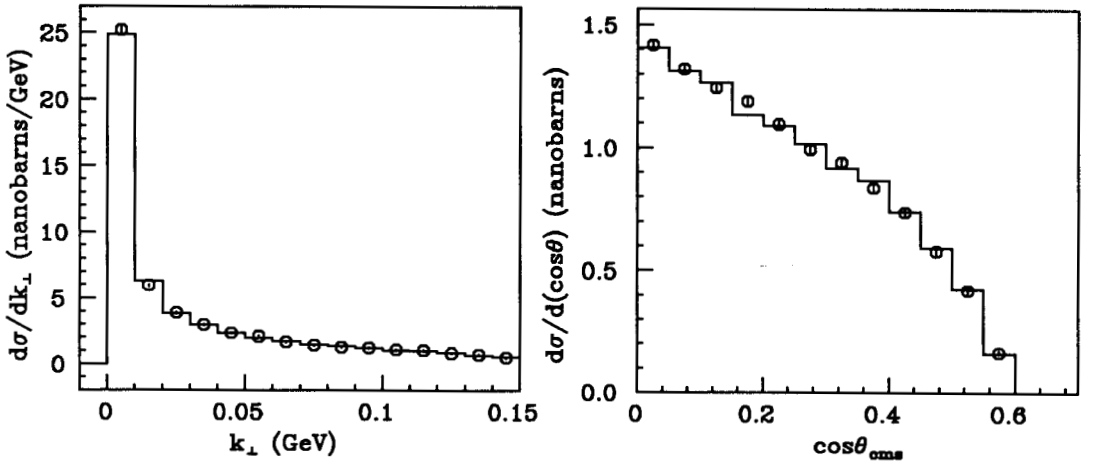

Figure B.3. Two calculations of the e^+e^- $k_\perp$ and $\theta_{\rm cms}$ distributions. The line histogram is from the EPA Monte Carlo, and the points are from the Vermaseren Monte Carlo.

characterized by sharp peaks at low invariant mass and low Q^2.† Other subsets have peaks in different regions of phase space.

The procedure used works by separating the diagrams into six subsets, where all diagrams in a particular subset give amplitudes which have a sharp peak, arising when the q^2 of one or more of the propagators becomes small, in the same region of phase space of the external particles. In each Monte Carlo iteration, one of the subsets is chosen with a probability proportional to its approximate contribution to the total cross section. An event is generated according to just the cross section for the chosen subset, so it is possible to choose the kinematic variables in a way which will cancel the peaks in that subset. The resulting sample of events is corrected by calculating for each the full cross section according to the entire set of diagrams and applying a rejection algorithm.

One result of their calculations is that for the experimental situation where only two of the electrons pass through the central detector, the two multiperipheral diagrams completely dominate the cross section. Therefore, for the DELCO

† For the four-electron final state, EPA includes only two of the permutations of the outgoing electron lines, thus ignoring interference between the scattered beam electrons and those from the $\gamma\gamma$ system.

analysis it is a safe approximation to use the Vermaseren Monte Carlo, or even to use the EPA Monte Carlo when untagged events are analyzed.

Appendix C. Unfolding Methods for Experimental Distributions

The procedure used in this thesis for unfolding kinematic distributions from the measured histograms is due to V. Blobel. In Ref. 88 he gives an excellent account of the justification and need for the method, a derivation of the equations, and an example calculation. Here we provide only a brief summary of how the calculation is done. The principle difference from Blobel's example is that, whereas his data is one dimensional, here we always must consider a multidimensional problem.

Even here, though, only one dimension is considered at a time. The problem with the other dimensions is only that they must be modeled properly in order that the efficiency corrections for the variable under consideration be correct. As a concrete example, let us consider unfolding the two-particle invariant mass distribution. In this case, for example, it is clear that the result will be correct only if the angular distributions are correct in the Monte Carlo which is used to calculate the efficiency. Let W represent the invariant mass, and let $W_a \leq W \leq W_b$ be the range in which we are interested. $f(W)$ represents the function to be determined—the result of the unfolding procedure.

The data is in the form of a histogram with n bins of equal width, where the value chosen for n depends on the number of events available and also on the experimental resolution of W. The extent to which $f(W)$ can be resolved is limited by the statistical precision of the data, so it must be represented by a finite number of parameters $a_1, a_2 \ldots a_m$, according to some expansion

$$f(x) = \sum_{i=1}^{m} a_i p_i(x) \,. \qquad (C.1)$$

The number chosen for m must be less than n, but otherwise it is not critical, unless it is much too small, because the regularization procedure to be discussed will automatically adjust the number of independent coefficients in the final result to be consistent with the statistical precision of the data.

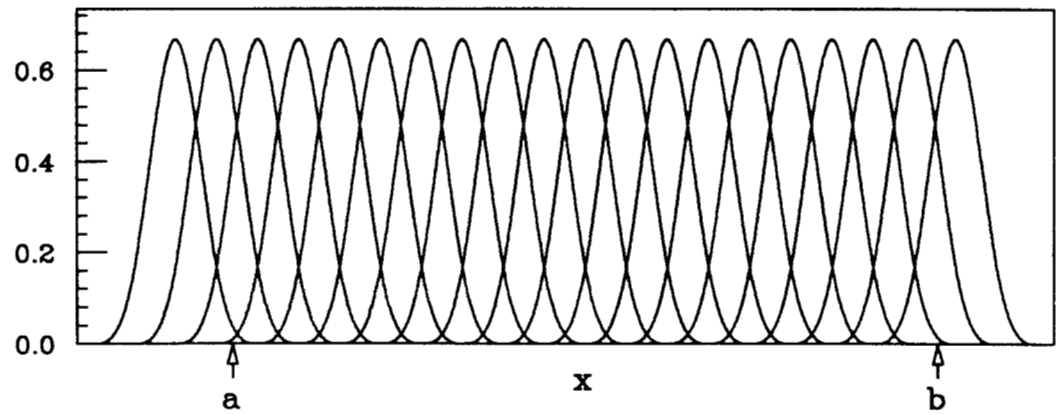

Figure C.1. A sequence of 20 cubic B-splines. They have the property that at any point x between a and b, the sum of all of the B-splines is unity.

The functions used for the $p_i(x)$ are cubic B-splines with equidistant knots. The range from W_a to W_b is divided into $m-3$ intervals of equal length $d = (W_b - W_a)/(m-3)$, and each of the B-splines is non-zero over a range of $4d$. Let t_i represent the position of the ith knot, so $t_4 = W_a$, $t_{m+1} = W_b$, and in general, $t_i = W_a + (i-4)/d$. Then the cubic B-splines are given by

$$b_i(x) = \begin{cases} \frac{1}{6}z^3 & z = (x - t_i)/d \quad t_i \le x < t_{i+1} \\ \frac{1}{6}[1 + 3(1 + z(1-z))z] & z = (x - t_{i+1})/d \quad t_{i+1} \le x < t_{i+2} \\ \frac{1}{6}[1 + 3(1 + z(1-z))(1-z)] & z = (x - t_{i+2})/d \quad t_{i+2} \le x < t_{i+3} \\ \frac{1}{6}[1 - z]^3 & z = (x - t_{i+3})/d \quad t_{i+3} \le x < t_{i+4} \\ 0 & \text{otherwise} \end{cases} . \tag{C.2}$$

Figure C.1 shows an example of 20 cubic B-splines spanning the interval in x between a and b.

Now let us represent the response function of the detector as $A(y, x)$, so the invariant-mass distribution which is observed is given by

$$g(W) = \int_{W_a}^{W_b} A(W, x) f(x)\, \mathrm{d}x = \sum_{i=1}^{m} a_i A_i(W)\,, \tag{C.3}$$

where the $A_i(W)$ are given by

$$A_i(W) = \int_{W_a}^{W_b} A(W,x)p_i(x)\,\mathrm{d}x\,. \qquad (C.4)$$

The function $g(W)$ is what actually is measured, but only as a histogram with a limited number of events, and therefore some statistical errors. The $A_i(W)$ also are produced as histograms from Monte Carlo events. The Monte Carlo events are generated according to some distribution $f_0(W)$, and all detector effects are simulated. After analyzing the Monte Carlo events just as is done for the data, m histograms of the measured invariant mass $\widetilde{W}$ are accumulated with weights given by $N \cdot p_i(W)$, where W is the generated invariant mass. N is an overall normalization given by the ratio of the integrated luminosity in data to the integrated luminosity generated by the Monte Carlo.

Since this really is a multidimensional problem, in order for the efficiencies to be calculated correctly and efficiently by Monte Carlo, it is best if f_0 is a reasonable approximation to f, and it if is necessary that all other kinematic variables are distributed in a close approximation to reality. That always may be checked by comparing the observed distributions with the Monte Carlo distributions after detector simulation. Thus the bin contents of the m histograms form an n-by-m matrix of elements A_{ij}, and Eqn. C.3 becomes

$$g_i = \sum_{j=1}^{m} A_{ij}a_j\,. \qquad (C.5)$$

Actually, this is completely true only if $f_0 = 1$; otherwise the resulting A_{ij} are such that the $f(W)$ produced by the unfolding procedure must be multiplied by $f_0(W)$ to give the desired result.

Given $\hat{g}_i$, the measured bin contents, Eqn. C.5 may be solved by a maximum likelihood method. The observed bin contents follow a Poisson distribution, for which the probability of observing the number $\hat{g}_i$ of events in the ith bin is $P(\hat{g}_i|g_i)$,

where

$$P(r|\mu) = e^{-\mu}\frac{\mu^r}{r!} \qquad r \in \{0, 1 \ldots \infty\}\,. \tag{C.6}$$

The g_i are the average or expected values of the bin contents, which we take to be given by Eqn. C.5; hence $P(\hat{g}_i|g_i)$ is a function of the parameters a_j. The likelihood function is formed from the product of the $P(\hat{g}_i|g_i)$ for all n bins, and its negative logarithm is proportional to

$$S(a) = \sum_{i=1}^{n} g_i - \sum_{i=1}^{n} \hat{g}_i \ln g_i\,. \tag{C.7}$$

The desired solution is the set of a_j which minimizes $S(a)$. However, one finds that such a solution is dominated by large oscillations due to amplification of the statistical errors inherent in the data.

To damp out the oscillations, a regularization term $\frac{1}{2}\tau \cdot r(a)$ is added to the log likelihood function, where $r(a)$ is a measure of the curvature of the solution $f(W)$:

$$r(a) = \int_{W_a}^{W_b} [f''(x)]^2 \mathrm{d}x = \sum_{i,j=1}^{m} a_i C_{ij} a_j\,. \tag{C.8}$$

C is a constant, symmetric, positive-semidefinite matrix and is easily calculated for the cubic B-splines. The regularization parameter τ is adjusted to an appropriate value as explained below.

The solution is calculated as follows. First define the derivative matrices

$$h_i = -\frac{\partial S}{\partial a_i} \qquad H_{ij} = \frac{\partial^2 S}{\partial a_i \partial a_j}\,. \tag{C.9}$$

These must be calculated assuming some initial guesses $\tilde{a}_i$ of the parameters a_i. What is done is first to calculate the solution assuming Gaussian distributions for the bin contents, in which case the log likelihood function is quadratic in a and no initial guess is needed. The Gaussian result then is used as a starting point for the first iteration of solving the problem with Poisson statistics. In practice,

few iterations are necessary—for high statistics the Gaussian approximation is itself good enough. Once the derivative matrices have been calculated, then the matrix U_1 is found which diagonalizes H, and another matrix U_2 is found which diagonalizes the matrix

$$C_1 \equiv D^{-1/2} U_1^T C U_1 D^{-1/2}, \quad \text{where} \quad D = U_1^T H U_1 . \tag{C.10}$$

First consider the unregularized solution ($\tau = 0$), which we denote by accenting with a bar. It may be written as

$$\overline{f}(W) = \sum_{i=1}^{m} \bar{a}'_j p'_j(W) , \tag{C.11}$$

where the $p'_j(x)$ are orthonormal polynomials given by

$$\begin{aligned} p'_i(x) &= \sum_{j=1}^{n} (U_1 D^{-1/2} U_2)_{ji}\, p_j(x) , \\ \bar{a}' &= U_2^T D^{-1/2} U_1^T (H\tilde{a} + h) . \end{aligned} \tag{C.12}$$

In this orthogonal space, denoted by accenting with a prime, the covariance matrix of the coefficients $\bar{a}'_i$ is simply the unit matrix. Therefore, any coefficient which satisfies $(\bar{a}'_i)^2 \leq 3.84$ is statistically compatible with zero at the 95% confidence level.

The contributions to the curvature of the individual orthonormal polynomials are given by S_{ii}, where $S = U_2^T C_1 U_2$. The coefficients $\bar{a}'_i$ should be arranged in order of increasing S_{ii}. Let m_0 be the smallest integer such that for $i > m_0$, all $\bar{a}'_i$ are compatible with zero. The coefficients of the regularized solution are given by

$$\hat{a}'_i = \frac{1}{1 + \tau S_{ii}} \bar{a}'_i , \tag{C.13}$$

so if we choose τ such that

$$m_0 = \sum_{i=1}^{m} \frac{1}{1 + \tau S_{ii}} , \tag{C.14}$$

then the coefficients are cut off smoothly at the point where they become statistically compatible with zero. The covariance matrix of the regulated solution is

$$V(\hat{a}')_{ij} = \frac{\delta_{ij}}{(1+\tau \cdot S_{ii})^2}, \qquad (C.15)$$

and both it and the coefficients $\hat{a}'$ may be transformed back to the original space by use of the matrix $U_1 D^{1/2} U_2$.

The final task is to convert the coefficients to a set of m_0 data points by integrating the solution $\hat{f}(W)$ over small contiguous regions of W and dividing each integral by the length of the particular region. The regions are chosen as being between the extrema of the polynomial $p'_{m_0+1}(W)$. Thus they are located about the m_0 zeroes of that polynomial, which has the effect of suppressing the contribution to the solution from the term $\hat{a}'_{m_0+1} p'_{m_0+1}(W)$ and also tends to give wider bins in regions of less statistical precision and reduce the correlations between data points. Since the integrals over the function $\hat{f}(W)$ are linear functions of the coefficients $\hat{a}_i$, then it is straightforward to calculate the covariance matrix for the data points as a linear transformation of the covariance matrix for the coefficients.

As mentioned above, if it is necessary, as is usually the case, that the Monte Carlo input distribution $f_0(W)$ not be uniform, then the unfolded data points must be multiplied by $f_0(W)$ to obtain the final result. In fact, for a multidimensional problem, f_0 is itself the result of an integration over several dimensions and is therefore usually not known analytically. What is done is to use the Monte Carlo generator itself to do the integration, giving a histogram representation of f_0. That histogram then is interpolated by cubic splines and integrated over the same regions in W as was the solution $\hat{f}$, which gives a set of Monte Carlo points to be directly multiplied by the m_0 points of the unfolded solution.

Finally, one has a measurement of the physical distribution of interest without any distortion due detector effects which are unique to the particular experiment.

The procedure is complicated because it is necessary to smooth oscillatory behavior in a manner which is compatible with the statistical precision and therefore unbiased. But the complications are worthwhile, because the result is meaningful even to one who is not familiar with the details of the experimental apparatus and methods. Often the result does not contain as many points as the original histograms, and the error bars may be larger. But that also is an advantage, because the points and error bars represent the true limitations of the apparatus. Resolutions effects inevitably decrease the statistical accuracy of an experiment, so the result should properly reflect those limitations.

REFERENCES

1. S.J. Brodsky and G.P. Lepage, *Large-Angle Two-Photon Exclusive Channels in Quantum Chromodynamics*, Phys. Rev. D **24** (1981) 24.
2. J.F. Gunion, D. Millers, and K. Sparks, *Q^2 Dependence of Exclusive Meson Production in Two-Photon Reactions*, UC Davis preprint (July 1985) 45pp.
3. J.R. Smith *et al.* (Mark II collaboration), *Pion Pair Production from $\gamma\gamma$ Collisions at PEP*, Phys. Rev. D **30** (1984) 851.
4. J. Boyer *et al.* (Mark II collaboration), *Charged Meson Pair Production in $\gamma\gamma$ Interactions*, SLAC-PUB-3780 and LBL-20280 (Sept. 1985) submitted to Phys. Rev. Lett.
5. W.G.J. Langeveld, *Pion and Kaon Pair-Production in Photon-Photon Collisions*, Ph.D. Thesis, Utrecht (1985).
6. Particle Data Group, *Review of Particle Properties*, Rev. Mod. Phys. **56** (April 1984).
7. M. Althoff *et al.* (TASSO collaboration), *Production of $K\overline{K}$-Pairs in Photon-Photon Collisions and the Excitation of the Tensor Meson $f'(1515)$*, Phys. Lett. **121B** (1983) 216.
8. H. Kolanoski, *Two-Photon Physics at e^+e^- Storage Rings*, Springer-Verlag, Berlin (1984).
9. C. Edwards *et al.* (Crystal Ball collaboration), *Production of $\pi^0\pi^0$ and $\pi^0\eta$ in Photon-Photon Collisions*, Phys. Lett. **110B** (1982) 82.
10. P. Grassberger and R. Kögerler, *Sum Rules for Elastic $\gamma\gamma$ Scattering and Meson Decays into Two Photons*, Nucl. Phys. B **106** (1976) 451.
11. M.S. Chanowitz, "Resonances in Photon-Photon Scattering," *Proceedings of the VIth International Workshop on Photon-Photon Collisions*, ed. R.L. Lander, World Scientific, Singapore (1985).
12. S.L. Adler, *Axial-Vector Vertex in Spinor Electrodynamics*, Phys. Rev. **177** (1969) 2426.

J.S. Bell and R. Jackiw, *A PCAC Puzzle: $\pi^0 \to \gamma\gamma$ in the σ-Model*, Nuovo Cimento **60A** (1969) 47.

13. Ch. Berger, "Two Photon Physics in the PLUTO Detector," *Proceedings of the International Workshop on $\gamma\gamma$ Collisions, Amiens*, ed. G. Cochard and P. Kessler, Lecture Notes in Physics Vol. 134, Springer-Verlag, Berlin (1980).
14. J.D. Bjorken and S.D. Drell, *Relativistic Quantum Mechanics*, McGraw-Hill, New York (1964).
15. V.M. Budnev *et al.*, *The Two-Photon Particle Production Process*, Physics Reports **15C** (1975) 241.
16. V.M. Budnev *et al.*, *op. cit.*, equation (5.12).
17. V.M. Budnev *et al.*, *op. cit.*, page 242.
18. V.M. Budnev *et al.*, *op. cit.*, page 246.
19. H. Kolanoski, *op. cit.*, Section 2.4.2.
20. J.H. Field, *Luminosity Functions for Two-Photon Processes in e^+e^- Collisions*, Nucl. Phys. B **168** (1980) 477.
    Ch. Berger and J.H. Field, *Luminosity Function for Two-Photon Processes in the Single Tagging Mode*, Nucl. Phys. B **187** (1981) 585.
21. G. Bonneau, M Gourdin, and F. Martin, *Inelastic Lepton (Anti)-Lepton Scattering and the Two-Photon Exchange Approximation*, Nucl. Phys. B **54** (1973) 573.
22. J. Smith, J.A.M. Vermaseren, and G. Grammer, *Two-Photon Production Processes at High Energy*, Phys. Rev. D **15** (1977) 3280.
23. J.J. Sakurai, *Vector Meson Dominance and High-Energy Electron-Positron inelastic scattering*, Phys. Rev. Lett. **22** (1969) 981.
24. J.J. Sakurai and D. Schildknecht, *Generalized Vector Dominance and Inelastic Electron-Proton Scattering*, Phys. Lett. **40B** (1972) 121.
    I.F. Ginzburg and V.G. Serbo, *Some Comments on the Total $\gamma\gamma \to$Hadron Section at High Energy*, Phys. Lett. **109B** (1982) 231.

25. G.B. Bowden, *et al.*, *A Sandwich Structure Beam Pipe for Storage Rings*, Nucl. Instr. & Meth. **228** (1984) 207.

26. V.L. Highland, *Some Practical Remarks on Multiple Scattering*, Nucl. Inst. & Meth. **129** (1975) 497, and *Erratum*, Nucl. Inst. & Meth. **161** (1979) 171.

27. H. Hinterberger and R. Winston, *Efficient Light Coupler for Threshold Čerenkov Counters*, Rev. Sci. Instr. 37 (1966) 1094.

28. D.E. Koop, *Prompt Electron Production in Electron-Positron Annihilation at* 29 GeV, Ph.D. thesis, California Institute of Technology (1984).

29. R.L. Ford and W.R. Nelson, *The EGS Code System: Computer Programs for the Monte Carlo Simulation of Electromagnetic Showers (Version 3)*, SLAC-0210 (1978) 277pp. We use Version 4, which is to be documented in SLAC-0265. However, it is very similar to Version 3.

30. K.C. Chandler and T.W. Armstrong, *Operating Instructions for the High-Energy Nucleon-Meson Transport Code HETC*, ORNL-4744, Oak Ridge Nat. Lab. (1972) 33pp.
T.W. Armstrong *et al.*, Nucl. Sci. Eng. **49** (1972) 82.
T.A. Gabriel, J.D. Amburgey, and B.L. Bishop, *"CALOR:" A Monte Carlo Program Package For the Design and Analysis of Calorimeter Systems*, ORNL/TM-5619, Oak Ridge Nat. Lab. (April 1977) 29pp.

31. H. Yamamoto, *A Study of Charged D^* Mesons Produced in e^+e^- Annihilation at $E_{\rm cm}$* = 29 GeV, Ph.D. thesis, California Institute of Technology (1985).

32. F.A. Berends, P.H. Daverveldt, and R. Kleiss, *Complete Lowest Order Calculation for Four-Lepton Final States in e^+e^- collisions*, Nucl. Phys. B **253** (1985) 441.
P.H. Daverveldt, *Monte Carlo Simulation of Two-Photon Processes*, Ph.D. thesis, Leiden (1985).

33. R. Kleiss, *Monte Carlo Simulation of Radiative Processes in Electron-Positron Scattering*, Ph.D. thesis, Leiden (1982).

34. G.B. Mills, *Charged Kaon Production in Tau Lepton Decays*, Ph.D. thesis, California Institute of Technology (1985).

H.D. Dahmen, L. Schulke, G. Zech, *Contributions of Weak Interactions to the Process* $e^+e^- \to \bar{\nu}_\tau X^+ \nu_\tau X^-$, Zeit. Phys. **C5** (1980) 71.

35. W.L. van Neerven and J.A.M. Vermaseren, *The Role of the Five-Point Function in Radiative Corrections to Two-Photon Physics*, Phys. Lett. **142B** (1984) 80.

36. F.A. Berends, P.H. Daverveldt, and R. Kleiss, *Radiative Corrections to the Process* $e^+e^- \to e^+e^-\mu^+\mu^-$, Nucl. Phys. B **253** (1985) 421.

37. G.B. Mills, Internal DELCO memorandum dated Nov. 16, 1983.

38. T. Sjöstrand, *The Lund Monte Carlo for* e^+e^- *Jet Physics*, Comput. Phys. Commun. **28** (1983) 229.

T. Sjöstrand, *The Lund Monte Carlo for Jet Fragmentation*, Comput. Phys. Commun. 27 (1982) 243.

39. Ch. Berger *et al.* (PLUTO collaboration), *Measurement of Exclusive* η' *Production in* $\gamma\gamma$ *Reactions*, Phys. Lett. **142B** (1984) 125.

40. G.P. Lepage and S.J. Brodsky, *Exclusive Processes in Perturbative Quantum Chromodynamics*, Phys. Rev. D **22** (1980) 2157.

41. See, for example, A. Roussarie *et al.* (Mark II collaboration), *Pion-Pair Production in Photon-Photon Collisions at SPEAR*, Phys. Lett. **105B** (1981) 304.

42. J. Werle, *Relativistic Theory of Reactions*, North-Holland, Amsterdam (1966).

43. J. Werle, *op. cit.*, equations 28.1 and 28.2.

44. J. Werle, *op. cit.*, equation 29.21.

45. J. Werle, *op. cit.*, equations 29.31 and 29.38.

46. C.N. Yang, *Selection Rules for the Dematerialization of a Particle into Two Photons*, Phys. Rev. **77** (1950) 242.

47. Morgan and G Shaw, *Pion-Pion Scattering Below 850 MeV. A Unique Solution*, Phys. Rev. D **2** (1970) 520.

48. G. Hohler *et al.*, *Handbook of Pion-Nucleon Scattering*, Karlsruhe, Germany, *Fachinformationszentrum Energie, Phys., Math* (1979) 440 pp.

49. R.J. Eden, P.V. Landshoff, D.I. Olive, and J.C. Polkinghorne, *The Analytic S Matrix*, Cambridge Univ. Press (1966) 287 pp.

50. H.D.I. Abarbanel and M.L. Goldberger, *Low Energy Theorems, Dispersion Relations, and Superconvergent Sum Rules for Compton Scattering*, Phys. Rev. **165** (1968) 1594.

51. D.H. Lyth, *Theoretical Investigation of the Process $\gamma\gamma \to \pi\pi$ at Low Energies*, Nucl. Phys. B **30** (1971) 195.

52. A.D. Martin and T.D. Spearman, *Elementary Particle Theory*, North Holland, Amsterdam (1970) Chapter 8.

53. D.H. Lyth, *The Shape of the f in $\gamma\gamma \to \pi\pi$*, Lancaster preprint (Sept. 1984).

54. C.D. Froggatt and J.L. Petersen, *Phase-Shift Analysis of $\pi^+\pi^-$ Scattering Between 1.1 and 1.8 GeV Based on Fixed Momentum Transfer Analyticity*, Nucl. Phys. B **91** (1975) 454.

55. K.M. Watson, *Some General Relations between the Photoproduction and Scattering of π Mesons*, Phys. Rev. **95** (1954) 228

56. D.H. Lyth, *Theoretical Description of the Process $\gamma\gamma \to \pi\pi$ Up To the f Region*, J. Phys. G **10** (1984) 39.

57. See V.M. Budnev *et al.*, *op. cit.*, page 217, for a review of the current-algebra theorems.

58. L. Lukaszuk, *A Generalization of the Watson Theorem*, Phys. Lett. **47B** (1973) 51.

59. G. Mennessier, *Meson Pair Production in $\gamma\gamma$ Scattering and Implications for Scalar Mesons*, Z. Phys. C **16** (1983) 241.

60. We thank Dr. A. Courau for this suggestion and for making the required modifications to the Mennessier code.

61. H.J. Behrend *et al.* (CELLO collaboration), *Production of the $f_0(1270)$ Meson in Photon-Photon Collisions*, Z. Phys. C **23** (1984) 223.

62. A.N. Vall, A.E. Kaloshin, and V.V. Serebryakov, *The Process $\gamma\gamma \to f(1270) \to \pi\pi$ and Low-Energy Parameters*, Novosibirsk preprint 144(3) (1985).

63. F. James and M. Roos, *MINUIT—A System for Function Minimization and Analysis of the Parameter Errors and Correlations*, Comp. Phys. Comm. **10** (1975) 343.

64. A. Courau, *et al.* (DELCO Collaboration), Pion-Pair Production from $\gamma\gamma$ Interactions at PEP and the Radiative Width of the f^0 Meson, Phys. Lett. **147B** (1984) 227.

65. J.M. Blatt and V.F. Weisskopf, *Theoretical Nuclear Physics*, John Wiley and Sons, New York (1952) pp. 359-365 and pp. 386-389.

66. H. Krasemann, J.A.M. Vermaseren, *The 2γ reaction $e^+e^- \to e^+e^-\pi^+\pi^-$ in the Resonance Region*, Nucl. Phys. B **184** (1981) 269.

67. U. Fano, Ann. Rev. Nucl. Sci. **13** (1963) 1.

68. R. Talman, *On the Statistics of Particle Identification Using Ionization*, Nucl. Instr. and Meth. **159** (1979) 189.

69. H.J. Lipkin, *Simple Branching Ratios and Sum Rules in Peripheral Reactions*, Nucl. Phys. B **7** (1968) 321.

70. Ch. Berger *et al.* (PLUTO collaboration), *Lepton and Hadron Pair Production in Two-Photon Reactions*, Phys. Lett. **94B** (1980) 254.
B. Adeva *et al.* (Mark-J collaboration), *Experimental Tests of Higher Order Quantum Electrodynamics at Small Distances*, Phys. Rev. Lett. **48** (1982) 721.

H.J. Behrend *et al.* (CELLO collaboration), *Lepton Pair Production in Deep Inelastic $e\gamma$ Scattering*, Phys. Lett. **126B** (1983) 384.

71. A. Courau *et al.* (DM1 collaboration), *Measurement of Lepton Pair Production in $\gamma\gamma$ Processes from e^+e^+ Collisions at DCI*, Phys. Lett. **84B** (1979) 145.

    A. Courau *et al.* (DM1 collaboration), *Measurement of Lepton and Pion Pair Production in Photon-Photon Collisions at DCI*, Phys. Lett. **96B** (1980) 402.

72. Ch. Berger *et al.* (PLUTO collaboration), *Lepton and Hadron Pair Production in Two-Photon Reactions*, Phys. Lett. **94B** (1980) 320.

73. R. Brandelik *et al.* (TASSO collaboration), *Two-Photon Excitation of the Tensor Meson f^0* (1270), Z. Phys. C **10** (1981) 117.

74. Ch. Berger *et al.* (PLUTO collaboration), *Pion Pair Production in Photon-Photon Interactions*, Z. Phys. C **26** (1984) 199.

75. P. Jenni *et al.* (Mark II collaboration), *Resonance Production by Two-Photon Interactions at SPEAR*, Phys. Rev. D **27** (1983) 1031.

76. N.P. Samios, M. Goldberg, and B.T. Meadows, *Hadrons and $SU(3)$: A Critical Review*, Rev. Mod. Phys. **46** (1974) 49.

    R. Ammar *et al.*, *f^* Production in K^-p Interactions at* 5.5 GeV/c, Phys. Rev. Lett. **19** (1967) 1071.

    V.E. Barnes *et al.*, *Properties of the f^* Meson* Phys. Rev. Lett. **19** (1967) 964.

77. See, for example, the discussion of the nonrelativistic quark model in Ref. 6, page S44.

78. M. Althoff *et al.* (TASSO collaboration), *Differential Cross Sections for $\gamma\gamma \to p\bar{p}$ in the CM Energy Range From 2.0 to 3.1 GeV*, Phys. Lett. **130B** (1983) 449.

    R. Brandelik *et al.* (TASSO collaboration), *Exclusive Proton-Antiproton Production in Two-Photon Collisions*, Phys. Lett. **108B** (1982) 67.

79. P.H. Damgaard, *Exclusive Processes in QCD: Two-Photon Physics Involving Baryons*, Nucl. Phys. B **211** (1983) 435.

80. G.R. Farrar, E. Maina, and F. Neri, *QCD Predictions for $\gamma\gamma$ Annihilation to Baryons*, Rutgers University print RU-85-08 (April 1985) 35pp.

81. V.L. Chernyak and I.R. Zhitnitsky, *Nucleon Wave Functions and Nucleon Form Factors in QCD*, Nucl. Phys. B **246** (1984) 52.

82. A. Courau, *Analytic Distributions of Various Parameters in $ee \to eex^+x^-$ Under Standard Experimental Conditions*, Phys. Rev. D **29** (1984) 24.

83. A useful introduction to practical Monte Carlo methods is F. James, *Monte Carlo Theory and Practice*, Reports on Progress in Physics **43** (1980) 1145.

84. The program is based on a similar program written by A. Courau, which he has documented in the report *A Fast Monte Carlo Generator for $ee \to eeX$ Untagged Experiments*, SLAC–PUB–3363 (June 1984).

85. J.M. Jauch and F. Rohrlich, *The Theory of Photons and Electrons*, Addison-Wesley, Reading Massachusetts (1955) equation 13-37.

86. G.P. Lepage, *A New Algorithm for Adaptive Multidimensional Integration*, J. Comput. Phys. **27** (1978) 192.

87. See the manual for the use of AXOLIB, the library of the Vermaseren routines (unpublished).

88. V. Blobel, *Unfolding Methods in High-Energy Physics Experiments*, DESY 84-118 *and* CERN Comp. School (1984) 88.